

Research & Development

2025

Mechanical Engineering Letters 2025

Technical-Scientific Journal supported by the Institute of Technology,
Hungarian University of Agriculture and Life Science (MATE), Gödöllő,
published by GATE Nonprofit Ltd.

Editor-in-Chief:
Dr. István SZABÓ

Editor:
Dr. Gábor KALÁCSKA

Executive Editorial Board:

Dr. István BARÓTFI	Dr. László KÁTAI
Dr. János BEKE	Dr. Sándor MOLNÁR
Dr. István FARKAS	Dr. Péter SZENDRŐ
Dr. László FENYVESI	Dr. Zoltán VARGA
Dr. István HUSTI	

International Advisory Board:

Dr. Patrick DE BAETS (B)
Dr. Radu COTETIU (Ro)
Dr. Manuel GÁMEZ (Es)
Dr. Klaus GOTTSCHALK (D)
Dr. Yurii F. LACHUGA (Ru)
Dr. Elmar SCHLICH (D)
Dr. Nicolae UNGUREANU (Ro)

Cover design:
Dr. László ZSIDAI

HU ISSN 2060-3789

All Rights Reserved. No part of this publication may be reproduced, stored in
a retrieval system or transmitted in any form or by any means, electronic,
mechanical, photocopying, recording, scanning
or otherwise without the written permission of GATE Nonprofit Ltd.

Páter K. u. 1., Gödöllő, H-2103 Hungary

Volume 26 (2025)

Contents

Bence KAZÁR, Márta SZABÓ: Evaluation of types and properties of phase change materials for heat emitters in buildings	5
Fares TOUAREF, István SERES, István FARKAS: Simulation and modelling of a tracking cylindro-parabolic collector using trnsys software	13
Hasna SAADI, Péter KORZENSZKY, Péter HERMANUCZ: Optimizing cooling efficiency: A statistical comparison of modified PVT and conventional PV panels under variable water flow rates	26
Csilla AGÓCS, László ZSIDAI: Laboratory production of different PLA filament composites by extrusion process, influential factors	39
Mahamadou Lamine Ousmane DIALLO, Ádám SARANKÓ, Tamás PATAKI, László ZSIDAI: Comparative vibration level of delta and Cartesian 3D printers: A MATLAB-enabled mobile sensor approach	47
Nejmeddine LAYEB, Rihem JEBALI, István OLDAL, István KEPLER: Interdependence of Tensile Strength and Hardness in FDM-Printed PLA: A Parametric Study	54
Feliciano SAMPAIO, Zoltán BÁRTFAI: Development and evaluation of a robotics system for plant health analysis and irrigation control	70
Bahram TURAPOV, Gábor KALÁCSKA, Róbert KERESZTES: Experimental Set-up of Sand-Pot Device for 3-Body Abrasive Wear Testing	76
Márton RÁTKAI, Gábor GÉCZI, Richárd KICSINY, László SZÉKELY: Energetic analysis and mathematical modelling of a solar-pot	85
Tamás György SÁRKÁNY, Gábor KALÁCSKA, Róbert KERESZTES: Tribological evaluation of glass fiber reinforced epoxy (GFRP) composites using pin-on-disc abrasion tests	107
László ZSIDAI, Benjámín MARKOVICS, Tamás PATAKI, Zoltán SZAKÁL, István SZABÓ, Norbert SCHREMPF, Róbert KERESZTES: Development of laboratory static fracture tests for milling tools	121
Adrián BOGNÁR, Krisztián KUN, László ZSIDAI: Analyzing the mechanical properties of bio photopolymer-composite test specimens	140

Rihem JEBALI, Nejmaddine LAYEB, László ZSIDAI:
Cradle-to-Cradle LCA for circular bio-based plastics:
a systemic framework for closed-loop material use

150

Evaluation of types and properties of phase change materials for heat emitters in buildings

Bence KAZÁR¹, Márta SZABÓ²

¹ *Doctoral School of Mechanical Engineering,
Hungarian University of Agriculture and Life Sciences,
MATE, Gödöllő*

² *Department of Building Engineering and Energetics, Institute of Technology,
Hungarian University of Agriculture and Life Sciences,
MATE, Gödöllő*

Abstract

Along with efforts to reduce carbon dioxide emissions and energy consumption, the use of renewable energy sources has also become increasingly widespread. Phase change materials (PCMs) are suitable for addressing energy storage challenges arising from these changes, as well as for reducing the heating and cooling energy demands of buildings. Additionally, PCMs can be effectively used to reduce peak heat demand and thermal load. To apply PCMs efficiently in buildings, it is essential to understand their types and properties. In this article, I will review the types and thermophysical properties of phase change materials that can be used in buildings, based on published studies.

Keywords

PCM, building, latent heat, phase change, energy storage, peak loads

1. Introduction

In recent years, efforts to reduce greenhouse gases, especially carbon dioxide emissions, have intensified. One possible means of reducing emissions is to use renewable energy sources instead of fossil fuels to cover our energy needs. Another means of reducing emissions is to increase energy efficiency and build buildings that use less energy while maintaining the level of indoor comfort. One of the biggest challenges in the application of renewable energy sources is the storage of the “produced” energy. Since the energy production and consumption profiles are different, we need efficient energy storage solutions. Phase change materials, thanks to their latent heat, provide the opportunity for high energy density energy storage. PCM can be placed in a separate storage container, or even directly next to the heat emitter (for example, next to underfloor heating pipes).

PCM built into the building envelope in hot climate zones can absorb summer heat loads during the hottest hours and release the absorbed heat at night. This way, it can protect the building's rooms from external heat loads and reduce the energy demand for mechanical cooling. In cold climate zones, PCM built into the walls of heated rooms can reduce heat demand peaks during the coldest hours.

2. Phase change materials for use in buildings

In the following, the term phase change material (PCM) refers to materials that use the property of undergoing phase transformation during heat absorption and heat release at a temperature we consider favorable. The definition also shows that the term phase change material refers to an arbitrarily defined set of materials and, depending on our goals, different materials may belong to this set. The use of many materials capable of phase change (such as ice, iron, zinc) in buildings is not possible because their melting point does not fall within the ideal temperature range for us.

2.1. Properties of phase change materials

Phase change materials are materials that release or absorb heat during a phase change (usually a liquid-solid or solid-liquid change). The advantageous property of the phase change is that it occurs at a nearly constant temperature. The theoretical (ideal) process can be more easily interpreted with the help of the temperature-enthalpy diagram. (Figure 1.) The advantage of using PCMs lies in the high energy density energy storage. As a result, phase change materials integrated into the building envelope are able to delay the timing of peak loads. (Al-Yasiri & Szabó, 2021)

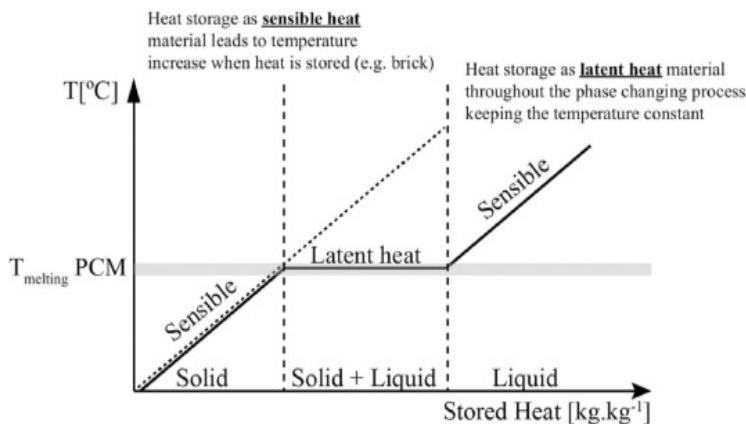


Figure 1. Temperature of the phase change material as a function of the thermal energy stored by a unit mass of PCM (Al-Yasiri & Szabó, 2021)

Figure 2. illustrates that for most real phase change materials, the phase change process does not occur at a discrete temperature value, but rather over a temperature interval. Melting and freezing start at different temperatures and the two processes take different “paths” on the enthalpy-temperature diagram (this is the phenomenon of hysteresis). (Que, et al., 2021) (Hu, et al., 2020) The phenomenon of supercooling (undercooling) can also be observed in Figure 2. When the liquid PCM is cooled to or below the temperature required for the onset of freezing, the liquid-solid phase transition does not occur. The temperature of the liquid PCM can be further reduced below the temperature required for the onset of freezing without the solid phase appearing. A small mechanical effect (shaking or introducing a small particle into a liquid) suddenly initiates the freezing process, which occurs “explosively” in an extremely short time. (Matolcsi, 2012)

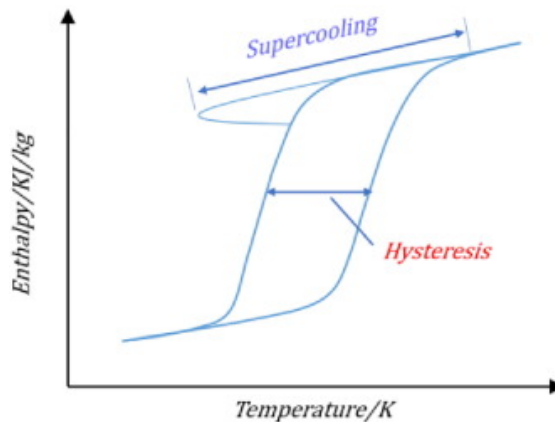


Figure 2. Interpretation of hysteresis and supercooling (subcooling) phenomena using the enthalpy-temperature diagram (Que et al., 2021)

The most important physical properties of phase change materials are illustrated in Table 1.

Table 1. Physical properties of phase change materials (Al-Yasiri & Szabó, 2021)

Property	Unit	Symbol
Fusion heat	kJ/kg	L_o
Melting point	°C or K	t_o or T_o
Specific heat	kJ/(kg*K)	c
Thermal conductivity	W/(m*K)	λ
Density	kg/m ³	ρ

When choosing phase change materials, in addition to thermophysical properties, attention should be paid to the following properties and characteristics of the PCM:

- phase segmentation (phase separation): During the solidification of the liquid phase, freezing starts at several points and the solid phases do not always coalesce (Andrássy, 2021)
- chemical and thermal stability
- corrosivity
- flammability
- leakage
- supercooling: the liquid must be cooled below the freezing point for the phase transformation to start (mechanical effect such as vibration or the introduction of a small particle causes freezing to occur suddenly) (Matolcsi, 2012)
- aging: deterioration of properties with time or with an increase in the number of phase change cycles

(Ning, 2025) (Lamrani, 2021) (Al-Yasiri & Szabó, 2021)

Al-Yasiri and Szabó summarized the requirements for phase change materials and their thermophysical properties. Ideal PCMs should have a high melting point, high specific heat (both in solid and liquid phases), good thermal conductivity, and high density. The ideal phase change material is non-flammable, non-toxic, ages slowly, has a small density difference between the liquid and solid phases, does not require supercooling to initiate freezing, and can withstand a sufficiently large number of phase change cycles without deterioration of its thermophysical properties. (Al-Yasiri & Szabó, 2021)

Real phase change materials cannot satisfy all the beneficial properties at the same time, so a compromise will be required regarding one of the characteristics.

The phase change materials studied by Al-Yasiri had melting points of 22...47 °C, heats of fusion of 147...245 kJ/kg, densities of 770...1530 kg/m³ in the liquid phase and 815...1681 kg/m³ in the solid phase. The specific heats of the studied PCMs fell between 1.46...2.72 [kJ/(kg K)]. (It should be noted that the specific heats of liquid and solid PCMs are different.)

2.2. Determination of the caloric thermophysical properties of phase change materials

A differential scanning calorimeter (DSC) is most often used to determine the temperature and enthalpy values of phase transitions, as well as the heat of transformation (e.g. heat of fusion). The essence of the procedure is that a sample and a reference piece with known thermophysical properties are heated so that their temperatures remain equal. The properties of the sample can be determined from the difference between the heat flows required to keep the sample and the reference piece at the same temperature. (ch.bme.hu)

Figure 3. illustrates the operating principle of the differential scanning calorimeter and the typical DSC curve obtained during the test.

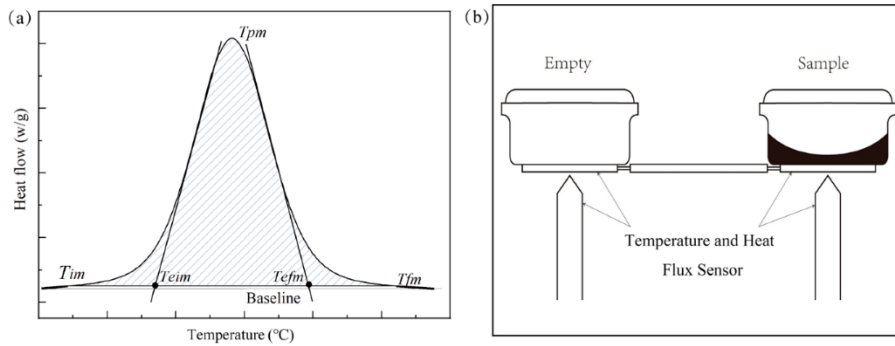


Figure 3. a) Typical DSC curve; b) working principle of differential scanning calorimeter (Gao, et al., 2024)

2.3. Types of phase change materials for use in buildings

Phase change materials that can be used in buildings can be classified into three main groups, as illustrated in Figure 4.

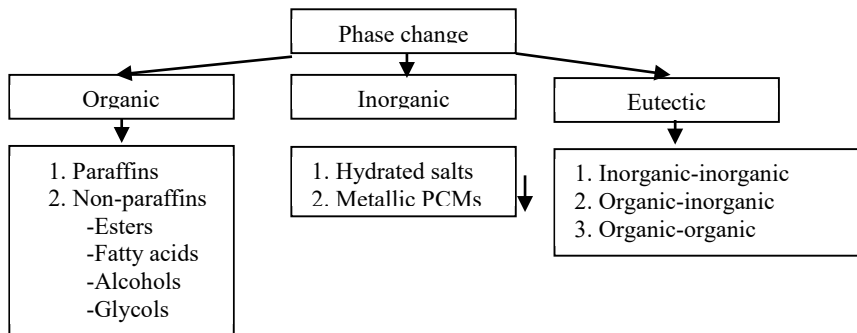


Figure 4. Types of phase change materials that can be used in buildings (Al-Yasiri & Szabó, 2021) (Lawag & Ali, 2022)

Wang et al. grouped organic phase change materials based on other criteria (Figure 5.) (Wang et al., 2022)

Wang emphasizes that paraffins are mixtures of alkanes with 20..40 carbon atoms. The melting point and latent heat of paraffins can be modified according to our needs by changing the number of carbon atoms (molecular weight) and composition. (Wang et al., 2022) Paraffins have good thermal stability, high

melting heat and can be used in a wide temperature range (between 15...45°C). Their advantageous properties are also that they do not cause corrosion, are relatively cheap and minimal supercooling is sufficient to initiate freezing. Disadvantages include that they are flammable, have low thermal conductivity and are incompatible with some plastic containers. (Lawag & Ali, 2022)

The advantageous and disadvantageous properties of different types of phase change materials are illustrated in Table 2. (Tyagi, 2022) (Al-Yasiri & Szabó, 2021)

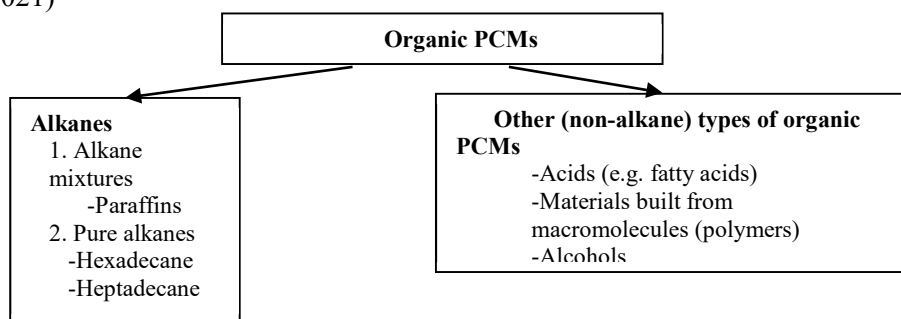


Figure 5. Classification of organic phase change materials (Wang et al., 2022)

Table 2. Advantages and disadvantages of organic, inorganic and eutectic phase change materials

	Organic PCMs	Inorganic PCMs	Eutectic PCMs
Advantages	<ul style="list-style-type: none"> • Chemical stability • Low supercooling • No phase segmentation • No definite melting point • High latent heat (heat of fusion) • High thermal conductivity • High latent heat (heat of fusion) 	<ul style="list-style-type: none"> • High thermal conductivity • High latent heat (heat of fusion) • Non-flammable • Definite melting point 	<ul style="list-style-type: none"> • High energy storage “density” can be achieved with it in a given volume • Definite melting point • Good chemical and thermal stability • Low subcooling
Disadvantages	<ul style="list-style-type: none"> • Flammable • High volume change • Low thermal conductivity 	<ul style="list-style-type: none"> • Significant subcooling • High volume change • Incompatible with metals • Low chemical and thermal stability 	<ul style="list-style-type: none"> • Expensive • Low thermal conductivity • Leakage

-
- Phase segmentation
-

Conclusions

- Phase change materials that can be used in buildings can be divided into three groups: Organic, inorganic and eutectic PCMs
- The ideal properties of phase change materials are: high specific heat (in solid and liquid phases), high latent heat, high thermal conductivity, high density, melting point adapted to the application area, chemical stability, thermal stability, slow aging, low subcooling, non-toxic, non-corrosive
- Phase change materials cannot satisfy all the beneficial properties at the same time, so a compromise will be required regarding one of the characteristics
- A differential scanning calorimeter is most often used to determine the caloric thermophysical properties of phase change materials
- In most cases, articles dealing with the application of phase change materials in buildings focus on the building envelope and are related to hot or cold climatic environments. The use of PCMs in heat transfer surfaces and their investigation under continental climatic conditions is a less researched area. Therefore, my research will address this topic.

References

- [1] Al-Yasiri., Qudama & Szabó, M. (2021). Incorporation of phase change materials into building envelope for thermal comfort and energy saving: A comprehensive analysis. *Journal of Building Engineering*, 36, 102122. <https://doi.org/10.1016/j.jobe.2020.102122>
- [2] Lawag, R. A., & Ali, H. M. (2022). Phase change materials for thermal management and Energy Storage: A Review. *Journal of Energy Storage*, 55, 105602. <https://doi.org/10.1016/j.est.2022.105602>
- [3] Lawag, R. A., & Ali, H. M. (2022). Phase change materials for thermal management and Energy Storage: A Review. *Journal of Energy Storage*, 55, 105602. <https://doi.org/10.1016/j.est.2022.105602>
- [4] Tyagi, V. V., Chopra, K., Sharma, R. K., Pandey, A. K., Tyagi, S. K., Ahmad, M. S., Sari, A., & Kothari, R. (2022). A comprehensive review on phase change materials for heat storage applications: Development, characterization, thermal and chemical stability. *Solar Energy Materials and Solar Cells*, 234, 111392. <https://doi.org/10.1016/j.solmat.2021.111392>
- [5] Que, L., Zhang, X., Ji, J., Gao, L., Xie, W., Liu, L., & Ding, X. (2021). Numerical simulation and experimental research progress of phase change hysteresis: A Review. *Energy and Buildings*, 253, 111402. <https://doi.org/10.1016/j.enbuild.2021.111402>
- [6] Hu, Y., Guo, R., Heiselberg, P. K., & Johra, H. (2020). Modeling PCM phase change temperature and hysteresis in ventilation cooling and heating applications. *Energies*, 13(23), 6455. <https://doi.org/10.3390/en13236455>
- [7] <https://www.ch.bme.hu/kutatas/reszletek/infrastruktura/7/> (2025.03.15.)
- [8] Matolcsi, T., (2012). *Közönséges termodinamika*. Budapest: Scolar Kiadó
- [9] Andrassy, Z. (2021) Fázisváltó anyaggal töltött hőtároló modellezése, optimalizálása és épületgépészeti rendszerekbe illesztése, *Budapesti Műszaki és Gazdaságtudományi Egyetem*
- [10] Ning, N., Sun, C., Ma, Z. J., Guo, S., Jiang, S., Zhang, J., Hou, D., & Wang, C. (2025). A review of incorporating pcms in various types of concrete: Thermal and mechanical properties, crack control, frost-resistance, and workability. *Journal of Energy Storage*, 114, 115814. <https://doi.org/10.1016/j.est.2025.115814>
- [11] Lamrani, B., Johannes, K., & Kuznik, F. (2021). Phase change materials integrated into building walls: An updated review. *Renewable and Sustainable Energy Reviews*, 140, 110751. <https://doi.org/10.1016/j.rser.2021.110751>
- [12] Gao, M., Zhao, S., Yang, H., Wu, X., & Xiao, Y. (2024). An analysis of the influence of DSC parameters on the measurement of the thermal properties of phase-change material. *Materials*, 17(23), 5689. <https://doi.org/10.3390/ma17235689>

Simulation and modelling of a tracking cylindro-parabolic collector using trnsys software

Fares TOUAREF¹, István SERES², István FARKAS³

¹ *Doctoral School of Mechanical Engineering,*

Hungarian University of Agriculture and Life Sciences, MATE, Gödöllő

² *Institute of Mathematics and Basic Science, Hungarian University of Agriculture and Life Sciences, MATE, Gödöllő*

³ *Institute of Technology, MATE, Gödöllő*

Abstract

In the field of solar power generation, parabolic collector technology is regarded as one of the most cost-effective and robust solutions, offering high efficiency in capturing solar energy. This study examines the simulation and practical implementation of a cylindro-parabolic collector (CPC) integrated with a solar tracking system. MATLAB was utilised for the design of the CPC, including the determination of the aperture angle and the analysis of solar radiation distribution. A detailed theoretical analysis was conducted to optimise the dimensions of the parabolic curve, followed by a simulation using TRNSYS software to evaluate the system's operational performance. The construction of the system involved assembling key components, including the reflective surface, receiver, fluid heating circuit, and a mechanical solar tracking device, which is controlled by electronic circuits programmed to adjust the collector's position in real time according to the sun's movement. A custom software application was developed to manage the system and facilitate the acquisition of important parameters, such as temperature and solar intensity. This approach integrates theoretical modelling with practical implementation, providing valuable insights into the efficiency and reliability of parabolic collectors for solar power applications.

Keywords

solar power, parabolic collector, solar tracking, TRNSYS simulation, thermal efficiency

1. Introduction

In recent years, the development of parabolic solar collectors has advanced significantly, driven by their cost-effectiveness and robust design (Touaref et al., 2025). Cylindro-parabolic collectors (CPCs) are particularly prominent in solar energy applications, including electricity generation, due to their high efficiency and reliability (Panja et al., 2025). The integration of sun-tracking systems with

CPCs enhances their performance by maintaining optimal solar alignment throughout the day (Panja et al., 2025). Advanced simulation tools, such as TRNSYS, are instrumental in the design and evaluation of these systems, enabling detailed modelling of their dynamic behaviour (Liu et al., 2025).

This study presents the theoretical design, simulation of a parabolic collector, equipped with a sun-tracking mechanism. The design process involved determining the dimensions of the parabolic curve, followed by simulating its operational performance using TRNSYS to account for solar radiation effects. The practical implementation encompassed constructing the collector's supporting structure, the focal system containing the heat transfer fluid, and the mechanical assembly of the sun-tracking system, complemented by programmed electronic control units. Custom-developed software was employed to control the system and facilitate the acquisition of operational parameters through a data logger interfacing via the computer's serial port. This comprehensive approach aims to validate the system's performance and efficiency, contributing to the ongoing development of cost-effective and robust solar energy solutions.

2. Theoretical study and mathematical models

Theoretical study and mathematical models are essential for evaluating the optical performance of cylindro-parabolic collectors. These models help optimize the collector's design by analysing factors like geometry, reflectivity, and solar concentration, ensuring maximum efficiency in capturing solar energy.

2.1. Optical performance of a cylindro-parabolic collector

2.1.1. Concentration ratio

The most common definition of the concentration ratio is based on the concept of surface area. It is given as the ratio of the aperture area to the receiver area, by Eq. 1 and as shown in the Fig. 1 (Touaref et al., 2025):

$$C_r = \frac{A_0}{A_r} \quad (1)$$

where A_0 is the aperture area, A_r is the absorber area.

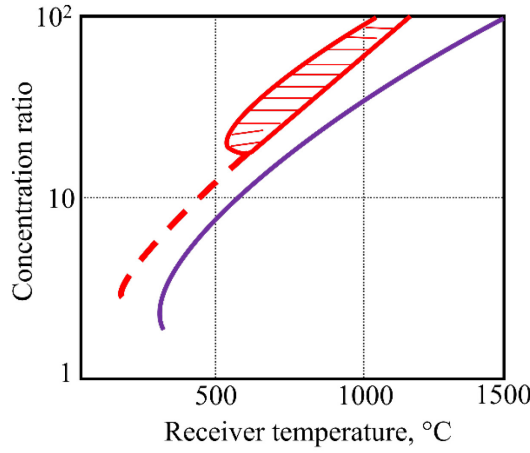


Figure 1. Relationship between the concentration ratio and the receiver temperature

Low concentrations ($1 < C_r < 10 \Rightarrow T_c \approx 150 \text{ }^\circ\text{C}$), Medium concentrations ($10 < C_r < 100 \Rightarrow T_c \approx 150 \text{ }^\circ\text{C}$), High concentrations ($C_r \geq 100 \Rightarrow T_c \geq 500 \text{ }^\circ\text{C}$).

2.1.2. Absorbed radiation

The absorbed radiation per unit of aperture area can be expressed at Eq. 2 (Touaref et al., 2025) as follows:

$$q_{abs} = C_r G \eta_{opt} \quad (2)$$

where q_{abs} is the absorbed radiation per unit of aperture area (W/m^2), C_r is the concentration ratio, G is the incident solar radiation (W/m^2), η_{opt} is the optical efficiency of the concentrator.

2.2. Thermal performance of a cylindro-parabolic Collector

The calculation of the performance of cylindrical parabolic concentrators follows the same calculation method as that of flat-plate thermal collectors.

The power gained at the collector Q_u can be calculated by knowing the values of the parameters F_R and U_L . Eq. 3 for thermal performance (Touaref et al., 2025):

$$Q_u = F_R A (G - U_L (T_m - T_a)) \quad (3)$$

where Q_u is the useful heat power gained at the collector (W), F_R is the collector heat removal factor, A is the aperture area of the concentrator (m^2), G is the

incident solar radiation (W/m^2), U_L is the heat loss coefficient ($\text{W}/\text{m}^2\cdot\text{K}$), T_m is the mean temperature of the collector ($^\circ\text{C}$), T_a is the ambient temperature ($^\circ\text{C}$).

2.2.4. Efficiency of the solar collector

The efficiency of the solar concentrator can be defined as the ratio of the useful heat power gained at the collector Q_u to the total incident solar radiation G on the aperture area A_0 . The Eq. 4 for the efficiency is:

$$\eta = \frac{Q_u}{G A_0} \quad (4)$$

where η is the efficiency of the solar concentrator, Q_u is the useful heat power gained at the collector (W), G is the incident solar radiation (W/m^2), A_0 is the aperture area of the concentrator (m^2).

2.3. Schematic diagram of the system used

Fig. 2 presents a comprehensive schematic diagram of the system, illustrating the acquisition system alongside all essential control and monitoring functions. The diagram highlights key components, including the parabolic collector, solar tracking mechanism, heat transfer circuit, and data acquisition system. It also depicts the integration of sensors for measuring parameters such as temperature, solar radiation, and wind speed.

Additionally, the schematic outlines the role of the electronic control unit, which processes real-time data and adjusts the concentrator's position accordingly. The system is further linked to a computer interface for data logging and performance analysis, ensuring efficient operation and continuous monitoring.

The heat transfer circuit is also depicted, showing the flow of the working fluid through the system, enabling the transfer of thermal energy from the collector to the heat exchanger. Sensors are strategically placed throughout the setup to measure critical parameters such as ambient temperature, fluid inlet and outlet temperatures, solar radiation intensity, wind speed, and system pressure. These measurements are crucial for evaluating the system's efficiency and performance.

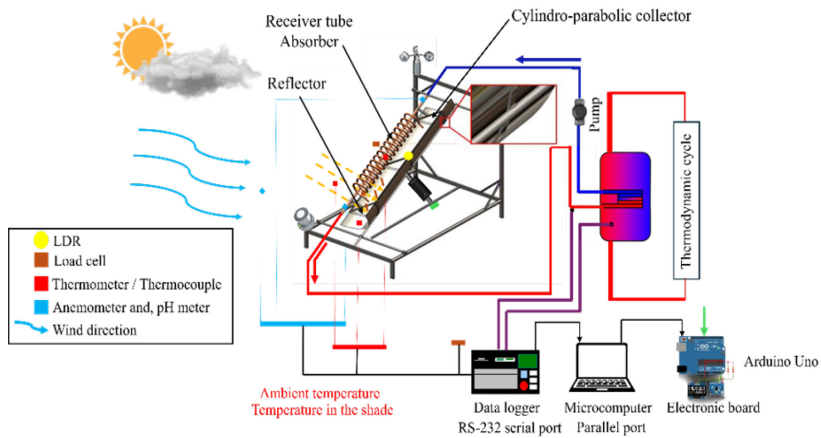


Figure. 2. Schematic diagram of the system

2.4. Simulation of the CPC's operation using TRNSYS

The simulation model is as follows: TYPE9f: Solar radiation model, TYPE65: Object for graphical display, TYPE74: CPC collector, TYPE3b: Circulation pump, TYPE91-2: Heat exchanger

This setup allows for the dynamic simulation of the energy system, covering solar radiation, the concentrator's thermal performance, circulation, and heat exchange processes as shown in the Fig. 3:

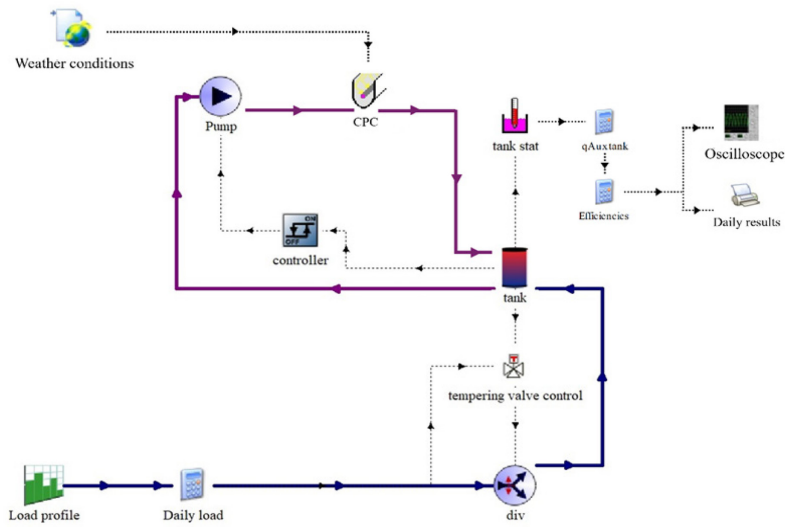


Figure. 3. TRNSYS-Based simulation of the CPC's performance

2.5. Simulation results

The simulation results provide insights into the performance of the cylindrical parabolic concentrator. Key outputs include Temperature variations at different points in the system; Thermal efficiency of the concentrator; Heat gain at the receiver and Effect of solar radiation on system performance, as shown in the Figs. 4 to 6:

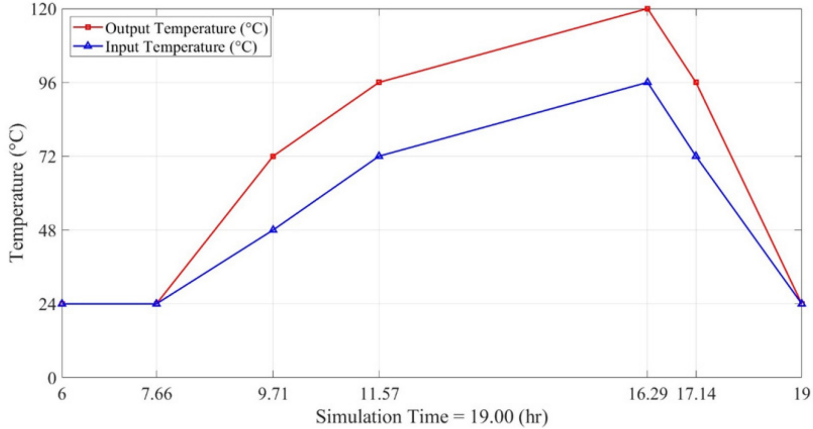


Figure 4. Simulation results of the CPC with a flow rate $Q = 12$ kg/h

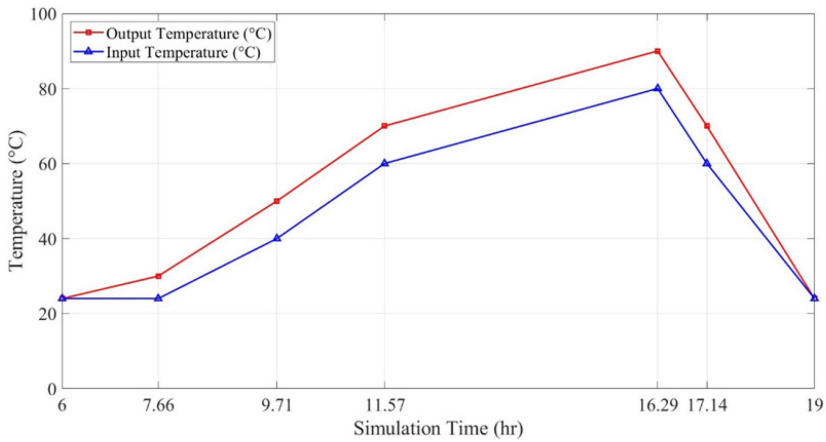


Figure 5. Simulation results of the CPC with a flow rate $Q = 48$ kg/h

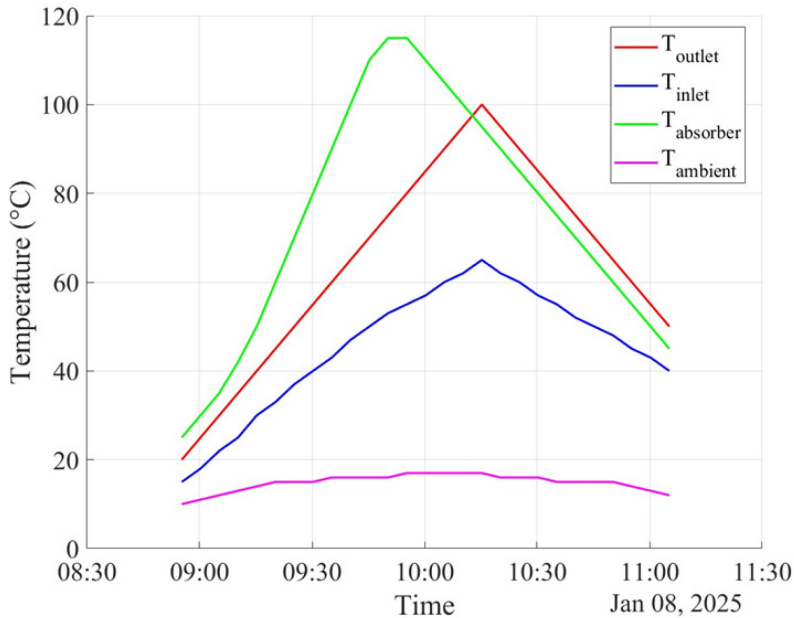


Figure. 6. Temperature evolution of the CPC system over time

3. Description of the implemented concentrator

This section outlines the design, components, specifications, and performance optimisation of the concentrator, highlighting its efficiency and integration.

3.1. Operating principle

The cylindro-parabolic collector is oriented towards the East at sunrise. Solar tracking is ensured by a controlled electric actuator. A heat transfer fluid, circulated by a pump, transports the absorbed heat to a heat exchanger located inside the storage tank.

The system is managed by a computer program that optimizes energy concentration throughout the day by controlling an electronic board via the computer's parallel port.

To achieve this, multiple parameters are acquired through a data logger that communicates via the serial port. The collected data is processed, stored, and can be displayed in real time on a magnetic storage medium.

3.2. Implementation of the cylindro-parabolic collector

3.2.1. Curve design

The shape of the cylindrical-parabolic concentrator is determined by the equation of a parabola, which is given by Eq. 5 (Touaref et al., 2025):

$$y = \frac{x^2}{4f} \quad (5)$$

where y is the height of the parabolic curve at a given point $x(m)$, x is the horizontal coordinate (m), f is the focal length of the parabola (m).

3.2.2. Construction of the supporting structure

Based on Eq. 5, to achieve a parabolic shape for the sheet metal (mirror), a metallic frame was constructed. The sheet metal was securely fixed onto the frame using rivets, as shown in the Fig. 7:

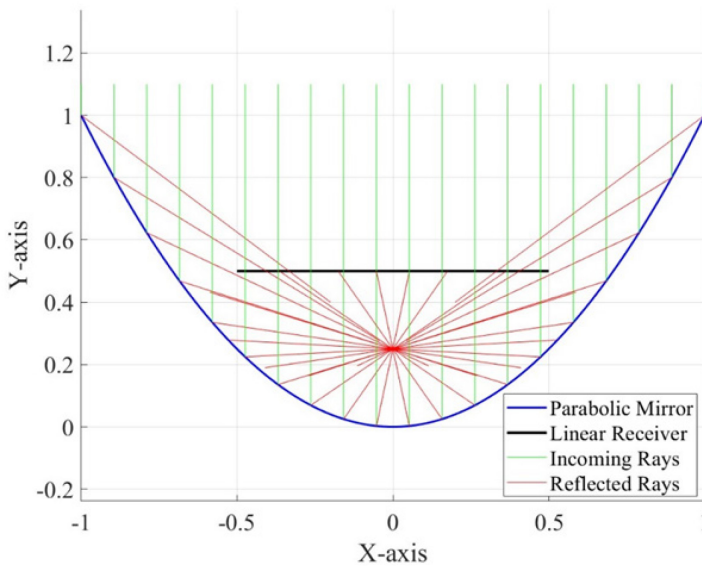


Figure. 7. Design of the CPC and aperture angle

4. Tests on the stationary concentrator

As shown in Fig. 8, installing a cylindro-parabolic collector with a solar tracking system involves several key considerations to optimise its efficiency. The first step is determining the optimal tilt angle, which is typically set equal to the latitude of the site. This ensures that the collector is positioned to capture the

maximum amount of solar energy throughout the year. Additionally, the collector must be oriented southward in the horizontal plane to align with the sun's path, allowing it to maximise exposure to sunlight during daylight hours. This specific configuration is a crucial factor in enhancing the overall performance of the concentrator.

Once the optimal tilt angle and orientation are set, the system is considered a stationary concentrator. This means that, unlike dynamic tracking systems that actively follow the sun's movement, the concentrator remains fixed in position, relying on its initial design to capture solar energy efficiently. By ensuring the collector is placed at the correct tilt and orientation, it maximises energy capture without requiring further adjustments. This configuration is ideal for regions where the sun's path remains relatively consistent and stable, allowing the stationary concentrator to deliver reliable and effective performance over time.

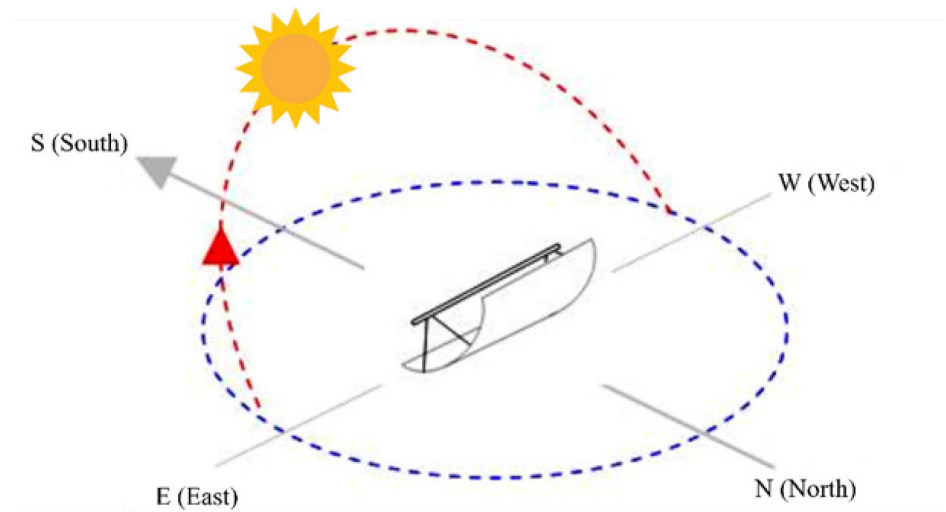


Figure 8. South-facing stationary concentrator

For solar tracking, An optical photoresistor sensor model CDs, was installed in the system to detect the solar radiation which connected to a driver to rotate the concentrator during the day by changing sunrays' angle. The concentrator axis was driven by a 12 V DC electric-motor with a gearbox.

The operation and implementation of the proposed solar tracking system (see Fig. 9) is like the principle of photovoltaic solar tracking, namely using the Maximum Power Point Tracking (MPPT) technique:

The automatic technology determines the position of the central point with two axes and provides movement commands required (Touaref et al., 2025). The movement of the absorber ensures that the reflection image and the focal point

overlap during both periods. Through electronic sensors (light sensors) sensitive to solar radiation and thermal sensors sensitive to solar temperature, the solar tracking mechanism is determined by a control board designed to pass through this parabolic concentrator with an iron bar that allows tilting or not tilting the parabolic concentrator using the motor.

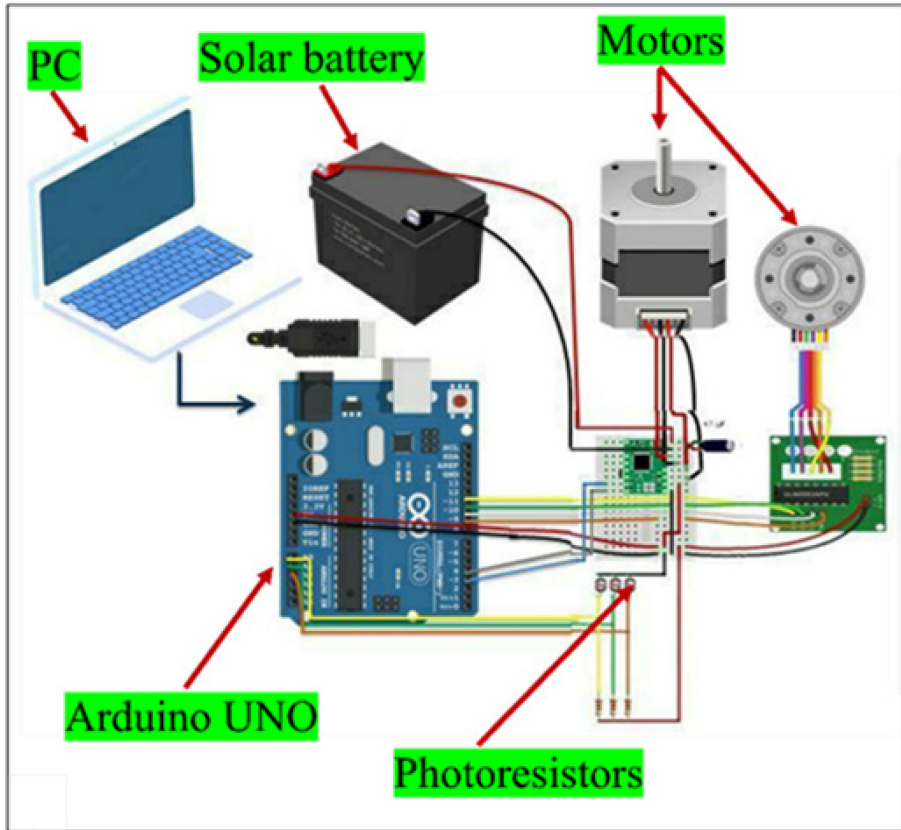


Figure. 9. Solar tracking system: Electronics and electrical components, and the mechanical method

To assess the efficiency of the system, tests were conducted on the concentrator, as shown in the Figs. 10, 11 and 12. During these experimental tests, temperatures at the focal point were measured throughout the day, including the temperature of the heat transfer fluid T_{fc} , the temperature of the absorber tube T_{abs} , the ambient temperature T_a , and solar radiation E . Tests conducted with a 30° tilt angle on a clear day yielded the following results:

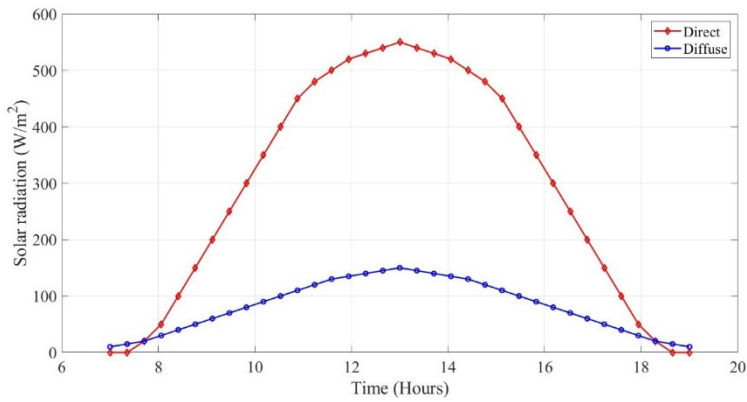


Figure 10. Incident solar radiation on a horizontal plane (07/01/2025)

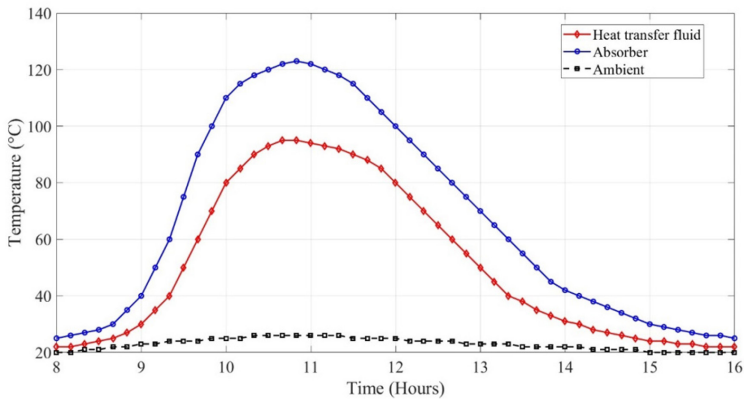


Figure 11. Temperature profile of the system (07/01/2025)

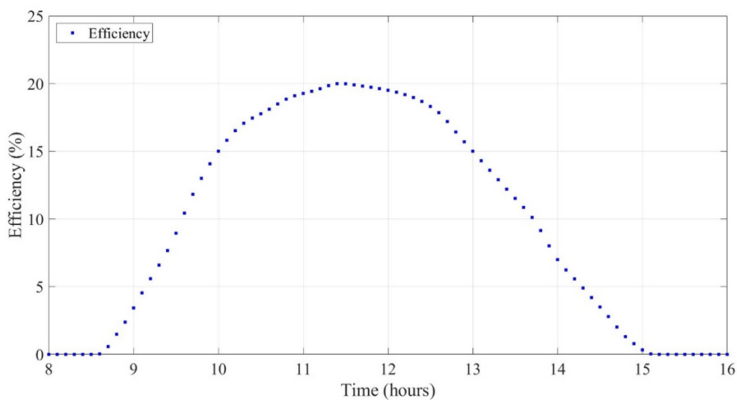


Figure 12. Efficiency of CPC (Gödöllő, Hungary)

6. Conclusion

In this study, a bibliographic review was carried out alongside an analysis of relevant documentation to determine the necessary equipment for the system. The design of the cylindrical-parabolic collector was developed, with a focus on optimizing the parabolic curve. A simulation using TRNSYS software was then conducted, incorporating the effects of solar radiation.

The results effectively demonstrated the system's operational behaviour and thermal performance. Additionally, the system was constructed, including its supporting structure, the focal system containing the heat transfer fluid, and the actuator mechanism responsible for solar tracking. Tests were performed under steady-state conditions with varying flow rates, revealing that the outlet temperature of the heat transfer fluid remained below 100 °C due to the use of water as the working medium.

The final phase of the study focused on evaluating the system's overall efficiency. The simulation results provided key insights into its thermal response and performance under different solar radiation levels. This analysis allowed for the identification of critical parameters affecting efficiency, enabling potential design optimizations. A comparison between simulated data and theoretical expectations has confirmed the system's feasibility for practical applications. Furthermore, the research highlighted several possible improvements that could enhance the performance and efficiency of the concentrator system. One such improvement involves using alternative heat transfer fluids with superior thermal conductivity and heat retention properties, which could significantly enhance energy absorption and transfer. Additionally, modifications to the design of the absorber tube, such as improved coatings or enhanced thermal insulation, could help reduce heat losses and improve overall efficiency. Another key advancement lies in integrating an advanced tracking mechanism that dynamically adjusts the concentrator's orientation in real time to maximise solar exposure throughout the day. Such a system would ensure optimal alignment with the sun, significantly improving energy capture and conversion efficiency. These findings contribute to the ongoing development of solar energy concentration technologies by identifying critical areas for refinement and providing a strong foundation for future advancements in the field.

NOMENCLATURE

A	Aperture area of the concentrator (m ²)
A_0	Aperture area (m ²)
A_r	Absorber area (m ²)
C_r	Concentration ratio
f	Focal length of the parabola (m)
F_R	Collector heat removal factor
G	Incident solar radiation (W/m ²)
q_{abs}	Absorbed radiation per unit of aperture area (W/m ²)

Q_u	Useful heat power gained at the collector (W)
T_a	Ambient temperature (°C)
T_m	Mean temperature of the collector (°C)
U_L	Heat loss coefficient (W/m ² .K)
x	Horizontal coordinate (m)
y	Height of the parabolic curve at a given point x (m)
η	Efficiency of the solar collector
η_{opt}	Optical efficiency of the collector

Acknowledgement

This work was supported by the Stipendium Hungaricum Program and by the Doctoral School of Mechanical Engineering, Hungarian University of Agriculture and Life Sciences, Gödöllő, Hungary.

References

- [1] Han, Y., Li, L., Wang, S., Bai, Z., Li, Q., (2025). A coupled optical-thermal-fluid-structural analysis of parabolic trough solar collector by deformation coupling instant ray tracing multiple iteration method. *Sol. Energy Mater. Sol. Cells* 279, 113221. <https://doi.org/10.1016/j.solmat.2024.113221>
- [2] Liu, S., Yang, B., Yu, X., 2025. Thermal transfer performance and flow instability analysis of direct steam generation for parabolic trough solar collectors. *Int. J. Therm. Sci.* 208, 109412. <https://doi.org/10.1016/j.ijthermalsci.2024.109412>
- [3] Panja, S.K., Das, B., Mahesh, V., (2025). Performance evaluation of a novel parabolic trough solar collector with nanofluids and porous inserts. *Appl. Therm. Eng.* 258, 124495. <https://doi.org/10.1016/j.applthermaleng.2024.124495>
- [4] Touaref, F., Saadi, A., Farkas, I., & Seres, I. (2025). Design and implementation of parabolic trough solar concentrator distiller. *Energy Reports*, 13, 1138–1157. <https://doi.org/10.1016/j.egyr.2025.01.001>

Optimizing cooling efficiency: A statistical comparison of modified PVT and conventional PV panels under variable water flow rates

Hasna SAADI¹, Péter KORZENSZKY², Péter HERMANUCZ³

¹ *Doctoral School of Mechanical Engineering,*

Hungarian University of Agriculture and Life Sciences, MATE, Gödöllő

² *Department of Farm and Food Machinery, Institute of Technology, MATE, Gödöllő*

³ *Institute of Technology, MATE, Gödöllő*

Abstract

The study compares the thermal performance of two PV panels with identical characteristics. One solar panel was converted into a PVT panel, where the cooling water flow rate was changed in two steps. The modification involves retrofitting the conventional PV panel with copper piping and an aluminium adhesive to enhance thermal conductivity and facilitate active cooling. Experiments were conducted under Hungary's climatic conditions, where temperature data were collected for both panels while the water flow rate was varied from 4 l/min to 7 l/min. The results reveal that the modified PVT panel consistently operates at lower temperatures than the unmodified PV panel. Statistical analysis via ANCOVA further indicates that each 1 l/min increase in water flow rate corresponds to an approximate 0.58 °C increase in the temperature difference ΔT between the two panels, even after controlling for ambient temperature and solar irradiance. These findings underscore the effectiveness of enhanced thermal management in maintaining optimal operating temperatures and suggest potential improvements in electrical output.

Keywords

Photovoltaic-Thermal (PVT) System, Conventional PV Panel, Working Temperature, Water Flow Rate, Cooling Efficiency, ANCOVA.

1. Introduction

Photovoltaic thermal (PVT) technologies have been studied since the 1970s, with research focusing on design variations, working fluids, and other factors that influence performance (Chow, 2010). The combined analysis of electrical and thermal efficiencies effectively illustrates the overall performance of PVT systems, as these systems simultaneously extract heat from the photovoltaic

model (PV) while maintaining the optimal temperature necessary to achieve maximum electrical output.

Ale's (2022) study reveals that the temperature of photovoltaic (PV) modules and other factors significantly affect how well PV systems perform. The research shows a strong positive connection between module temperature and critical performance metrics like solar irradiance, short-circuit current, output power, and conversion efficiency. For the specific monocrystalline module studied, the optimal operating temperature was around 60°C. Typically, solar panels are tested under standard conditions, and it was noted that for every degree Celsius increase in temperature, the panel's efficiency drops by about 0.4 % to 0,5 % (Natarajan et al., 2011).

Similarly, Al-Ghezi (2022) looked into how solar radiation and operating temperatures affect PV panels using simulations and real-life outdoor experiments. The results showed that higher operating temperatures negatively impact panel performance. Specifically, while a 1°C increase leads to a slight rise in current (around 0.068%), it also causes a decline in voltage (about 0.34%), output power (approximately 0.489%), and efficiency (roughly 0.586%). Dash and Gupta (2015) further explored the link between temperature and the power generated by different types of solar panels, using temperature coefficients as a reference. Their findings indicated that monocrystalline panels suffer the most, with an average power loss of 0.446% for each degree Celsius increase in temperature.

Meanwhile, Chander et al. (2015) conducted simulations to understand how higher temperatures affect PV panel performance, regardless of changes in solar radiation. They found that increased temperatures lower the fill factor, open-circuit voltage, and maximum power while directly impacting the short-circuit current. Tripathi (2021) focused on sunny days in February 2020 in Telangana, India, examining how solar radiation and ambient temperature influence PV panel temperatures. The study accurately predicted panel temperatures by employing a multi-linear regression model with low mean square error, noting a peak of 78.50°C under solar irradiance of 1140 W/m² and an ambient temperature of 36°C. These findings support the idea that extended exposure to high temperatures can harm panel efficiency and potentially damage the cells, negatively affecting overall performance and structural integrity.

To address the adverse effects of high working temperatures on the electrical output of PV panels, the PVT (thermal photovoltaic panel) configuration is positioned as a primary solution. In this system, integrating a thermal management mechanism with the PV panel actively extracts excess heat, thereby maintaining optimal operating conditions. However, achieving maximum electric and thermal efficiency with a PVT system is impossible due to the energy conservation principle. Nonetheless, to increase the overall efficiency of the PVT module, the most essential factors are the flow rate and fluid inlet temperature, as the cell temperature is heavily dependent on these (Radziemska, 2009), as well as the ambient temperature. For water-based PVT, an increase in

water flow rate increases the heat transfer coefficient, and Charalambous et al. (2011) have shown that the PVT efficiency is a function of the flow rate. Tiwari (2009) discovered that the overall exergy efficiency of systems initially rises with the mass flow rate, peaking at 0.006 kg/s before it starts to decline. Similarly, Morita (2000) found that for two different photovoltaic/thermal (PV/T) panel setups, the optimal mass flow rates were 1.4×10^{-3} kg/s for one design and 4.9×10^{-3} kg/s for the other, with the first configuration achieving a higher maximum energetic efficiency.

Kalogirou (2001) explored various water flow rates—0, 20, 25, 50, 100, and 150 litres per hour—and identified 25 l/h as the ideal rate, which led to an average annual electrical efficiency of 7.7% and a total efficiency (combining electrical and thermal) of 31.7%. Chow (2003) noted that increasing the water mass flow rate from 0.002 kg/s to 0.004 kg/s could result in a combined efficiency exceeding 70%. However, this high efficiency was usually reached outside the typical design parameters, highlighting the importance of accurately optimizing flow rates. In addition, Nualboonrueng (2013) reported that among mass flow rates ranging from 10 to 75 kg/h, a flow rate of 20 kg/h provided the best thermal and electrical outputs. Lastly, Li, Chen, and Novakovic (2025) examined a micro heat pipe PV/T system at flow rates of 0.16 l/s, 0.26 l/s, and 0.36 L/s, concluding that 0.36 L/s offered the best performance, achieving a thermal conversion efficiency of 38.0%, photovoltaic conversion efficiency of 15.9%, and an overall efficiency of 53.9%.

In conclusion, climatic conditions and operating temperature emerge as the two key factors in evaluating the performance and technical features of photovoltaic thermal (PVT) systems. While previous research on how flow rate affects PVT performance has offered valuable insights, these investigations have predominantly focused on regions outside of Hungary. Consequently, this paper aims to fill that gap by examining how the volume flow rate of water, which serves as the heat transfer medium in our case, influences the operating temperature of a modified PVT panel. This study will optimise system performance specifically for Hungary's distinct climatic conditions.

2. Experimental

This study used a standard PV panel and a modified version (Figure 1.a) featuring copper pipes attached to a Synthetic Resin adhesive containing 75% aluminium to enhance thermal conductivity (Figure 2.b). By adjusting the cooling flow rate, we aim to identify the optimal configuration for maximizing the system's performance. Sensors were employed to monitor changes in temperature, sunlight intensity, and ambient temperature, all aimed at designing a PV system that not only sustains but potentially improves its efficiency as temperatures rise, ultimately boosting solar energy performance.

2.1 Material

The experimental setup assessed how the flow rate of water as a heat transfer medium affected photovoltaic (PV) systems. The setup features a standard PV panel and a modified version (Figure 1). The modified panel has copper pipes attached to its backside using a Synthetic Resin adhesive containing 75% aluminium, applied in thicknesses ranging from 3 to 5 mm (Figure 2). Additionally, the system allows for adjustments to the cooling medium's flow rate to enhance heat removal, and it incorporates 20 mm of XPS insulation to minimize heat loss and maintain proper temperature control. A central component of the setup is an Arduino-based control unit, which is crucial for coordinating data collection and real-time monitoring through a network of strategically placed sensors. The system also includes a 10-litre thermal storage tank (Figure 3), which is essential for the cooling process of the modified PV-T panel. It stores and manages the cooling fluid to ensure a consistent supply.



Figure 1. Experimental Setup, a: PV and PVT, b: back side of both panels

Within our experimental framework, we utilised a carefully selected array of sensors to monitor and enhance the performance of both conventional and modified PV systems. These sensors are essential for gathering real-time data and critical for assessing system behaviour and efficiency. The LM335 temperature sensor was implemented to deliver accurate temperature measurements at various system points, maintaining precision within 1°C across a wide range. Additionally, the TF 6003.0000 BG irradiance sensor was employed to measure solar irradiance; it detects global radiation using a silicon

diode paired with a PMMA dome, making it ideal for photovoltaic applications as well as for climate research and agricultural purposes.

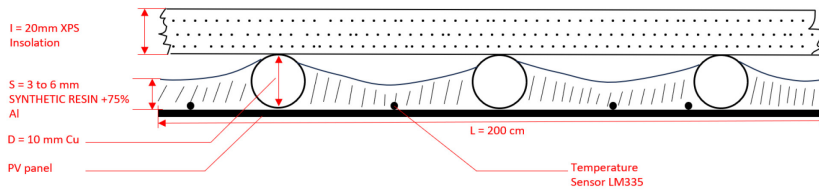


Figure 2. PVT Modified model design cross-section



Figure 3. Arduino-based control unit and the storage tank

Over four months (June, July, August, and September) in the energetic building's laboratory at the Hungarian University of Agriculture and Life Sciences, our experimental setup was deployed from 10:00 AM to 04:00 PM to evaluate conventional and modified PV systems. The modified system, featuring copper pipes attached to the panel's backside with a specialized adhesive containing 75% aluminium, enhances thermal conductivity and cooling efficiency. We incrementally adjusted the flow rate while using the TF 6003.100 irradiance sensor mounted on the PV panel via the PV-Sensor Mount and the LM335 temperature sensors, which were installed using dedicated Thermal Probe Brackets, to capture real-time data on irradiance, ambient temperature, and thermal variations. This comprehensive monitoring enabled us to optimize system performance and identify the optimal configuration for maximizing heat

capacity.

3. Results and discussion

The analysis utilizes data from two selected days to investigate the impact of the water's volume flow rate (Q), which serves as a heat transfer medium, while setting the supply temperature (T_{in} water temperature at the inlet of the modified PV panel) on both days at 10°C and under similar external conditions, on maintaining the PV panel at an optimal operating temperature for satisfactory electrical output. By examining these key variables, our goal is to understand how changes in these factors influence the operating temperature of the modified photovoltaic panel TPVT compared to that of the conventional panel TPVT and, consequently, how they affect the temperature difference ($\Delta T = TPV - TPVT$). An ANCOVA statistical approach was considered to determine the model for the impact of the main independent variable, flow rate (Q), on the dependent variable, ΔT , under the covariate variables solar irradiance (I) and ambient temperature (T_{amb}). This understanding will guide improvements in cooling efficiency and overall system performance.

3.1 The impact of the volume flow on ΔT

3.1.1 Observational Results and Graphical Analysis

Two flow rates (4 l/min and 7 l/min) were tested for two days to investigate how varying the cooling-water flow rate influences the temperature difference between a conventional photovoltaic (PV) panel and a photovoltaic-thermal (PVT) panel. On 19 September, the system was operated at 4 l/min, whereas on 18 September, the flow rate was increased to 7 l/min. Throughout both days, the PV and PVT panel temperatures were measured at regular intervals (between 10:00 AM and 04:00 PM) alongside ambient temperature (T_{amb}) and solar irradiance (I), ensuring that any observed differences in performance could be associated with the change in flow rate and the naturally varying weather conditions.

Table 1 provides descriptive statistics for the key variables measured during each test day. It reports the average temperature of the conventional PV panel (T_{PV}) and the modified PVT panel (T_{PVT}) and the difference between the two (ΔT). Additionally, ΔT is expressed as a percentage (ΔT_{avg}) to facilitate comparison under different flow rates.

Table 1. Descriptive statistics for T_{PV} and T_{PVT} , ΔT , T_{amb} and I on 18 Sept (7 l/min) and 19 Sept (4 l/min).

Date	T_{in} [°C]	Q [l/min]	Descriptive Statistics	T_{PV} [°C]	T_{PVT} [°C]	ΔT [°C]	ΔT_{avg} [%]	T_{amb} [°C]	I [W/m ²]
19- Sep	10	4	Mean	25.82	23.90	1.91	7.41%	24.36	709.20
			Standard deviation	4.94	5.26	0.76		2.38	215.07
			Min	12.33	10.67	1.86		19.93	387.91
			Max	30.66	28.40	4.96		26.50	899.60
18- Sep	10	7	Mean	29.09	25.84	3.25	11.17%	27.65	720.29
			Standard deviation	3.30	4.19	1.13		3.19	133.17
			Min	19.71	13.06	1.65		20.89	264.25
			Max	34.24	31.44	6.97		30.79	914.61

Figure 4 and Figure 5 display the temperature changes in both PV and PVT as a function of time for each flow rate condition (4 l/min on 19 September and 7 l/min on 18 September). The T_{PV} and T_{PVT} temperatures in Figure 4 gradually rise over the day, with T_{PVT} consistently remaining lower than T_{PV} . The difference ΔT , as calculated from Table 1 (7.41%), shows a moderate temperature gap between the two panels, with a maximum observed difference of 4.96°C at 10:40 AM. On 18 September, with a flow rate of 7 l/min, the temperatures again increased over time, but the gap between the PV-T and PVT-T is wider compared to 19 September. The ΔT is higher (11.17%), with a peak difference of 6.97°C at 10:50 AM. The visual comparison between the two charts indicates that increasing the flow rate from 4 l/min (19 September) to 7 l/min (18 September) results in a higher temperature difference (ΔT) as expected, confirming that the higher flow rate enhances the cooling capacity of the PVT panel and increases the temperature gap between the PV and PVT panels.

Figure 6 provides a box-and-whisker comparison of ΔT under 4 l/min and 7 l/min flow rates. The median of the 4 l/min group (blue) is around 2 °C, while the 7 l/min group (orange) has a higher median of about 3 °C. Moreover, the interquartile range (IQR) is narrower for the 4 l/min condition, indicating less variability in ΔT compared to the 7 l/min group, which has a broader IQR. The whiskers and outliers show that, although ΔT sometimes exceeds 5 °C or 6 °C at 7 l/min, most values still cluster above those from the 4 l/min group. This confirms that a higher flow rate consistently yields a more significant temperature difference, implying more effective cooling of the PVT panel than the conventional PV.

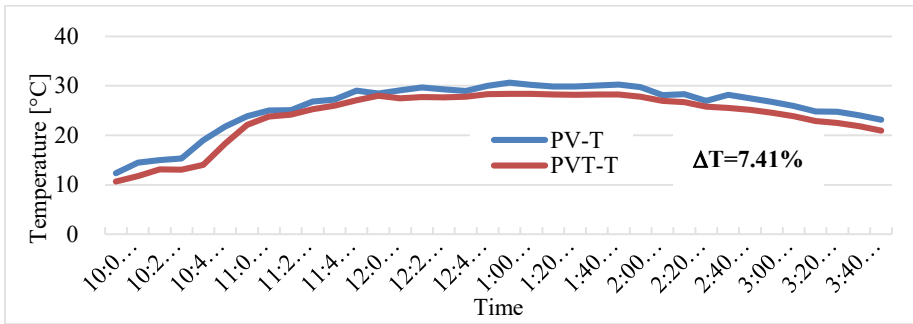


Figure 4. Variation of T_{PV} and T_{PVT} With Time on 19 September 2024 (4 l/min)

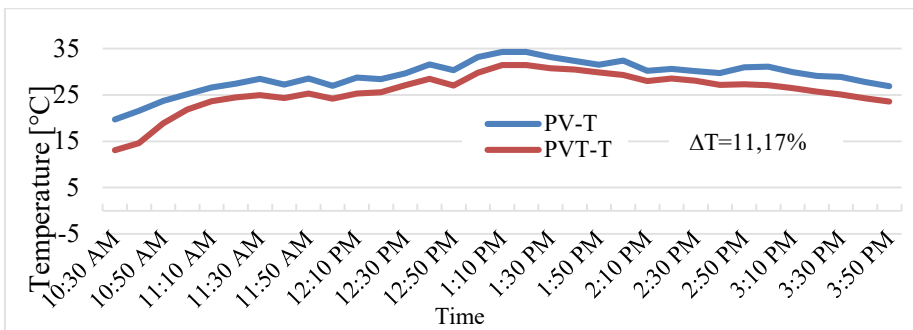


Figure 5. Variation of T_{PV} and T_{PVT} With Time on 18 September 2024 (7 l/min)

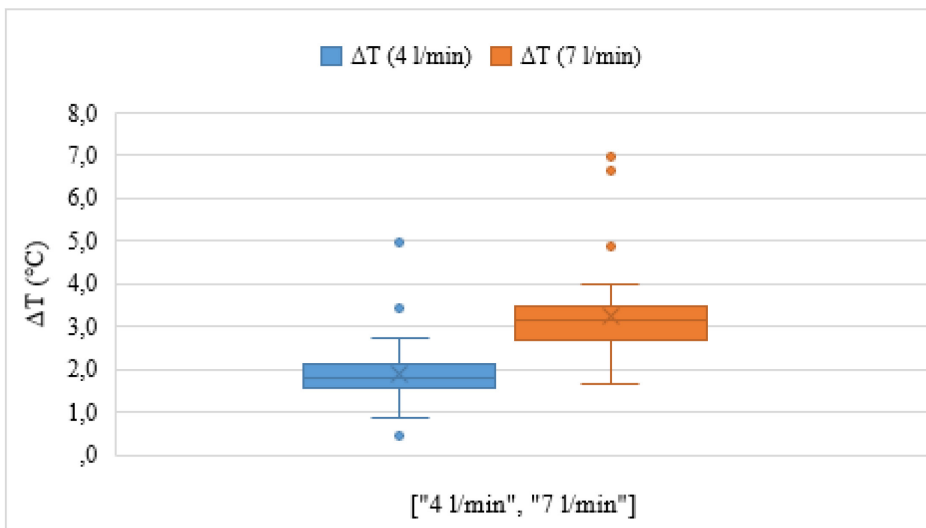


Figure 6. Distribution of ΔT under 4 l/min and 7 l/min Water Flow Rates

3.1.2 Statistical Evaluation Using ANCOVA

Analysis of Covariance (ANCOVA) is a statistical method that integrates features of both analysis of variance (ANOVA) and regression. In our study, ANCOVA is an ideal tool to determine whether the cooling water flow rate significantly affects the temperature difference (ΔT) between the conventional PV and the PVT panel. Importantly, ANCOVA allows us to control for the potentially confounding effects of ambient conditions, specifically solar irradiation and ambient temperature, which are known to influence panel temperatures. By including these continuous covariates, we can isolate and accurately quantify the effect of flow rate on ΔT .

Our model is structured as follows:

$$\Delta T = \beta_0 + \beta_1(\text{Flow rate}) + \beta_2(\text{Solar Irradiation}) + \beta_3(\text{Ambient Temperature}) + \epsilon \tag{1}$$

- ΔT – Temperature difference (Dependent Variable)
- β_0 – The baseline value of ΔT when all predictors are zero. (Intercept)
- β_1 – Flow Rate; Captures the effect of increasing the cooling water flow rate (Independent variable)
- β_2 – Solar Irradiation;
- β_3 – Ambient temperature; These covariates adjust for day-to-day variations, ensuring that changes in ambient conditions do not confound the effect of the flow rate.
- ϵ – This represents the error term. It captures the variability in ΔT not explained by the predictors /flow rate, solar irradiation, and ambient temperature/. (Residual)

Table 2. Regression/ANCOVA Coefficients results assessing the impact of flow rate and ambient conditions on ΔT .

	Coefficient <i>s</i>	Standard Error	<i>t</i> Stat	<i>P</i> -value	Lower 95%	Upper 95%	Lower 95.0%	Upper 95.0%
Intercept	3.63	0.77	4.72	1.30347E-05	2.09	5.16	2.09	5.16
Flow rate [l/min]	0.58	0.08	7.53	2.0×10 ⁻¹⁰	0.42	0.73	0.42	0.73
Solar Irradiation [W/m ²]	0.00	0.00	2.77	0.007377735	0.00	0.00	0.00	0.00
T _{amb} [°C]	-0.11	0.04	2.76	0.007409630	-0.20	-0.03	-0.20	-0.03

Table 2 displays the ANCOVA results assessing the impact of flow rate, solar irradiation, and ambient temperature on ΔT):

- Intercept: The intercept (3.6273) represents the baseline ΔT when all other variables (flow rate, solar irradiation, and ambient temperature) are zero. It mainly serves as a reference point in the model.
- Flow Rate [l/min]: This positive and highly significant coefficient (0.5764, $p \approx 2.0 \times 10^{-10}$) indicates that increasing the flow rate by 1 l/min raises ΔT by roughly 0.58 °C, even after controlling for ambient conditions. It confirms that the PVT panel's cooling effectiveness grows as the flow rate increases.
- Solar Irradiation [W/m²]: Although small in magnitude, the coefficient is negative (-0.00176, $p \approx 0.0074$), implying that higher solar irradiation slightly reduces ΔT . Each additional 1 W/m² of solar irradiance is associated with a slight reduction in ΔT by about 0.00176 °C. As irradiation rises, both panels warm up, narrowing the temperature gap between them.
- Ambient Temperature [°C]: With a negative coefficient (-0.1137, $p \approx 0.0074$), each 1 °C rise in ambient temperature corresponds to a 0.11 °C decrease in ΔT . In warmer conditions, both panels start from a higher baseline temperature, which reduces the PVT panel's relative cooling advantage.

These findings confirm that flow rate is the primary driver of the temperature difference between the PV and PVT panels. While ambient conditions do significantly affect ΔT , the strong positive coefficient for flow rate supports the conclusion that higher flow rates enhance the cooling performance of the PVT system relative to a conventional PV panel.

In addition to the ANCOVA coefficients, an ANOVA confirmed that the model is statistically significant, with predictors accounting for approximately 57% of the variance in ΔT . Furthermore, the residual analysis revealed that the errors are minor and randomly distributed, indicating that the assumptions of linearity, homoscedasticity, and independence are satisfactorily met.

Conclusions

The study demonstrates that optimising the water flow rate in a modified photovoltaic-thermal (PVT) system significantly improves cooling performance, boosting overall system efficiency. The experimental setup involved a standard PV panel enhanced with copper piping and aluminium adhesive to increase thermal conductivity, allowing for careful monitoring of temperature changes under controlled flow conditions and a conventional PV panel stand-alone to compare it with the modified one.

The findings reveal that raising the water flow rate from 4 l/min to 7 l/min dramatically increases the temperature difference ($\Delta T = T_{PV} - T_{PVT}$) between the standard PV panel and the modified PVT panel. ANCOVA analysis further

validated this conclusion, showing that for every 1 l/min increase in flow rate, ΔT rises by about 0.58 °C, even considering the effects of ambient temperature and solar irradiance. Although ambient conditions have a slight negative impact, the flow rate is the main factor driving improved cooling efficiency.

Focusing on Hungary's specific climatic conditions, this study addresses an important research gap and lays a solid foundation for optimising PVT performance. Overall, the research confirms that effective thermal management through enhanced water flow keeps operating temperatures within an ideal range and can potentially increase electrical output, contributing to the advancement of solar energy technologies.

The next paper will build on these findings by examining how inlet temperature, treated as an independent variable, affects ΔT while considering irradiance and ambient temperature as covariates. Additionally, future research will investigate the practical effects of removing or adding insulation to the system on overall PVT performance. This upcoming work aims to deepen our understanding of thermal management strategies, ultimately leading to increased efficiency and more adaptable designs in next-generation photovoltaic-thermal technologies.

Acknowledgements

The project is implemented with the support of the call for tenders for Incentives of Corporate Research, Development, and Innovation Activities announced within the framework of the Széchenyi Terv Plusz program („Széchenyi” Plan Plus Programme), within the framework of the Economic Development and Innovation Operational Programme Plus (GINOP Plusz). Thank you for the financial support. The title of the project: "Scalable Cogeneration Solution by Integrating Solar Energy and Biomass Utilization". Project id. number: GINOP_PLUSZ-2.1.1-21-2022-00165.

References

- [1] Ale, T. O., Rotipin, K., Makanju, T. D. (2022): Temperature effects on optimal performance of PV module. *Journal of Engineering Advancements*, 162–165. <https://doi.org/10.38032/jea.2022.04.004>
- [2] Al-Ghezi, M. K. S., Ahmed, R. T., Chaichan, M. T. (2022): The influence of temperature and irradiance on performance of the photovoltaic panel in the middle of Iraq. *International Journal of Renewable Energy Development*, 11(2), 501–513. <https://doi.org/10.14710/ijred.2022.43713>
- [3] Chander, S., Purohit, A., Sharma, A., Nehra, S. P., Dhaka, M. S. (2015): A study on photovoltaic parameters of monocrystalline silicon solar cell with cell temperature. *Energy Reports*, 1, 104–109. <https://doi.org/10.1016/j.egy.2015.03.004>
- [4] Charalambous, P., Kalogirou, S., Maidment, G., Yiakoumetti, K. (2011): Optimization of the photovoltaic thermal (PV/T) collector absorber. *Solar Energy*, 85(5), 871–880.
- [5] Chow, T. T. (2003): Performance analysis of photovoltaic-thermal collector by explicit dynamic model. *Solar Energy*, 75(2), 143–152. <https://doi.org/10.1016/j.solener.2003.06.003>
- [6] Chow, T. (2010): A review on photovoltaic/thermal hybrid solar technology. *Applied Energy*, 87, 365–379.
- [7] Dash, P., Gupta, N. C. (2015): Effect of temperature on power output from different commercially available photovoltaic modules. *International Journal of Engineering Research and Applications*, 5(1), 148–151.
- [8] Kalogirou, S. A. (2001): Use of TRNSYS for modelling and simulation of a hybrid pv–thermal solar system for Cyprus. *Renewable Energy*, 23(2), 247–260. [https://doi.org/10.1016/S0960-1481\(00\)00098-1](https://doi.org/10.1016/S0960-1481(00)00098-1)
- [9] Morita, Y., Fujisawa, T., Tani, T. (2000): Exergetic evaluation of photovoltaic/thermal hybrid panel. *Electrical Engineering in Japan*, 133(2), 43–51. [https://doi.org/10.1002/1520-6416\(20001115\)133:2<43::AID-EEJ5>3.0.CO;2-R](https://doi.org/10.1002/1520-6416(20001115)133:2<43::AID-EEJ5>3.0.CO;2-R)
- [10] Natarajan, S., Mallick, T., Katz, M., Weingaertner, S. (2011): Numerical investigations of solar cell temperature for photovoltaic concentrator system with and without passive cooling arrangements. *International Journal of Thermal Sciences*, 50(12), 2514–2521. <https://doi.org/10.1016/j.ijthermalsci.2011.06.014>
- [11] Nualboonrueng, T., Tuenpusa, P., Ueda, Y., Akisawa, A. (2013): Performance of photovoltaic-thermal systems for residential application in

Bangkok. *Progress in Photovoltaics: Research and Applications*, 21(5), 1204-1213. <https://doi.org/10.1002/pip.2181>

[12] Li, R., Chen, Y., Novakovic, V. (2025): Investigation of thermal resistance and flow rate impacts on micro heat pipe PV/T systems under dust accumulation conditions. *Renewable Energy*, 241, 122309. <https://doi.org/10.1016/j.renene.2025.03.042>

[13] Radziemska, E. (2009): Performance analysis of a photovoltaic-thermal integrated system. *International Journal of Photoenergy*, 2009.

[14] Tiwari, A., Dubey, S., Sodha, M. S. (2009): Exergy analysis of an integrated photovoltaic thermal solar water heater. *Applied Energy*, 86(5), 2592–2597. <https://doi.org/10.1016/j.apenergy.2009.04.004>

[15] Tripathi, A. K., Ray, S., Aruna, M. (2021): Analysis on photovoltaic panel temperature under the influence of solar radiation and ambient temperature. In *Proceedings of the 2021 1st International Conference on Advances in Electrical, Computing, Communications and Sustainable Technologies (ICAECT 2021)*. <https://doi.org/10.1109/ICAECT49130.2021.9392619>

Laboratory production of different PLA filament composites by extrusion process, influential factors

Csilla AGÓCS¹, László ZSIDAI²

¹ *Doctoral School of Mechanical Engineering,*

Hungarian University of Agriculture and Life Sciences MATE, Gödöllő

² *Department of Materials Science and Engineering Processes, Institute of Technology,
MATE, Gödöllő*

Abstract

Filament extrusion is a fundamental technology in plastic processing, in which a polymer material is melted and formed into a continuous filament (Gao et al., 2019). The process is crucial for 3D printing, as most printers use molten filament to produce objects (Wang et al., 2021). With the spread of 3D printing and the increasing demand for custom manufacturing, filament extrusion and the use of various additives are expanding. This article discusses the production of graphite-filled PLA filaments in different weight percentage compositions and the investigation of filament diameters.

Keywords

filament extrusion, PLA, graphite

1. Introduction

Additive manufacturing is a technology that can be used to rapidly produce parts by using 3D geometric information of objects and adding materials layer by layer. FDM technology was developed in the 1970s, and by the 1980s it was used not only for prototyping but also for the production of main parts (Wang et al. 2019). Additive manufacturing faces problems compared to traditional manufacturing, but the mechanical properties of the parts produced in this way are better, since the composite materials used in additive manufacturing combine the best properties of their materials (Valvez et al. 2020). Additive manufacturing technology has become most widespread with 3D printing, which allows the high-precision and low-cost production of physical models and complex geometric structures (Jha et al. 2020, Shanmugam et al. 2020). The raw materials for 3D printers are polylactic acid (PLA), acrylonitrile butadiene styrene (ABS), polyvinyl alcohol (PVA), PETG and its derivatives. PLA and ABS filaments are widely used due to their recyclability, marketability and cost-effectiveness (Wang et al. 2019)

1.1 Filament extrusion in general

The process for producing filaments is extrusion, a multi-step process. First, the raw granules or powder are fed into a screw, where the material is melted under pressure and heat (Throne, 2015). The homogeneous melt is then forced through a nozzle, where solidification and cooling processes occur (Peng et al., 2020). The consistency of the final diameter of the filament is of paramount importance, as it affects the subsequent printing application (Turner et al., 2014). The selection of the appropriate extrusion parameters depends on several factors, such as the type of polymer, melting temperature, screw profile geometry, temperature control, cooling rate, all of which influence the optimization of the material viscosity, filament crystallinity, internal stresses, and thus the final mechanical properties of the printed object (Gibson et al., 2021, Sun et al., 2018). In the following, the extrusion of PLA filament and its difficulties will be explained, as the article discusses the production of graphite-filled PLA filament.

PLA (polylactic acid) is a biodegradable polymer that is often used in 3D printing due to its easy processability, low melting point, and environmentally friendly properties (Gebhardt et al., 2017). During extrusion, the material is fed into the extruder in the form of granules or powder, where it is heated to a liquid state and a filament of the desired diameter is created by extrusion through nozzles (Turner et al., 2014). The filament diameter is a critical parameter in 3D printing, and its accuracy is essential during printing, as too thick or thin filaments can lead to defects, such as adhesion problems between layers or geometric inaccuracies (Wang et al., 2007).

The extrusion temperature affects the viscosity of PLA, which affects the filament diameter; at low temperatures, it leads to an increase in the thickness of the filament, while at high temperatures, the material is too fluid and causes the filament to become thinner (Levenhagen & Dadmun, 2018). Pressure is also an important factor, as too high a pressure leads to a decrease in the filament diameter (Rahim et al., 2019). The initial diameter of the filament is also affected by the nozzle size, and the final diameter is also affected by the cooling rate, as rapid cooling can cause the filament to shrink, and slow cooling can cause the filament to deform (Kantaros & Karalekas, 2013).

Other influencing factors are the flow properties: viscosity, shear rate. Viscosity is temperature-dependent, and increasing the extrusion speed also increases the shear rate, which can reduce the viscosity and affect the filament diameter (Li et al., 2017).

2. Experimental

2.1. Material

During the study, graphite-filled PLA filaments with different compositions (0.5%, 1%, 2%, 5%) were produced in a single-screw extruder for subsequent mechanical tests. The physical and mechanical properties of the materials used in the study are given in Table 1.

Table 1. Physical and mechanical properties of PLA (Sağlam et al. 2022, Khan et al. 2023)

Material	Tensile strength (MPa)	Modulus of elasticity (MPa)	Hardness (Shore D)	Melting temperature (°C)
PLA	42	104	75	180-220°C

The graphite used in the study was commercially available, particle size: $80\% < 80\mu\text{m}$, purity 87%. During the study, several weight percentage compositions were tested, above 5% composition, blockages occurred in the filament outlet nozzle of the extruder.

2.2. Method

The filaments used in FDM type 3D printers are produced in an extruder. In this study, the filaments were obtained from a laboratory type extruder filament machine, as shown in Figure 1. The structure of the extruder machine is as follows: a granule feeder is located at the top of the machine, where the raw material is loaded, the internal screw pushes the material forward while melting it evenly. There are several heating zones in the extruder body, which ensure the correct processing temperature. The molten plastic exits through a precision nozzle, which determines the final diameter of the filament (1.75 mm or 2.85 mm). The drawn filament thread passes through an air-cooled channel and then enters the winding unit, which ensures a uniform and orderly filament.

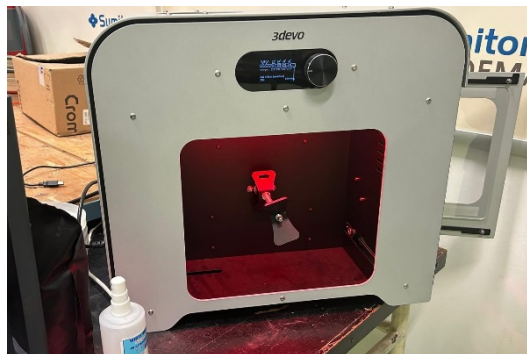


Figure 1. Extrusion machine for filament production

Table 2. Technical characteristics of the filament extruder machine

Properties	Values
Extruder machine size	506x216x540 mm
Nozzle diameter Ø	Ø 1,75 cm
Extrusion screw diameter Ø	Ø 0,5-3 mm
Power	110 – 240 V, 50 – 60 Hz

The PLA + graphite composite filaments used in the study were extruded on the extruder machine shown in Figure 1. The parameters recommended by the manufacturer were used and then optimized in several steps until the filaments with the desired composition were produced. The granulate was always mixed with the amount of graphite powder corresponding to the required composition (Table 3) before being loaded into the machine, after one minute of mechanical mixing.

Table 3. Mixing ratios of PLA and graphite powder

%	Granulate (g)	Graphite powder (g)
0%	100	-
0,5%	99,5	0,5
1%	99	1
2%	98	2
5%	95	5

The extruder has four heating zones, which were optimized to achieve the appropriate (bubble-free, smooth surface) filaments (Table 4).

Table 4. Optimal process parameters for PLA filaments

Material	Temperature				Extrusion speed (rpm)
	Zone 1	Zone 2	Zone 3	Zone 4	
PLA	210	215	215	220	3,5

The filaments produced in the extruder were tested by measuring the diameter every 1 meter of length. Table 5 shows the diameter values measured during filament production

Table 5. Diameter of filament samples.

Material	Φ mm)	Φ (mm)	Φ (mm)	Φ (mm)	Φ (mm)	Average Φ (mm)	Standard deviation	Failure%
PLA + 0% graphite	1,6	1,65	1,67	1,7	1,7	1,664	0,0416	2,50
PLA + 0,5% graphite	1,57	1,64	1,7	1,68	1,65	1,648	0,0497	3,02
PLA + 1% graphite	1,69	1,62	1,6	1,73	1,6	1,648	0,0589	3,57
PLA + 2% graphite	1,87	1,91	1,81	1,75	1,82	1,832	0,0610	3,33
PLA + 5% graphite	1,61	1,48	1,48	1,47	1,92	1,592	0,1923	12,08

When examining the diameter of the filaments, it can be seen that the thickness of the filaments varies between 1.48-1.81 mm. The processes were optimized by adjusting the temperature, but due to the aggregation of the graphite powder, a constant 1.75 mm filament could not be produced, the diameter always varied between 1.70-1.80 mm, however, during the FDM test printing, small bodies were produced from these, which will be examined later.



Figure 2. Pure PLA and graphite-enriched PLA fibers (a, 0% graphite + PLA, b, 0.5% graphite + PLA, c, 1% graphite + PLA, d, 2% graphite + PLA, e, 5% graphite + PLA)

PLA's low-temperature processability, high mechanical performance, eco-friendly structure, good surface quality and compatibility with reinforcements made it the final material of choice in this study.

In industrial applications, it can be difficult to maintain a uniform temperature at all points, which can affect the quality consistency of the filament. In particular, homogeneous dispersion of graphite particles into the PLA matrix can be more difficult on a larger scale. In larger extruders, temperature control can be optimized with multi-chamber heating systems. In addition, by using stronger mixing mechanisms, a homogeneous distribution of graphite particles can be achieved. If the filament cannot be completely cooled during high-speed production, rough surfaces and low mechanical strength problems can occur. For fast production lines, additional cooling channels or fans can be installed to ensure adequate cooling of the filaments at the exit point.

3. Results and conclusions

This article presents a study on the production of graphite-reinforced PLA-based composite filament. The aim of the study was to first determine the processing parameters of PLA filaments, produce composite filaments ($\text{\O}1.7\text{-}2.00$ mm) according to these parameters, and then test 3D printing with filaments with different graphite compositions.

According to the study results, the operating temperature, extrusion speed parameters, and the amount of graphite additive have a great influence on the diameter of the filaments. During extrusion, the filament cools down rapidly at the nozzle outlet when exposed to ambient temperature. If the ambient temperature is too low (for example, in an air-conditioned environment or in the case of direct fan cooling), the filament cools down faster, which can lead to the formation of distorted crystal structures.

References

- [1] Duty, C. E., Kunc, V., Compton, B., Post, B., Erdman, D., Smith, R., ... & Love, L. (2017). Structure and mechanical behavior of Big Area Additive Manufacturing (BAAM) materials. *Rapid Prototyping Journal*, 23(1), 181-189.
- [2] G. Sağlam, A. Bedeloğlu - Mechanical properties of thermoplastic filament stitched carbon fiber reinforced composites, *J Innov Sci Eng*, 6 (2) (2022), pp. 248-258, 10.38088/jise.979229
- [3] Gao, S., He, Y., Fu, J., et al. (2019). Additive manufacturing of polymer materials: Progress and prospects.
- [4] Gebhardt, A., Kessler, J., & Thurn, L. (2017). *3D Printing: Understanding Additive Manufacturing*. Hanser Publishers.
- [5] Gibson, I., Rosen, D. W., & Stucker, B. (2021). *Additive manufacturing technologies: 3D printing, rapid prototyping, and direct digital manufacturing (3rd ed.)*. Springer.
- [6] K.K. Jha, T.T.M. Kannan - Recycling of plastic waste into fuel by pyrolysis a review, *Mater Today Proc*, 33 (2) (2020), pp. 755-758, 10.1016/j.matpr.2020.10.181
- [7] Kantaros, A., & Karalekas, D. (2013). Fiber Bragg grating based investigation of residual strains in ABS parts fabricated by fused deposition modeling process. *Materials & Design*, 50, 44-50.
- [8] Khan, M. Tariq, M. Abas, M. Shakeel, F. Hira, A.A. Rashid, et al. - Parametric investigation and optimisation of mechanical properties of thick tri-material based composite of PLA-PETG-ABS 3D-printed using fused filament fabrication, *Composites, Part C: Open Access*, 12 (2023), Article 100392, 10.1016/j.jcomc
- [9] Levenhagen, N. P., & Dadmun, M. D. (2018). Understanding the effect of processing conditions on the morphology and properties of 3D printed poly(lactic acid) parts. *Polymer*, 158, 381-390.
- [10] Li, H., Wang, T., & Yu, Z. (2017). A novel approach to improve mechanical properties of parts fabricated by fused deposition modeling. *Materials & Design*, 105, 152-159.
- [11] Ning, F., Cong, W., Qiu, J., Wei, J., & Wang, S. (2015). Additive manufacturing of carbon fiber reinforced thermoplastic composites using fused deposition modeling. *Composites Part B: Engineering*, 80, 369-378.
- [12] Peng, X., Zhou, L., & Wu, H. (2020). Optimization of polymer extrusion process for filament production. *Journal of Manufacturing Processes*, 58, 465-473.

- [13] Rahim, T. N. A. T., Abdullah, A. M., & Akil, H. M. (2019). Recent developments in fused deposition modeling-based 3D printing of polymers and their composites. *Polymer Reviews*, 59(4), 589-624.
- [14] S. Valvez, P. Santos, J.M. Parente, M.P. Silva, P.N.B. Reis - 3D printed continuous carbon fiber reinforced PLA composites: A short review, *Procedia Struct Integrity*, 25 (2020), pp. 394-399, 10.1016/j.prostr.2020.04.056
- [15] Shanmugam, V., Das, O., Babu, K., Marimuthu, U., Veerasimman, A., Johnson, D. J. and Berto, F. (2021). f, 143, 106032. DOI:10.1016/j.ijfatigue.2020.106007.
- [16] Sun, Q., Rizvi, G., & Bellehumeur, C. (2018). Effect of process parameters on the mechanical properties of fused deposition modeling parts. *Journal of Materials Processing Technology*, 214(3), 691–697.
- [17] Throne, J. L. (2015). *Technology of thermoforming*. Hanser Publishers.
- [18] Turner, B. N., Strong, R., & Gold, S. A. (2014). A review of melt extrusion additive manufacturing processes. *Rapid Prototyping Journal*, 20(3), 192–204.
- [19] Turner, B. N., Strong, R., & Gold, S. A. (2014). A review of melt extrusion additive manufacturing processes: I. Process design and modeling. *Rapid Prototyping Journal*, 20(3), 192-204.
- [20] Wang, T. M., Xi, J. T., & Jin, Y. (2007). A model research for prototype warp deformation in the FDM process. *The International Journal of Advanced Manufacturing Technology*, 33(11-12), 1087-1096.
- [21] X. Wang, L. Zhao, J.Y.H. Fuh, H.P. Lee - Effect of porosity on mechanical properties of 3D printed polymers: Experiments and micromechanical modeling based on X-ray computed tomography analysis *Polymers*, 11 (7) (2019), p. 1144, 10.3390/polym11071154

Comparative vibration level of delta and Cartesian 3D printers: A MATLAB-enable mobile sensor approach

Mahamadou Lamine Ousmane DIALLO¹,  SARANK²,
Tam PATAKI², Lzl ZSIDAI²

¹*Doctoral School of Mechanical Engineering, MATE Gdll*

²*Department of Materials Science and Engineering Processes, Institute of Technology,
Hungarian University of Agriculture and Life Sciences MATE, Gdll MATE Gdll*

Abstract

This study introduces a novel method to measure and compare vibration levels in Cartesian and Delta 3D printers using MATLAB MobileTM as sensor for acceleration data acquisition. While Cartesian and Delta printers are widely utilized in additive manufacturing, their vibration characteristics under similar printing conditions remain unknown. Results revealed that Delta printers exhibited four times greater displacement than Cartesian printers, attributed to kinematic differences in motion control. Significant displacement errors due to sensor underscores the need for specialized sensors in vibration analysis of 3D printers where displacements are small.

Keywords

3D printer, Cartesian, Delta, Vibration, Displacement

1. Introduction

Over the years, 3D printing technology has undergone substantial advancements giving rise to diverse printer designs tailored to different requirements and applications. Cartesian and Delta printers are the two most used configurations in fused deposition modelling (FDM) and other additive manufacturing processes.

Cartesian printers (fig. 1) operate on a cartesian coordinate system which comprises three perpendicular axes: X, Y and Z. The printer head moves along these axes to deposit material layer by layer to achieve the final product. On the other hand, Delta printers (fig. 1), use parallel kinematic system with three arms that moves in a triangular way. Their design permits the print head to move in a spherical coordinate system, enabling faster and more efficient printing. The Delta configuration helps to achieve high speed while cartesian printer are slow and smoother motion, greater production volume, making useful in rapid

prototyping application. (Zhuk & Klotchko, 2024) (Kiranlal et al., 2023) (Schmitt et al., 2018).

Delta printer, generally, produce better surface quality due to the smoother and more continuous motion while cartesian printer tend to have better dimensional accuracy but might show more layer line. The smoother motion of Delta printers can lead to more uniform layer adhesion, potentially improving wear resistance. In Cartesian printers, the wear resistance can vary more significantly with changes in speed and other parameters (Schmitt et al., 2018). Tyagi et al. utilized FEA to evaluate various parameters such as total deformation, equivalent stress, natural frequency and the stiffness of three 3D printers: Cartesian, Polar, and Delta. The conclusion shows that the Cartesian printer presents large deformation and least stiffness, indicating potential challenges in maintaining print quality under loads, Delta printer has faster printing capabilities, but lower stiffness compared to the Polar Printer. The polar printer exhibits the highest stiffness and the least deformation (Tyagi et al., 2024). Pandya also used finite element analysis to find the fundamental frequencies and mode shapes of 3D printed PLA beams alongside an experimental setups (Pandya, 2023).

İpekçi et al. investigated the impact of mechanical improvements on vibration and surface roughness in a Cartesian 3D printer (İpekçi, 2023). Białas et al. to focused on the impact of reducing mechanical vibration in 3D printers on the quality of printed produced by measuring systematically the vibration before and after modification to the printer's structure (Białas et al., 2023). By the method of Białas et al., the amplitude is reduced by 50-70%, which improved the dimensional parameters of printed products. On another hand, Kopets et al. propose a method to estimate the natural frequencies of Cartesian 3D printers based on their kinematic schemes. (Kopets et al., 2022).

Buchalik & Nowak, 2021 discussed the types of sensors utilized in measuring small dimensions and masses (Buchalik & Nowak, 2021) like vibration scanning method. Gomathi et al., used conventional accelerometers, micro-accelerometers, and micro flown sensor to measure the vibrations in 3D printers (Gomathi et al., 2021).

It can be seen through this literature review that no study has compared the vibration level of Delta and Cartesian printers, neither a MATLAB Mobile sensor used to measure the acceleration. This is going to be the object of current study.

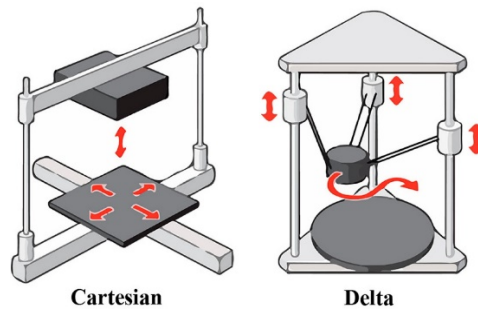


Figure 1: Schematic of Cartesian and Delta Printer (Schmitt et al., 2018)

2. Materials and methods

2.1 Testing geometry

To compare the level of vibration between the Delta and Cartesian printers, two types of geometry were proposed: a pyramid and a cone (fig. 2). These geometries were chosen based on assumption that it brings the printers to change more often position as long as the printing process is going on. Printers performs circular motion for the cone and rectilinear motion for the printing process of the pyramid. The motion is in by the three axes: X, Y and Z. The printed pyramid has the following dimensions: length is equal to 30mm, width 30 mm and the height is 30 mm too. For the cone, the base has 30 mm as diameter while the height is half of the height of the pyramid.

The material used is a Polylactic acid commonly called PLA. The printing parameters on the two machines are similar. The layer height was set at 0.2mm, the infill density was 30%, grid was chosen to be the infill pattern, the print speed was fixed at $40\text{mm}\cdot\text{s}^{-1}$ while the travel speed was three times the print speed.

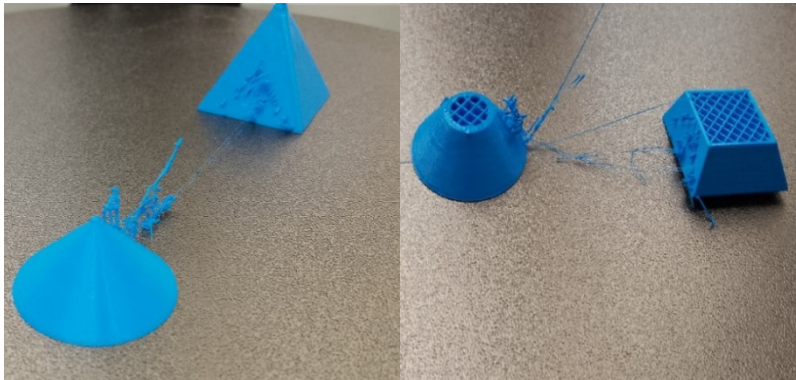


Figure 1 : Printed Specimen

2.2. Measurement method

As we have said above, we have not read any article that compare the vibrations of 3D printers based on their kinematics. So, using a phone where is installed the MATLAB® Mobile™ as sensor data collector to record the acceleration in X, Y, and Z coordinates in meters per second squared. Figure 3 shows the different axis, Y is on the direction of the length of the phone, X is perpendicular to the width of the phone while z axis is perpendicular to the screen of the phone.

To use MATLAB sensor, open the app on your phone, go to ‘Sensors’, then ‘Sampling Parameters’, then ‘Motion Sensors Sample Rate’ to choose the frequency. The range of the frequency goes from 0 – 100Hz. Once this has been done, acceleration recording can be started. Acceleration along the z-axis comprises gravity g. Once recording finished, the data are saved on the MATLAB Drive.

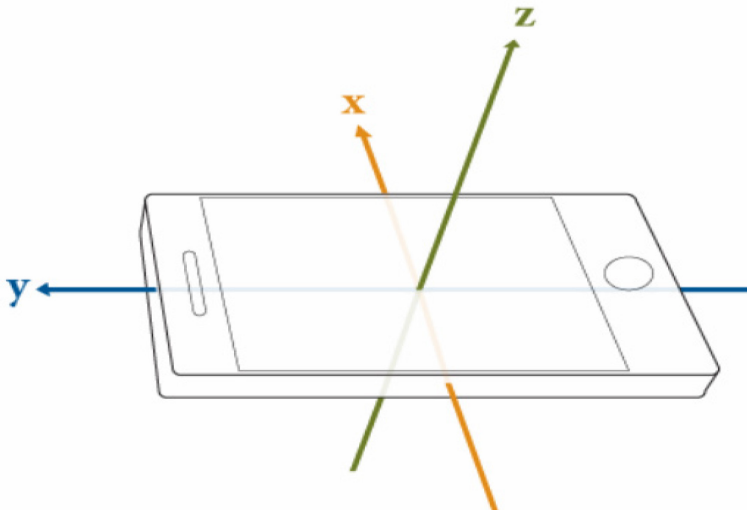


Figure 2 : Device axis orientation

3. Results and discussion

After the acquisition of the data and analyse them using MATLAB code. The objection of the analyse is to find some variables like speed, displacement, the frequency of the printer.

To find variables like speed, displacement, from basic physic, we know that speed is obtained by integrating the acceleration, and the displacement by integrating the speed. By doing so using in-built MATLAB function ‘cumtrapz’, we get the displacement from both accelerations measured for the Delta and Cartesian Printers. The first constat we can get from reading the fig 4 is that the displacement of the Delta is four times greater than the one of Cartesian Printer. Thus, can be understood that the cartesian vibrates less.

The second constat is that this displacement is higher to be believed. As it is noticed on the figure 4, the displacements are not abnormally high. Even after filtering the error by subtracting the mean of the acceleration, it does not help much. The reason behind this is that the MATLAB sensor has a very big bias before any measurement and by this is not good in measuring small displacements as it can be proved by these mathematical equations. From physic, we know that:

$$\begin{aligned} v(t) &= \int a(t)dt \\ &= \int (a_r + bias)dt \\ v(t) &= v_r + bias \times t \quad (eq. 1) \end{aligned}$$

The displacement is found by integrating the speed:

$$\begin{aligned} x(t) &= \int v(t)dt \\ &= \int (v_r + bias \times t)dt \\ x(t) &= x_r + \frac{1}{2}bias \times t^2 \quad (eq. 2) \end{aligned}$$

So, for a bias of 0.01 during 60 seconds, the error would reach:

$$error = \frac{1}{2} \times 0.01 * 60^2 = 18 m$$

It is impossible to calibrate the MATLAB sensor to reduce the error close to zero before any measurement. We can conclude that MATLAB® Mobile™ sensor is not good in measuring small displacement.

After seen this abnormality, we have stopped pursuing further analysis, like finding the higher frequencies for example.

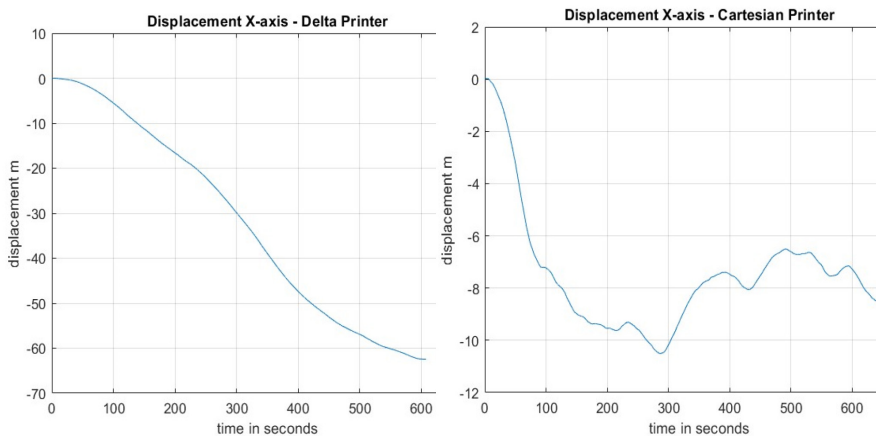


Figure 3 : Displacement of a Delta Printer vs Cartesian

4. Conclusions

In this study, we cover a comparative vibration analysis between Cartesian and Delta 3D printers by using MATLAB® Mobile™ for acceleration measurement. The results demonstrated that Delta printers, despite their faster printing capabilities, produced four times greater displacement than Cartesian printers during comparable printing tasks.

The displacement calculations, derived from double integration of acceleration data, revealed significant challenges in using MATLAB® Mobile™ for vibration analysis. Sensor bias introduced substantial errors, rendering the tool unsuitable for small-displacement measurements critical to additive manufacturing.

References

- [1] Białas, K., Dymarek, A., & Dzitkowski, T. (2023). IMPACT OF 3D PRINTER VIBRATION REDUCTION ON THE QUALITY OF ITS PRINTOUT. *International Journal of Modern Manufacturing Technologies*, 15, 79–90. <https://doi.org/10.54684/ijmmt.2023.15.2.79>
- [2] Buchalik, R., & Nowak, G. (2021). Single-Sensor Vibration-Scanning Method for Assessing the Mechanical Properties of 3D Printed Elements. *Materials*, 14(5), Article 5. <https://doi.org/10.3390/ma14051072>
- [3] Gomathi, K., Ganesh, T., Bharanidharan, J., Arvinth Prajathkar, A. P., & Aravinthan, R. (2021). Condition Monitoring of 3D Printer Using Micro Accelerometer. *IOP Conference Series: Materials Science and Engineering*, 1055(1), 012035. <https://doi.org/10.1088/1757-899X/1055/1/012035>
- [4] Kiranlal, S., Brathikan, V. M., Harish, C. S., Moideen, A. A., & Anandh, B. (2023). Delta 3D Printer—A Review on Electrical Components. In N. M. Sivaram, K. Sankaranarayananasamy, & J. P. Davim (Eds.), *Advances in Manufacturing, Automation, Design and Energy Technologies* (pp. 201–208). Springer Nature. https://doi.org/10.1007/978-981-99-1288-9_21
- [5] Kopets, E., Karimov, A., Scalera, L., & Butusov, D. (2022). Estimating Natural Frequencies of Cartesian 3D Printer Based on Kinematic Scheme. *Applied Sciences*, 12(9), Article 9. <https://doi.org/10.3390/app12094514>
- [6] Pandya, K. (2023). An Experimental and Numerical Investigation Into Vibration of Delaminated 3D Printed PLA Beams [Thesis, Toronto Metropolitan University]. <https://doi.org/10.32920/24625122.v1>
- [7] Schmitt, B. M., Zirbes, C. F., Bonin, C., Lohmann, D., Lencina, D. C., & Netto, A. da C. S. (2018). A Comparative Study of Cartesian and Delta 3D Printers on Producing PLA Parts. *Materials Research*, 20, 883–886. <https://doi.org/10.1590/1980-5373-MR-2016-1039>
- [8] Tyagi, B., Raj, A., Gupta, H., Malik, G., Bhardwaj, L., Sharma, G. S., Uppukoden, J., Sahai, A., & Sharma, R. S. (2024). Modelling Structural Behaviour of the Cartesian, Polar, and Delta Material Extrusion Printers by

- Finite Element Analysis. Journal of The Institution of Engineers (India): Series C, 105, 617–634. <https://doi.org/10.1007/s40032-024-01066-8>
- [9] Zhuk, Y., & Klotchko, T. (2024). COMPARISON OF 3D-PRINTED PARTS' QUALITY USING PRINTERS WITH "COREXY" AND "DELTA" KINEMATICS. Вісник Київського Політехнічного Інституту. Серія Приладобудування, 68(2), Article 68(2). [https://doi.org/10.20535/1970.68\(2\).2024.318630](https://doi.org/10.20535/1970.68(2).2024.318630)

Interdependence of tensile strength and hardness in FDM-Printed PLA: A parametric study

Nejmeddine LAYEB¹, Rihem JEBALI¹, István OLDAL², István Keppler²

Doctoral School of Mechanical Engineering,

*² Department of Machine Construction, Institute of Technology,
Hungarian University of Agriculture and Life Sciences MATE, Gödöllő*

Abstract

Additive manufacturing (AM) using polylactic acid (PLA) and fused deposition modeling (FDM) has emerged as a pivotal technology for producing lightweight, high-strength components with complex geometries. This study investigates the parameters in 3D printing such as layer thickness, nozzle temperature, raster orientation, and the speed of printing, and their effect on tensile strength and hardness of PLA-specimens. The analysis was made using the Taguchi L9 orthogonal array. Results show that layer thickness and raster orientation have significant effects on mechanical properties. Optimum for tensile strength (51 MPa) is obtained at 0.1 mm layer thickness, 210 °C nozzle temperature, 0° raster orientation, and 30 mm/s printing speed. Maximum hardness shore D (80) was achieved with a $\pm 45^\circ$ raster orientation at similar conditions. Further, it was noticed that the hardness and tensile strength are in a proportional relation when the print orientation parameter is the variable.

Keywords

FDM / Parameters optimization / Polylactic acid (PLA) / Hardness/ Tensile strength

1. Introduction

3D printing has become one of the widely known additive manufacturing techniques that builds components layer by layer based on 3D-modeled data considering the diversity of structures and geometries of the objects it produces [1]. Unlike conventional subtractive manufacturing methods, which involve material removal, AM enables intricate design customization, reduces material waste, and enhances production efficiency [2]. The rapid advancements in AM have facilitated its application across various industries, including aerospace, automotive, biomedical. Among the different AM techniques, Fused Deposition Modeling (FDM) is extensively utilized due to its simplicity, cost-effectiveness, and ability to produce functional polymer-based components with a wide range

of material options, such as polylactic acid (PLA), acrylonitrile butadiene styrene (ABS), and polyethylene terephthalate glycol (PETG) polycarbonate, among others [3]. PLA is a widely used material in 3D printing technology due to its easy handling and minimal warping [4]. Besides reduced warping issues, this bio polymer is produced by fermenting agricultural crops like potatoes, maize, or sugar beets [5]. For this reason, PLA is also considered environmentally friendly and is rated by researchers as a biomedical polymer [6,7]. Being produced through utilizing renewable resources, lactic acid-based PLA is also biodegradable. It also possesses a lower melting point of approximately 190-220°C [8,9]. However, the mechanical performance of 3D-printed PLA components is highly influenced by printing parameters such as raster orientation, print speed, layer thickness, nozzle temperature, and infill density. Previous studies have demonstrated that optimizing these parameters is critical for achieving superior tensile strength, hardness, and overall structural integrity. In recent years, numerous studies have focused on demonstrating how optimizing these parameters is critical for achieving superior tensile strength, hardness, and overall structural integrity. Wittbrodt et al. [10] examined how printing temperature affects the tensile strength of 3D-printed PLA components, finding a direct relationship between the two. Their results showed that as the printing temperature increased, so did the tensile strength, with the average breaking stress rising from 53 MPa at 190°C to 59 MPa at 215°C. Similarly, Studies by Song et al. [11], Afrose et al. [12], and Chacon et al. [13] demonstrated that 3D-printed parts with a 0° axial orientation or a 45° angle and 100% infill exhibited superior mechanical properties compared to those with a 90° transverse infill. Specifically, parts printed at 90° were more brittle, lacking a plastic deformation phase in their stress-strain behavior. In contrast, components printed at 0° or 45° displayed greater ductility and an elasto-plastic response under both tensile and compressive loads. Experimental studies on different thermoplastic materials, including PETG and carbon fiber-reinforced composites, have revealed that infill density, deposition rate, and printing orientation are critical factors in optimizing the final product's strength and durability [14]. Additionally, researchers have explored statistical approaches such as the Taguchi design of experiments to systematically evaluate process parameters and their interactions. While several studies have explored the correlation between FDM parameters and hardness, research on optimal conditions and their combined effects remains limited. Leonardo Santana et al. [15] applied Taguchi's experimental design to study the effect of filament diameter, fluidity, and deposition rate on PETG and PLA properties, demonstrating that these factors significantly impact mechanical performance. ANOVA analysis has also been utilized to assess the influence of infill density and feed rate on tensile strength, further supporting the need for parameter optimization in FDM-based fabrication [16]. Kumar et al. [17] found that increasing infill density (80%) and optimizing print speed (60 mm/s) enhanced both tensile strength and hardness. Maguluri et al. [18] reported that higher

extrusion temperatures (220°C) and full infill density (100%) improved layer bonding, achieving the highest Shore D hardness (84.62). In this study, we are investigating the influence of key FDM printing parameters like raster orientation, print speed, layer thickness and nozzle temperature on the tensile strength and hardness of PLA specimens. A Taguchi L9 orthogonal array is employed with Minitab software to systematically analyze the effects of these parameters and determine the optimal conditions for enhanced mechanical properties. Tensile and hardness tests are performed to evaluate the mechanical behavior of the samples, and statistical methods such as ANOVA are applied to assess the significance of each parameter. The findings of this study help deepen the understanding of how FDM printing parameters influence the hardness and tensile properties of PLA components. By analyzing these effects, this research provides valuable insights that can guide future advancements in real-life applications, particularly in the expanding fields of industrial manufacturing and biomedical engineering.

2. Materials and methods

2.1. Materials and Sample preparation

In this study, the biodegradable material used for 3D printing is PLA, designed as per ASTM standards using CAD software. The CAD model was exported to slicing software for preparation. Specimens were manufactured using an FDM-based 3D printer raise pro 3D. The Taguchi method [19,20] with an L9 orthogonal array was employed to optimize process parameters and evaluate their effects on mechanical properties. Four critical printing parameters: printing speed, nozzle temperature, layer thickness, and raster orientation were considered at three levels each as illustrate in Table 1. The fixed parameter levels maintained during specimen preparation are outlined in Table 2. Specimens were fabricated according to ASTM D638 and D785 standards for tensile and hardness tests [21,22], respectively as presented in Figure 1. Shore hardness testing was performed using a durometer to measure material quality, with the higher hardness values indicating improved part strength. The experiments followed the Taguchi design to statistically evaluate the influence of the selected parameters. Table 3 details the various tests conducted according to these configurations. Equation (1) represents the S/N ratio used to identify optimal settings, focusing on maximizing mechanical performance. The results were analyzed to establish the relationship between parameters and the properties of the printed components.

$$SN_i = -10 \log \left[\frac{1}{n} \sum_{i=1}^n \frac{1}{y_i^2} \right] \quad (1)$$

Table 1. The Selected variables and values.

Factors	1	2	3
	Low level	Medium level	High level
A Layer thickness	0.1mm	0.2mm	0.3mm
B Nozzle temperature	200°C	210°C	220°C
C Printing speed	30 mm/s	60 mm/s	90 mm/s
D Raster orientation	0 °	45/-45 °	90 °

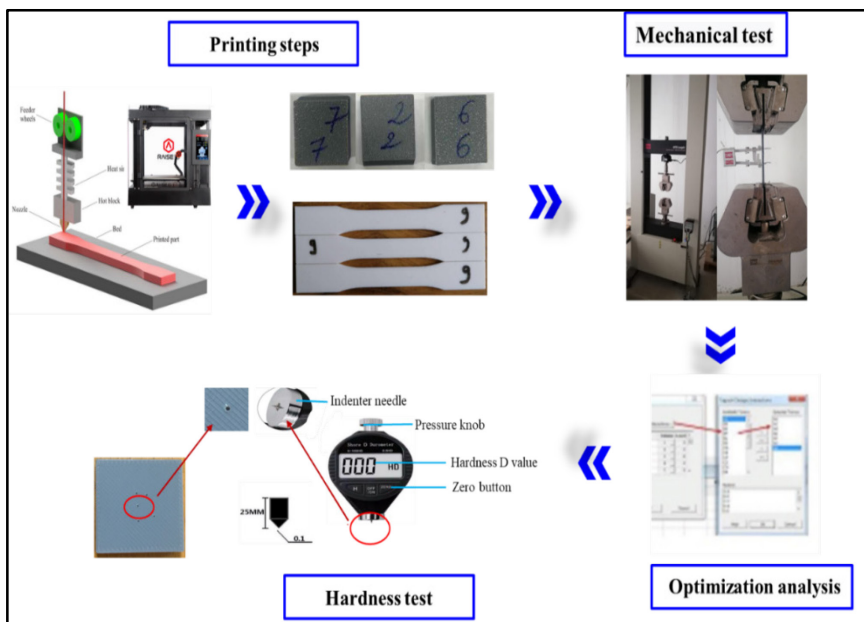


Figure1. Process from 3D printing till mechanical

Table 2. Fixed printing parameters

<u>S.NO</u>	<u>Parameter</u>	<u>Level</u>	<u>Unit</u>
<u>1</u>	Filament diameter (PLA)	1.75	mm
4	Nozzle diameter	0.4	mm
5	Infill pattern	Linear	-
6	Platform temperature	60	°C
8	Build orientation	Flat	-

Table 3. Experimental Taguchi design L9.

No	A	B	C	D
	Layer thickness (mm)	Nozzle Temperature (°C)	Printing speed (mm/s)	Raster orientation (°)
1	0.1	200	30	0
2	0.1	210	60	45/-45
3	0.1	220	90	90
4	0.2	200	60	90
5	0.2	210	90	0
6	0.2	220	30	45/-45
7	0.3	200	90	45/-45
8	0.3	210	30	90
9	0.3	220	60	0

2.2. Mechanical test

The mechanical properties were evaluated using an MTS Insight® electromechanical universal testing machine with a 200 kN load capacity. Tensile tests were performed at a displacement rate of 5 mm/min until specimen failure, as shown in Figure 2. Load and displacement data were recorded at a sampling rate of 100 Hz throughout the tests.

2.3. Hardness measurement

A digital Shore D durometer was utilized to evaluate the hardness of the printed specimens as shown in Figure 1. The instrument features a measuring range of 0–100 HD, a resolution of 0.5 HD, an indenter depth range of 0–2.5 mm, and a test pressure range of 0–45.5 N. To guarantee precise measurements, each specimen was firmly placed on a sturdy slab before testing. During the test, the indenter needle was applied vertically to the specimen, and the hardness value was recorded within the pressure foot making full contact with the specimen surface. Each specimen was tested five times to ensure consistency and reliability of the results.

2.4. Optimization using Taguchi method

To evaluate the influence of key parameters on UTS, tensile strength, and hardness, Figures 3 and 4 depict their effects on both properties. Meanwhile, Tables 4 and 5 rank the input parameters, as determined through analysis using Minitab software.

3. Results and discussion

3.1. Effect of FDM printing parameters on Tensile strength

Figure 2 shows the result of the tensile strength and Figure 3A illustrated that changing the raster orientation from the heights to low level had a positive effect on tensile strength and the same was observed when the nozzle temperature was changed to middle level 210°C. On the other hand, increasing the layer thickness and the printing speed from low to high level resulted in tensile strength decrease. According to Table 4, raster orientation had the greatest impact on tensile strength, leading to an average increase of 48%. Layer thickness followed as the second most influential factor, contributing to a 13% increase. Nozzle temperature, ranked third, caused a decrease in tensile strength from 33 MPa to 30 MPa when increased from low to high settings, with an average reduction of 2.4 MPa. Lastly, printing speed resulted in a 4% increase in tensile strength.

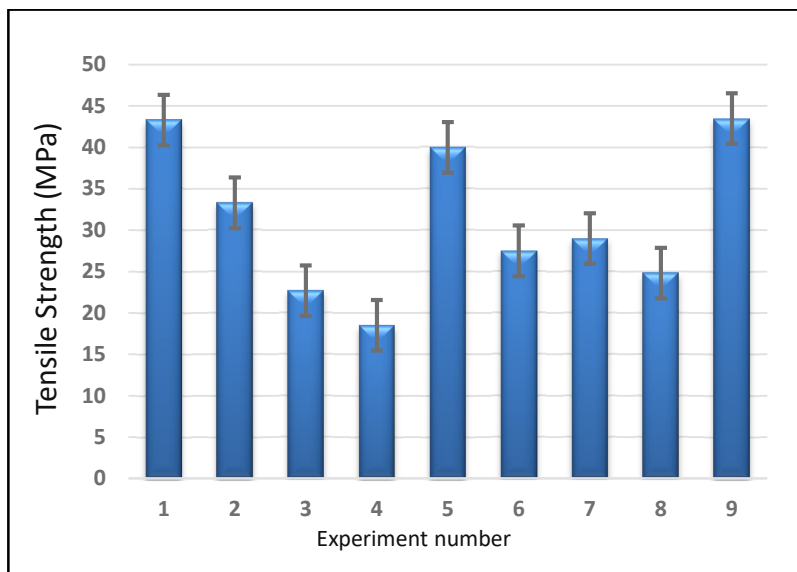


Figure 2. Tensile strength (Mpa)

Table 4. Minitab-Identified Input Parameters Influencing Tensile Strength

Level	Layer thickness (mm)	Nozzle temperature (°C)	Printing speed (mm/s)	Raster orientation (°)
1	33,11	30,29	31,84	42,26
2	28,67	32,69	31,78	29,92
3	32,39	31,19	30,55	21,98
Delta	4,442	2,41	1,29	20,28
Rang	2	3	4	1

The interaction plot in Figure3 B illustrates the relationship between tensile strength and key FDM parameters: raster orientation, layer thickness, nozzle temperature, and printing speed, highlighting notable interaction effects. In the plot, non-parallel trend lines provide strong evidence of interaction, particularly between raster orientation and printing speed. For example, at a 0° raster orientation, tensile strength decreases as printing speed increases, likely due to reduced interlayer adhesion caused by faster deposition rates. Similarly, significant improvements in tensile strength are observed when raster orientation is adjusted from 90° to 0°, especially in combination with a layer thickness of 0.1 mm and a printing speed of 30 mm/s. A linear regression analysis was conducted to establish a predictive relationship for tensile strength based on these parameters. The regression equation, presented in equation 2 and table 5, offers a reliable method for estimating tensile strength for specific FDM settings. The coefficient of determination underscores the strength of this model, confirming a robust correlation between tensile strength and the FDM parameters. Layer thickness, Nozzle Temperature, Printing Speed, and Raster Orientation are denoted by A, B, C, and D, respectively

Regression Equation (2):

$$\begin{aligned} \text{Tensile} = & 31.40 + 1.700 A_{.0.1} - 2.733 A_{.0.2} + 1.033 A_{.0.3} - 1.133 B_{.200} \\ & + 1.300 B_{.210} - 0.1667 B_{.220} + 0.4667 C_{.30} + 0.3667 C_{.60} - \\ & 0.8333 C_{.90} + 10.87 D_{.0} - 1.467 D_{.45} - 9.400 D_{.90} \end{aligned}$$

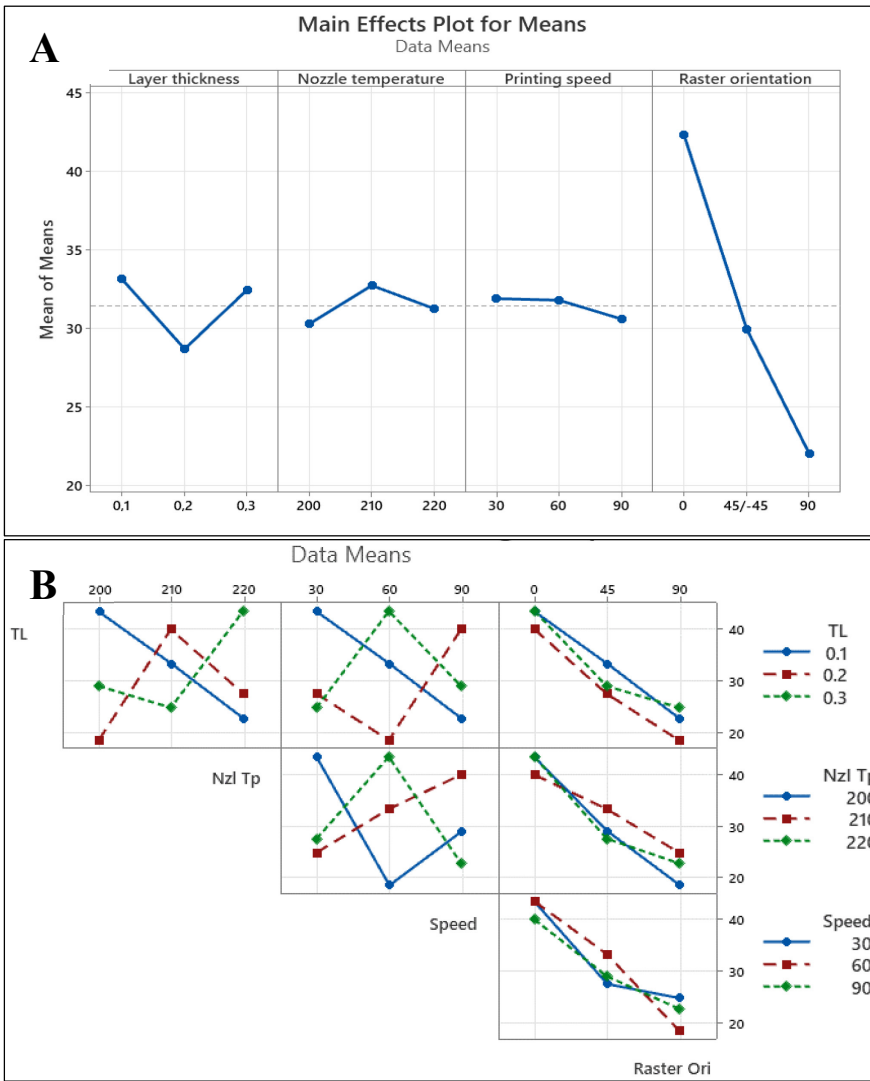


Figure 3. Main effects parameters on the: A) tensile strength, B) Interaction Plot for Tensile

Table 5. ANOVA model for shore D hardness

R-sq	R-sq(adj)	R-sq(pred)
98.19%	96.39%	90.85%

3.2. Effect of FDM printing parameters on PLA material hardness (Shore D)

Shore hardness evaluates a material's resistance to indentation using a durometer with a specialized indenter tip. This tip extends 2.54 mm below the flat presser foot, with the indentation depth determined by the polymer's hardness and viscoelastic properties. For Shore D hardness, the ASTM D2240 test method specifies a sharp conical indenter and a stiff spring. When pressure is applied, the durometer measures the indenter's position relative to the presser foot and calculates the hardness value based on the correlation defined in Equation 3 of the instrument manual:

$$\text{Hardness (Shore D)} = 100 - \left[\frac{L}{0.025} \right] \quad (3)$$

Where L represents the indenter's displacement.

Table 6 presents the measured hardness values along with their means and standard deviations.

Table 6. Hardness results

Exp	Hardness (shore D)					Min.	Max.	Mean	StDev
	1	2	3	4	5				
1	75.5	75.5	73.5	76.0	76.0	73.5	76.0	75	0.978
2	77.0	77.5	77.0	78.5	77.5	77.0	78.5	77.5	0.500
3	75.5	75.5	76.5	76.5	76.0	75.5	76.5	75.5	0.400
4	76.0	75.0	76.0	73.0	73.0	73.0	76.0	74.5	1.500
5	74.5	74.5	73.5	72.0	72.5	72.0	74.5	73.0	1.020
6	78.5	78.0	76.5	79.5	77.5	76.5	79.5	78.0	1.000
7	73.0	73.5	72.0	74.5	73.5	72.0	74.5	73.5	0.790
8	73.0	75.0	75.0	74.0	74.5	73.0	75.0	74.5	0.683
9	66.5	69.5	70.0	70.0	66.5	66.5	70.0	68.5	1.443

Figure 4A presents the effects of the process parameters on the hardness of FDM-printed PLA parts. The results indicate that decreasing the layer thickness from 0.3 mm to 0.1 mm significantly enhances hardness, mainly by improving interlayer adhesion and minimizing void formation. Similarly, altering the raster orientation from 0° or 90° to ±45° had a positive impact by promoting uniform load distribution and stronger bonding at the layer interfaces. Printing speed also influenced hardness, with a lower speed of 30 mm/s providing smoother filament deposition and better interlayer bonding. Among the temperature levels, the middle value of 210°C was found to be optimal, ensuring a balance between filament liquidity and adhesion quality. According to Table 7, layer thickness

was the most influential parameter, with a Delta value of 3.67, followed by printing speed (3.00), nozzle temperature (2.33), and raster orientation (1.67). The higher Delta values for layer thickness and printing speed emphasize their critical roles in determining hardness, while nozzle temperature and raster orientation contributed more subtle, yet still significant, improvements.

Figure 4B highlights the interaction effects among the parameters. The non-parallel lines in the interaction plot indicate strong interactions, particularly between layer thickness and raster orientation. The combination of 0.1 mm layer thickness and $\pm 45^\circ$ raster orientation consistently yielded the highest hardness values, illustrating the synergistic effects of these settings. The interaction between layer thickness and printing speed also demonstrated a clear trend, with slower printing speeds further enhancing the mechanical properties when combined with thinner layers yielding the highest hardness values 77.5 and 78.0 the same in the literature reported that changing parameters can improve the hardness value for PLA [18,23,24].

Table 7. Input Parameters Affecting Hardness D

Level	Layer thickness (mm)	Nozzle temperature (°C)	Printing speed (mm/s)	Raster orientation (°)
1	74.00	70.67	73.67	72.67
2	71.67	73.00	70.67	72.33
3	70.33	72.33	71.67	71.00
Delta	3.67	2.33	3.00	1.67
Rang	1	3	2	4

As show in Figure 5, the maximum response values are represented by deep green regions colour, while minimum response values are represented by light green regions. Maximum Hardness value i.e. more than 74 which is visible as deep green coloured regions when print speed varied from 90 to 30 mm/sec, raster orientation from 0 to 45 degree and layer height from 0.3mm to 0.1mm.

Table 8. ANOVA results for shore D hardness

Parameter	DOF	Sum of squares	Means squares	Contribution
Layer thickness	2	24.389	12.1944	39.51%
Printing speed	2	9.056	4.5278	14.67%
Raster orientation	2	26.722	13.3611	43.29%
Error	2	1.556	0.7778	2.52%
Total	8	61.722		100%

To establish a relationship between the hardness of a 3D printed component and the previously mentioned factors, a linear regression analysis was conducted. The relationship presented in Equation 4, Table 8 and 9 can be used to predict the estimated value of hardness for chosen printing parameters in the FDM method. A coefficient of determination signifies the relationship strength of outcome hardness and FDM printing parameters.

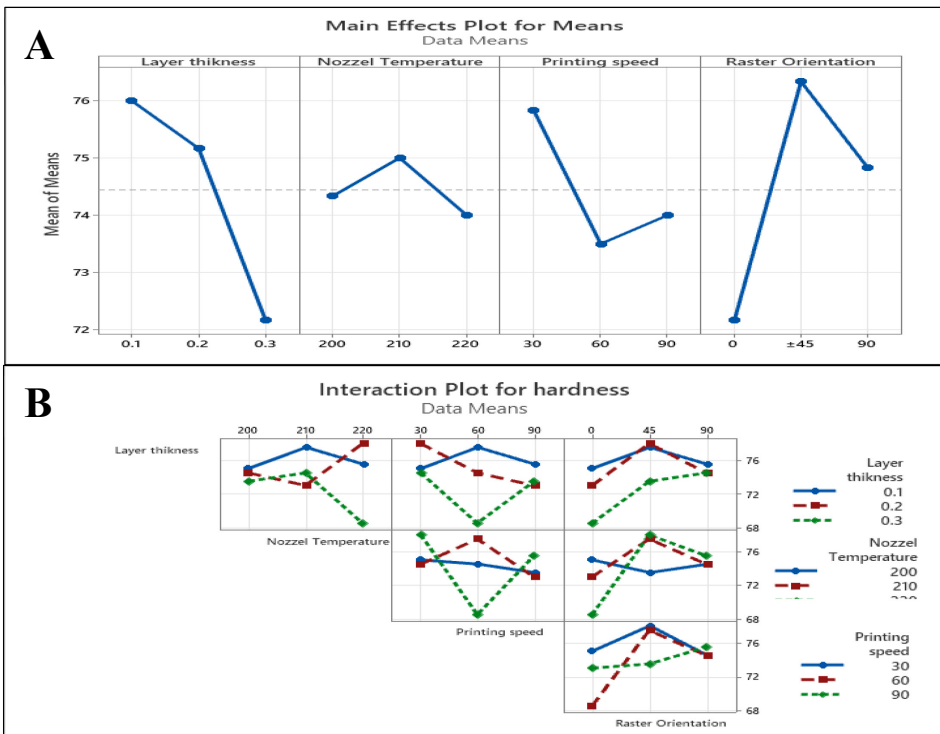
Regression equation Shore D Hardness (4):

$$\begin{aligned} \text{Hardness} = & 74.44 + 1.556 A_{.0.1} + 0.7222 A_{.0.2} - 2.278 A_{.0.3} - \\ & 0.1111 B_{200} + 0.5556 B_{210} - 0.4444 B_{220} + 1.389 C_{30} \\ & - 0.9444 C_{60} - 0.4444 C_{90} - 2.278 D_{0} + 1.889 D_{45} \\ & + 0.3889 D_{90} \end{aligned}$$

Table 9. ANOVA model for shore D hardness

R-sq	R-sq(adj)	R-sq(pred)
97.48%	89.92%	55.63%

Figure 4. Main effects parameters on the: A) Hardness, B) Interaction Plot for Hardness



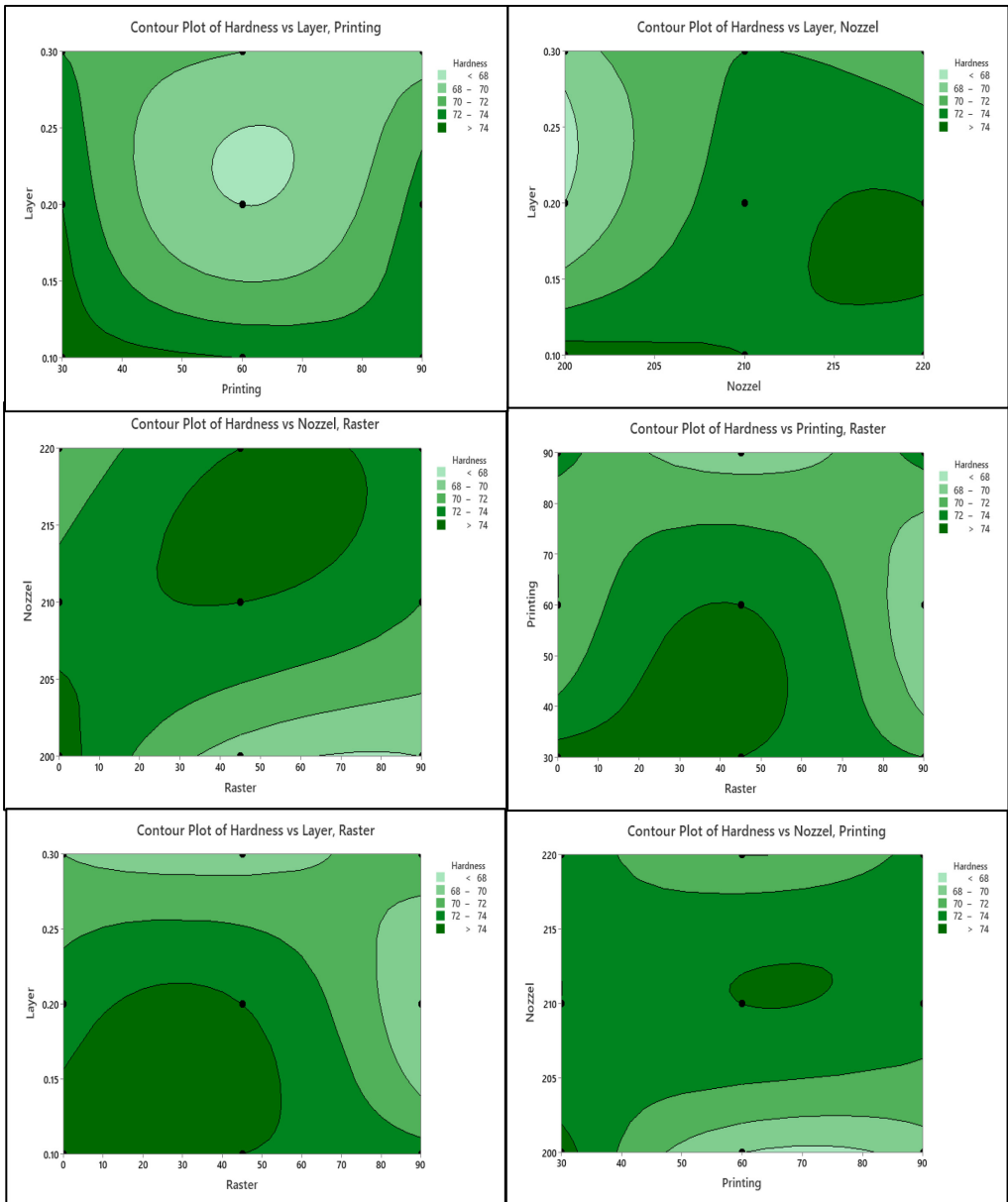


Figure 5. Contour plots response for the hardness test

3.3. Multiple response optimization: tensile strength and hardness

To examine the accuracy of the Taguchi technique in predicting tensile and hardness, the sample was prepared and tested according to equation number 1 and input optimal parameters results from Figure 3 and 4 with 0.1 mm layer 210 nozzle temperature 30mm/s printing speed and 0-degree orientation for tensile and ± 45 degree for hardness. Figure 6 shows the new measured indentation of the 3D printed PLA sample and the tensile curve. The mean values of hardness (Shore D) and tensile strength were 80 and 51 MPa, respectively. The observed values showed a variance when compared to those predicted using the Taguchi technique. Therefore, the Taguchi DOE has proven to be a reliable approach for predicting the mechanical characteristics of 3D printed models produced with the FDM process, demonstrating high accuracy.

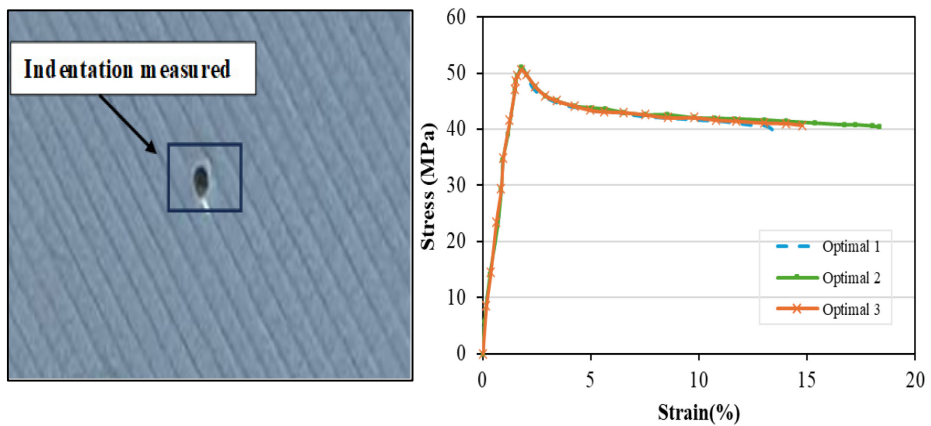


Figure 6. New measured indentation and tensile curves

Conclusions

This study investigated the mechanical performance of 3D-printed PLA through experimental evaluation of tensile strength and hardness properties, utilizing a Taguchi L9 fractional factorial design. Nine experimental runs were conducted, each with three specimens tested for tensile properties and five for hardness, analyzing the influence of key process variables: layer thickness, nozzle temperature, raster orientation, and printing speed.

The findings revealed that:

1. The optimum parameters for maximizing tensile strength were a layer thickness of 0.1 mm, nozzle temperature of 210°C, raster orientation of 0°, and printing speed of 30 mm/s. Among these, raster orientation and layer thickness emerged as the most influential factors in enhancing tensile properties.

2. For hardness, the optimal settings were a layer thickness of 0.1 mm, nozzle temperature of 210°C, raster orientation of $\pm 45^\circ$, and printing speed of 30 mm/s.

3. The ideal parameter combinations resulted in significant mechanical improvements, with tensile strength increasing from 40 MPa to 51 MPa and hardness improving from 68.5 to 80.

References

[1]. Zhou, L., Miller, J., Vezza, J., Mayster, M., Raffay, M., Justice, Q., Tamimi, Z. A., Hansotte, G., Sunkara, L. D., & Bernat, J. (2024). Additive Manufacturing: A Comprehensive review. *Sensors*, 24(9), 2668. <https://doi.org/10.3390/s24092668>

[2]. A. Alafaghani and A. Qattawi, "Investigating the effect of fused deposition modeling processing parameters using Taguchi design of experiment method," *J. Manuf. Process.*, vol. 36, no. December 2017, pp. 164–174, 2018, doi: 10.1016/j.jmapro.2018.09.025.

[3]. M. Dawoud, I. Taha, and S. J. Ebeid, "Mechanical behaviour of ABS: An experimental study using FDM and injection moulding techniques," *J. Manuf. Process.*, vol. 21, pp. 39–45, 2016, doi: 10.1016/j.jmapro.2015.11.002.

[4]. Grosso, P.; Cejudo, C.; Sánchez-Gomar, I.; Durán-Ruiz, M.; Moreno-Luna, R.; Casas, L.; Pereyra, C.; Mantell, C. Supercritical Impregnation of Mango Leaf Extract into PLA 3D-Printed Devices and Evaluation of Their Biocompatibility with Endothelial Cell Cultures. *Polymers* 2022, 14, 2706. <https://doi.org/10.3390/polym14132706>

[5]. Bajpai, P.K.; Singh, I.; Madaan, J. Tribological behavior of natural fiber reinforced PLA composites. *Wear* 2013, 297, 829–840. <https://doi.org/10.1016/j.wear.2012.10.019>

[6]. de França, J.O.C.; da Silva Valadares, D.; Paiva, M.F.; Dias, S.C.L.; Dias, J.A. Polymers Based on PLA from Synthesis Using D,L-Lactic Acid (or Racemic Lactide) and Some Biomedical Applications: A Short Review. *Polymers* 2022, 14, 2317. <https://doi.org/10.3390/polym14122317>

[7]. Singhvi MS, Zinjarde SS, Gokhale D. Polylactic acid: synthesis and biomedical applications. *J Appl Microbiol.* 2019;127:1612-1626. <https://doi.org/10.1111/jam.14290>

[8]. Joseph TM, Kallingal A, Suresh AM, et al. 3D printing of polylactic acid: recent advances and opportunities. *Int J Adv Manuf Technol.* 2023;125(3-4):1015-1035. doi:10.1007/s00170-022-10795-y

[9]. X. Zhou, S.-J. Hsieh, Y. Sun, Experimental and numerical investigation of the thermal behaviour of polylactic acid during the fused deposition process,

Virtual Phys. Prototyp.12, 221–33 (2017).
<https://doi.org/10.1177/07316844231167551>

[10]. B. Wittbrodt, J.M. Pearce, The Effects of PLA Color on Material Properties of 3-D Printed Components, *Addit. Manuf.* (2015). doi:10.1016/j.addma.2015.09.006.

[11]. Y. Song, Y. Li, W. Song, K. Yee, K.Y. Lee, V.L. Tagarielli, Measurements of the mechanical response of unidirectional 3D-printed PLA, *Mater. Des.*123(2017)154–164. doi:10.1016/j.matdes.2017.03.051.

[12]. M.F. Afrose, S.H. Masood, M. Nikzad, P. Iovenitti, Effects of Build Orientations on Tensile Properties of PLA Material Processed by FDM, *Adv. Mater. Res.* 1044–1045 (2014) 31–34. doi:10.4028/www.scientific.net/AMR.1044-1045.31.

[13]. J.M. Chacón, M.A. Caminero, E. García-Plaza, P.J. Núñez, Additive manufacturing of PLA structures using fused deposition modelling: Effect of process parameters on mechanical properties and their optimal selection, *Mater. Des.* 124 (2017) 143–157. doi:10.1016/j.matdes.2017.03.065.

[14]. Cesar O. Balderrama - Armendariz, Eric MacDonald, Esdras D. Valadeza, David Espalin.: Folding endurance appraisal for thermoplastic materials Printed in fusion deposition technology. *Solid Freeform Fabrication: Proceedings of the 27th Annual International, Solid Freeform Fabrication Symposium – An Additive Manufacturing Conference* (2016).

[15]. Gabriel A. Johnson, Jesse J. French, Evaluation of infill effect on mechanical properties of consumer 3D printing materials, *Adv. Technol. Innov.* 3 (4) (2018) 179–184.

[16]. Leonardo Santana, Jorge Lino Alves, Aurélio da Costa Sabino Netto, Dimensional analysis of PLA and PETG parts built by open source extrusion- based 3D printing. 10th Brazilian Congress on Manufacturing Engineering August 05th-07th (2019).

[17]. Kumar, MA, Khan & Mishra, SB 2020, “Effect of machine parameters on strength and hardness of FDM printed carbon fiber reinforced PETG thermoplastics,” *Materials Today Proceedings*, 27975–983, <https://doi.org/10.1016/j.matpr.2020.01.291>.

[18]. Maguluri, N, Suresh, G & Guntur, SR 2022, “Effect of printing parameters on the hardness of 3D printed poly-lactic acid parts using DOE approach,” *IOP Conference Series Materials Science and Engineering*, 1248(1):012004, <https://doi.org/10.1088/1757-899x/1248/1/012004>.

[19]. Song H, Dan J, Li J, et al. Experimental study on the cutting force during laser-assisted machining of fused silica based on the Taguchi method and response surface methodology. *J Manuf Process* 2019; 38: 9–20.

[20]. Mahapatra SS and Patnaik A. Optimization of wire electrical discharge machining (WEDM) process parameters using Taguchi method. *Int J Adv Manuf Technol* 2007; 34: 911–925.

[21]. Heidari-Rarani M, Rafiee-Afarani M, Zahedi AM, Mechanical characterization of FDM 3D printing of continuous carbon fiber reinforced PLA

composites, *Composites Part B* (2019), doi: <https://doi.org/10.1016/j.compositesb.2019.107147>.

[22]. Soundararajan, R., Dharunprakash, E., Arjunkumaar, N. et al. Appraisal of Mechanical and Tribological Performance of Onyx and Carbon Fiber Composites Produced Through Various Layering Approaches in Continuous Fused Filament Fabricated. *J. Inst. Eng. India Ser. D* (2024). <https://doi.org/10.1007/s40033-023-00626-z>

[23]. Ansari, A. A., & Kamil, M. (2022). Izod impact and hardness properties of 3D printed lightweight CF-reinforced PLA composites using design of experiment. *International Journal of Lightweight Materials and Manufacture*, 5(3), 369-383. <https://doi.org/10.1016/j.ijlmm.2022.04.006>

[24]. Hanon, M. M., Dobos, J., & Zsidai, L. (2020). The influence of 3D printing process parameters on the mechanical performance of PLA polymer and its correlation with hardness. *Procedia Manufacturing*, 54, 244-249. <https://doi.org/10.1016/j.promfg.2021.07.038>

Development and evaluation of a robotics system for plant health analysis and irrigation control

Feliciano SAMPAIO¹, Zoltán Bártfai²

¹ *Doctoral School of Mechanical Engineering,*

Hungarian University of Agriculture and Life Sciences MATE, Gödöllő

² *Department of Farm and Food Machinery, Institute of Technology, MATE Gödöllő*

Abstract

This research presents the development of a robotic system integrated with a Python-based program for plant health analysis and automated irrigation control. The system employs a multi-spectral sensor to capture electromagnetic interactions of sunlight with plants, leveraging machine learning models to classify plant health status and adjust irrigation accordingly. This report details the robot's software structure, decision-making processes, sensor integration, and potential improvements for real-world applications. The study also explores the potential scalability of the system for large-scale agricultural use and integration with IoT-based remote monitoring.

Keywords

Robotics, Agriculture, Machine Learning, Plant Health, Automated Irrigation, IoT

1. Introduction

Agricultural robotics plays a crucial role in precision farming, enhancing productivity and sustainability through automation. This research focuses on the development of a robot capable of assessing plant health and executing irrigation decisions based on spectral data analysis. The core innovation lies in the integration of machine learning algorithms with real-time sensor data to ensure accurate and efficient water distribution. The study also evaluates the feasibility of expanding the system to support predictive analytics and remote monitoring via cloud-based solutions.

During the preparations, we conducted a trial measurement on commercially available C45 material quality to test the measurement method and necessary technical conditions. During the trial measurements, we examined the relationship between different machining settings, machining temperature, and surface roughness.

In this study, we present the results of the trial measurements and provide detailed explanations of the measurements and analyses carried out during the machining process. We will reference previous research and expert opinions in order to provide readers with appropriate and reliable results. In the following chapters, we will present in detail the methods, results, and conclusions of the trial measurements.

2. Materials and methods

The robotic system comprises:

- A multi-spectral sensor (camera) for capturing plant reflectance data.
- Python-based software handling data processing, model predictions, and actuator control. The core of the program, encapsulating the robot's logic.

Below is an outline of the software and commands. Figure 1 and 2 show the program.

```

1 Agrobot AI
2
3 ## Overview
4
5 This project involves a robot equipped with a multispectral sensor that captures the interaction between solar energy and plants. The robot uses a camera (multi-spectral sensor) to measure the reflected light
6 and makes decisions for optimal plant care, including irrigation. The primary aim is to monitor plant health, assess their condition, and apply irrigation based on their needs.
7
8 ## Components
9
10 1. **Robot**: The main controller of the robot, which handles loading data, interacting with the sensor, and making decisions based on predictive models.
11 2. **Sensor (Multi-Spectral)**: Captures reflected light in various spectral bands (e.g., Red, Green, Blue, Near-Infrared).
12 3. **Data Processing**: The robot uses the data captured from the sensor to calculate vegetation indices like NDVI (Normalized Difference Vegetation Index) to assess plant health.
13 4. **Model**: A predictive model that classifies plant conditions as "Healthy", "Stressed", or "Unhealthy" based on the captured data.
14 5. **Irrigation Control**: The robot makes irrigation decisions based on the plant condition and applies an irrigation percentage (50%, 75%, 100%).
15
16 ## File Structure
17
18 ...
19
20 /project-directory
21 ├── robot.py           # Main robot logic
22 ├── sensor.py         # Sensor class for capturing reflected light
23 ├── utils.py          # Helper functions (e.g., data reading, model loading)
24 └── README.md         # Documentation for the project
25
26 ## Setup
27
28 1. **Clone the Repository**:
29    If you're working with a version-controlled repository, you can clone it as follows:
30
31    ...
32    ```bash
33    git clone https://github.com/Altrobotics/agrobot-ai
34    cd agrobot-ai
35    ...
36
37 2. **Install Dependencies**:
38    ...
39    ```bash
40    pip install -r requirements.txt
41    ...
42
43 3. **Configure Sensor and Model**:
44    Ensure that you have access to or configure the sensor hardware and models for your specific use case. The load_model function should load a trained machine learning model for plant health classification
45
46 ## Components and Usage
  
```

Figure 1. Program

```

The 'Sensor' class simulates a multispectral sensor that captures reflected light in different spectral bands.

**Constructor**:
- __init__(bands): Initializes the sensor with a list of spectral bands (e.g., Red, Green, Blue, NIR).

**Methods**:
- capture_reflected_light(): Simulates the capturing of reflected light across the defined spectral bands, returning random reflectance values between 0 and 1.

### 3. **Utility Functions**

These helper functions facilitate data loading, model loading, and prediction:

- **read_data()**: Reads the sensor data or a dataset, possibly from a file or database.
- **load_model()**: Loads a pre-trained model to make predictions about plant health.
- **make_prediction(model, data)**: Uses the model to predict plant health based on the data.

## Example Usage

```python
from robot import Robot

Initialize and start the robot
robot = Robot()
robot.start()
```

The 'start()' method begins the robot's continuous monitoring and decision-making loop. It will capture sensor data, process it, and make irrigation decisions accordingly.

## Example Output



```

plaintext
Condition: Healthy
Irrigating at 50%
Condition: Stressed
Irrigating at 75%
Condition: Unhealthy
Irrigating at 100%

```


```

Figure 2. Program

__init__(self): The constructor initializes the robot by loading data and a pre-trained model, creating an empty list index (likely for storing vegetation indices), and instantiating a Sensor object.

load_data (self): Loads data using the read_data() function from the utils module. The exact format and source of this data are not clear from the provided code, but it likely contains information relevant to plant health (e.g., sensor readings, spectral data).

load_model (self): Loads a pre-trained machine learning model using the load_model() function from the utils module. This model is presumably used to predict plant health.

Start (self): The main loop of the robot's operation. It continuously captures reflected light data from the sensor, decides based on the data, and then pauses for 1 second.

get_ndvi (self, red_band, near_infrared_band): Calculates the Normalized Difference Vegetation Index (NDVI) from red and near-infrared light readings. NDVI is a common metric used to assess vegetation health.

vegetation_indices (self): Calculates NDVI for a set of input data (presumably spectral bands). The current implementation has a bug: it calls get_ndvi with a single argument x but get_ndvi expects two arguments (red_band, near_infrared_band). This will cause a TypeError. The map function

is also not being used correctly; it should pass two arguments to the `get_ndvi` function.

take_decision(self): Uses the loaded model to make a prediction about plant health based on the loaded data. It prints the prediction ("Healthy", "Stressed", or "Unhealthy") and then calls `do_irrigate()` with different percentages based on the prediction.

do_irrigate(self, percentage): Simulates irrigation by printing a message indicating the irrigation percentage. In a real-world scenario, this method would likely control actuators to perform actual irrigation.

control(self): This method is currently empty and does nothing. It's likely intended to control other robot actuators based on the decisions made, beyond just irrigation. The program is shown in figure 3 below.

```

main.py
1 from robot import Robot
2
3 if __name__ == "__main__":
4     robot = Robot()
5     robot.start()

```

```

python3 main.py
Data preview:
  RED  NIR  NDVI
0  0.2  0.7  0.556
1  0.3  0.6  0.333
2  0.1  0.8  0.778
3  0.4  0.3  0.111
4  0.2  0.3  0.600
Condition: Healthy
Irrigating at 50%
Irrigating at 20%
Condition: Healthy
Irrigating at 50%

```

Figure 3. The main .py Terminal

- A machine learning model for classifying plant health into three categories: Healthy, Stressed, Unhealthy.
- A decision-making module that adjusts irrigation levels based on predictions as shown in figure 4 below.

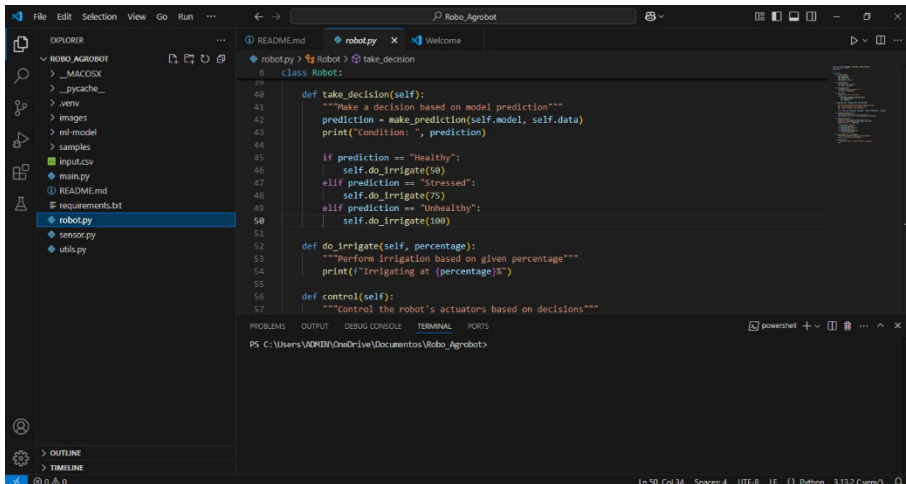


Figure 4. Decision making module

- An optional IoT module for remote data transmission and monitoring.

3. Results and discussion

The program successfully classified plant health and adjusted irrigation levels. As shown in figure 5 below.

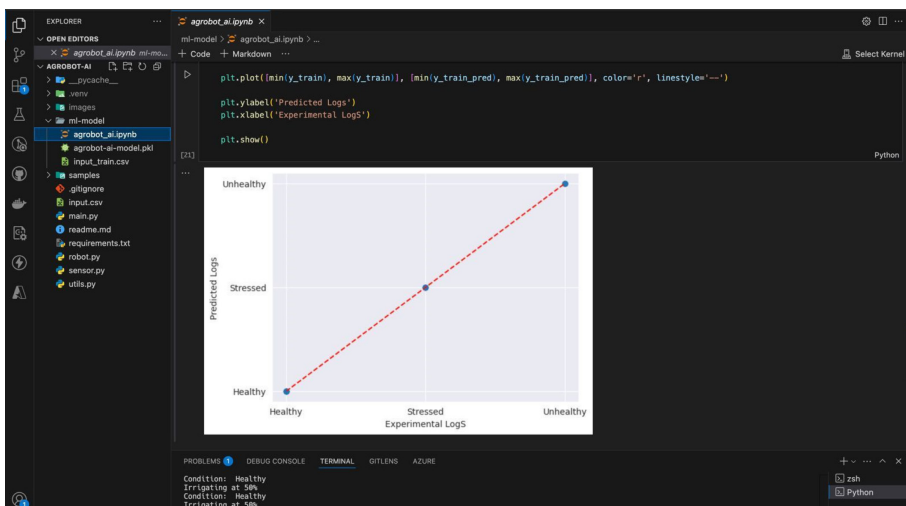


Figure 5. Plant classification into categories

While the program was able to classify the plants into three categories, certain challenges were identified:

- **Bug in vegetation indices ()**: Incorrect parameter passing caused a TypeError, requiring function revision.
- **Empty control () method**: Intended for broader robotic actuation beyond irrigation but currently unimplemented.
- **Data Format Uncertainty**: The structure of input data needs clarification for model training and refinement.
- **Error Handling**: The absence of exception handling mechanisms for sensor failures and data inconsistencies.
- **Cloud Connectivity Enhancements**: The IoT integration can be further improved to support automated alerts and predictive maintenance features.

4. Conclusion

This research presents a robotic system capable of plant health monitoring and automated irrigation. While the system effectively classifies plant conditions and adjusts irrigation, further refinement is needed to address function bugs, enhance control mechanisms, and improve data handling. The integration of IoT-based solutions has the potential to extend the system's capabilities for large-scale agricultural applications. Future work will focus on real-world testing, predictive analytics, and full-scale IoT integration.

References

- [1] Bergerman, M., Van Henten, E., Billingsley, J., Reid, J., & Mingcong, D. (2013). IEEE robotics and automation society technical committee on agricultural robotics and automation. *IEEE Robotics & Automation Magazine*, 20(2), 20-23.
- [2] Mahmud, M. S. A., Abidin, M. S. Z., Emmanuel, A. A., & Hasan, H. S. (2020). Robotics and automation in agriculture: present and future applications. *Applications of Modelling and Simulation*, 4, 130-140.
- [3] R Shamshiri, R., Weltzien, C., Hameed, I. A., J Yule, I., E Grift, T., Balasundram, S. K., ... & Chowdhary, G. (2018). Research and development in agricultural robotics: A perspective of digital farming.

Experimental set-up of Sand-Pot Device for 3-body abrasive wear testing

Bahram TURAPOV¹, Gábor KALÁCSKA¹, Róbert KERESZTES²

¹ *Doctoral School of Mechanical Engineering,*

Hungarian University of Agriculture and Life Sciences, MATE, Gödöllő

² *Department of Materials Science and Engineering Processes,
Institute of Technology, MATE, Gödöllő*

Abstract

A thorough understanding of the abrasive nature of lunar regolith is crucial for mitigating the damage to mechanical components during lunar missions. This paper describes in detail the 3-body abrasive wear testing procedure of 1.4404 (EN) steel grade shaft and natural PTFE lip seal rotating pair in a sand-pot test device. Fraction 4 of the five predefined particle size fractions from the LX-TH100 Lunar highland simulant was used to demonstrate the testing procedure for a distinct particle size. The study outlines the torque variations in the rotating shaft/seal mechanism caused by abrasive wear. This research paper will serve as a guideline for future tests to compare the trend lines of the torque changes and running distances in the case of different fractions. To replicate Lunar conditions, future experiments will employ a custom-built pin-on-disc tribo-test rig in addition to a sand-pot test rig. Furthermore, the findings will be used to calibrate the model, reduce the margin of error and validate the results in Discrete Element Modelling.

Keywords

Lunar regolith, abrasive wear, tribological model, particle size fractions.

1. Introduction

The main challenge in Lunar exploration projects is the abrasive wear process caused by lunar regolith. The geometric, mechanical, and adhesion characteristics of lunar dust are different from those of dust under the earth's environment (Gaier & Berkebile, 2012; Li et al., 2023). Approximately one-fifth of the lunar regolith layer is less than 20 μm which is categorized as a lunar dust (Kawamoto, 2014; Zanon et al., 2023). Its extremely abrasive nature is caused by a lack of erosion on the moon's surface, micrometeorite bombardments, silicate content, and electrostatic charging (Nikki Welch, 2021; Zanon et al., 2023). Seals, shafts, axles, interlocks, joints, and airlocks are among the

structural elements harmed by lunar dust abrasion (Gaier & Berkebile, 2012). Tribological parts only account for a small portion of the total cost of the spacecraft, but they frequently cause malfunctions that threaten the mission by disrupting the spacecraft either totally or partially (Mukhtar et al., 2023).

Recent studies have employed numerical modelling to predict the abrasive wear of mechanical parts in space exploration (Afshar-Mohajer et al., 2015; Li et al., 2023). Numerical modelling is a promising, cost- and time-effective approach (Valerie Wiesner, 2024) for assessing and predicting the abrasive nature of lunar regolith. Methods such as the Discrete Element Method (DEM) and Finite Element Analysis (FEA) allow for the detailed simulation of interactions between regolith particles and materials, considering factors such as particle size, shape, distribution, and mechanical properties to provide a comprehensive understanding of abrasive wear mechanisms (Xi et al., 2021). However, the development, verification, and validation of numerical models require extensive experimental testing to ensure reliable results. Designing and testing machines and tools that operate on the lunar surface with terrestrial equivalents (simulants) is standard practice (Barkó et al., 2023). Lunar simulants were designed to reproduce the composition, mineralogy, morphology, and size distribution of different types of lunar regoliths. According to the literature, most of the time, no thorough characterization is provided with their release, and there are no lunar regolith simulants that can address the wide range of use cases required for exploratory missions (Windisch et al., 2022). The studies were conducted using fine and coarse types of advanced lunar regolith simulants, LX-TH100 and LX-M100, which are appropriate for mechanical studies (Keuntje et al., 2024). Both simulants mimicked the particle morphology and particle size distribution of lunar regolith, as determined from samples from the Apollo and Luna missions (Seidel et al., 2023). Accurate tribological models depend on precise input data, including the size distribution of the abrasive particles. Using simulants with various size fractions allows for more realistic wear rate modelling, particularly under prolonged exposure to lunar dust. Testing materials with distinct size fractions allows researchers to systematically evaluate their durability for space exploration (Trigwell, 2013) and gain insights into specific wear mechanisms (Kawamoto, 2014). Different 3-body abrasive testing mechanisms together with different lunar regolith features from a size distribution standpoint will provide a detailed picture of the abrasive characteristics of lunar soil.

To this end, in this research work, one distinct particle size fraction from previously prepared LX-TH100 lunar simulant was used to determine proper imitation of the lunar environment by Nitrogen gas in a custom-built sand-pot device. Stainless steel rotating shaft and PTFE spring loaded seal pair was tested under a continuous Nitrogen gas flow and under a Nitrogen gas environment prefilled for 5 minutes.

2. Experimental

In this work, Fraction 4 from the previously prepared five fractions of LX-TH100 lunar simulant (Table 1) was used in 3-body abrasive wear testing by sand-pot test device. The LX-TH100 is made of anorthosite rock containing primarily plagioclase (>95%), corresponding to the lunar terrae regions (B. Turapov, 2024).

Table 1. Five different size fractions of LX-TH100 Lunar highland simulant for the 3-body abrasive test (Turapov & Kalácka, 2024).

| Name | Particle size distribution |
|------------|----------------------------|
| Fraction 5 | 1.4 μ m - 2.0 μ m |
| Fraction 4 | 1 μ m - 1.4 μ m |
| Fraction 3 | 710 μ m - 1 μ m |
| Fraction 2 | 125 μ m - 710 μ m |
| Fraction 1 | 0 μ m - 125 μ m |

For the shaft material, 1.4404 (EN) steel grade and for the sealing natural PTFE lip seal was utilized. Three-body abrasive wear testing of the rotating shaft was conducted according to was conducted according to DIN 50322 standard, category VI. For each case rotating shaft/seal mechanism is planned to run for 0.25h, 7h and 24 hours (Figure 1).

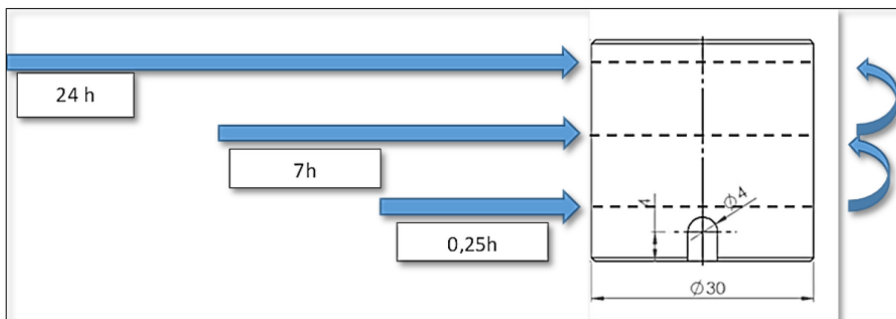


Figure 1. Test run sequences

Before testing, shafts and sealings undergo ultrasonic cleaning in an ultrasonic bath for 20 minutes (Figure 2), followed by 24 hours of drying in a drying cabinet DRY30EA at 22 to 24°C (Figure 3).



Figure 2. Cleaning shafts and seals in an ultrasonic bath.



Figure 3. Drying shafts, seals and Lunar regolith in the drying chamber.

After the cleaning and drying the surface roughness of the shaft samples was measured in accordance with the DIN 4768 standard, and the results are recorded (Figure 4).



Figure 4. Surface roughness test of stainless steel shaft sample

Lunar regolith simulants were also dried in a drying chamber for 24 hours. The inside of the sand pot chamber and the inner surface of the cover plate (top of the sand pot) were cleaned with IPA and laboratory tissue. The installed sand-pot test rig is illustrated in Figure 5.



Figure 5. 3-body abrasive wear testing by sand-pot test rig.

A sample of sealing has been placed into the housing (SKF assembling set) of the chamber cover and the driving shaft unit has been placed into the chamber cover. As soon as the chamber was prepared, it was inserted into the sand pot machine according to the keyway position, the torque head was lowered along the guideway to the chamber contacts, and the connection was tightened with two screws. The shaft was fixed at the dead end, and the chamber unit was lifted to its measurement position. The chamber was prefilled with T5.0 Linde N2 gas supply for 3 minutes with a 50 cm³/min gas mass flow rate. A camera was connected, and the shaft alignment and sealing were checked.

3. Results and discussion.

The results of the surface roughness analysis (Figure 6) will be used for the comparison with the surface evaluation after the test. Additionally the results will be used for the comparison of different particle size fractions abrasive properties.

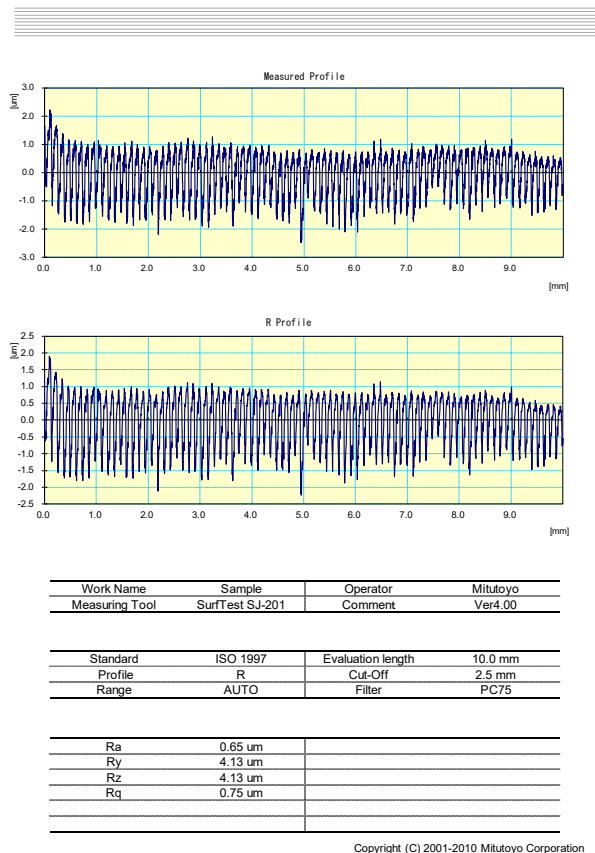


Figure 6. Surface roughness result of Ln-Ss-Lx-TH100-Fr4.

The designation Ln-Ss-Lx-TH100-Fr4 explanation is Ln-Lunar, Ss-Stainless steel (shaft material), Lx-TH100 – Lunar regolith simulant type, Fr4 – fraction 4. This designation system will be used in future research also.

In the system with a PTFE lip seal on a rotating stainless-steel shaft (circumferential $v=0,1$ m/s), the starting torque due to the friction loss was $0,1525$ N*m, steadily running as long as the lip seal reaches 5.74 m. sliding distance. Then, the abrasive regolith particles get into the contact zone of the lip seal causing a frictional increase and instability (Figure 7).

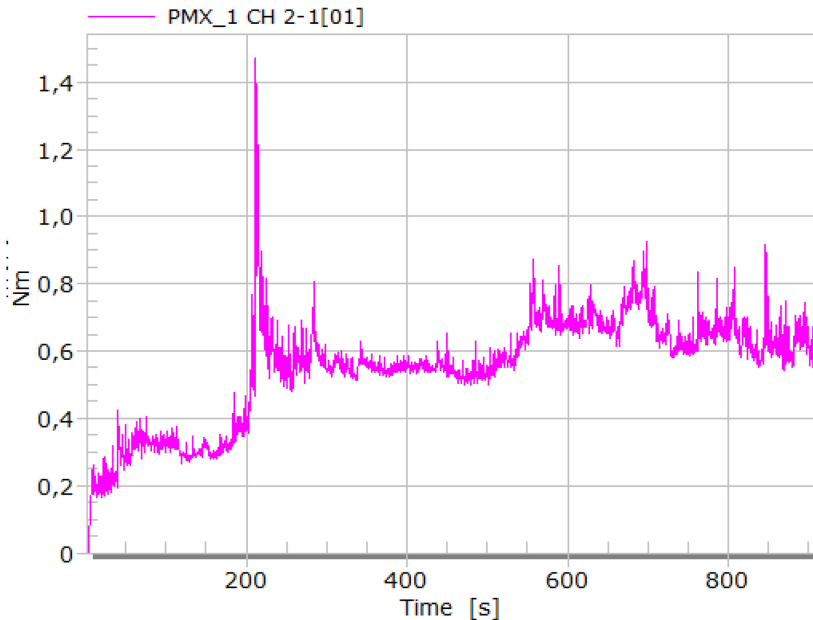


Figure 7. The change of driving torque of the shaft/seal pairs working in the imitated lunar environment.

After 21.2 m. sliding distance, the lip seal was partially damaged, Lunar particles started to come out from the chamber of the sand-pot device with a gradual decrease of torque due to wear out of sealing and reduction of particles in the chamber. After 91 m. sliding distance, the test was stopped with 0.63 Nm torque.

4. Conclusion

The current study practically describes testing a 3-body abrasive wear process between the Lunar regolith with distinct particle size with stainless steel shaft/PTFE seal rotating pair. Starting from the material preparation, the

procedure was established step by step in accordance with safety standards, DIN 4768 and DIN 50322 standards, and the research conducting ethics.

The 3-body abrasive wear test in the sand-pot test device reported the trend lines of the torque changes and running distances due to the abrasive wear nature of Lunar regolith. Based on the research results, bigger particle sizes have higher abrasive properties. Cited five particle size fractions will be used to replicate the lunar environment in experimental analysis for further evaluation. Future studies will assess the wear performance of a polytetrafluoroethylene (PTFE) seal and stainless steel shaft using a specially designed pin-on-disc tribo-test rig and sand-pot test rig.

References

- [1] Afshar-Mohajer, N., Wu, C.-Y., Curtis, J. S., & Gaier, J. R. (2015). Review of dust transport and mitigation technologies in lunar and Martian atmospheres. *Advances in Space Research*, 56(6), 1222–1241. <https://doi.org/10.1016/j.asr.2015.06.007>
- [2] Barkó, G., Kalácska, G., Keresztes, R., Zsidai, L., Shegawu, H., & Kalácska, Á. (2023). Abrasion Evaluation of Moon and Mars Simulants on Rotating Shaft/Sealing Materials: Simulants and Structural Materials Review and Selection. In *Lubricants* (Vol. 11, Issue 8). Multidisciplinary Digital Publishing Institute (MDPI). <https://doi.org/10.3390/lubricants11080334>
- [3] Gaier, J., & Berkebile, S. (2012, January 9). Implication of Adhesion Studies for Dust Mitigation on Thermal Control Surfaces. 50th AIAA Aerospace Sciences Meeting Including the New Horizons Forum and Aerospace Exposition. <https://doi.org/10.2514/6.2012-875>
- [4] Kawamoto, H. (2014, January 13). Electrostatic Particle-Size Classification of Lunar Regolith for In-Situ Resource Utilization. 7th Symposium on Space Resource Utilization. <https://doi.org/10.2514/6.2014-0341>
- [5] Keuntje, J., Griemsmann, T., Patzwald, J., Staehr, R., Jaeschke, P., Stoll, E., Kaierle, S., & Overmeyer, L. (2024). Numerical simulation approach for Laser Melting of lunar regolith using an enthalpy-based model. *Procedia CIRP*, 124, 347–351. <https://doi.org/10.1016/j.procir.2024.08.131>
- [6] Li, R., Cui, Y., Feng, Y., Wang, J., Huang, W., Sui, Y., & Ren, D. (2023). New Mechanical Models to Study the Impact of Contact, Wear, and Adhesion of Lunar Dust on Space Materials. *International Journal of Applied Mechanics*, 15(04). <https://doi.org/10.1142/S1758825123500254>
- [7] Mukhtar, S. H., Wani, M. F., Sehgal, R., & Sharma, M. D. (2023). Nano-mechanical and nano-tribological characterisation of self-lubricating MoS₂ nano-structured coating for space applications. In *Tribology International* (Vol. 178). Elsevier Ltd. <https://doi.org/10.1016/j.triboint.2022.108017>

- [8] Nikki Welch. (2021, June 8). Dust: An Out-of-This World Problem. <https://www.nasa.gov/humans-in-space/dust-an-out-of-this-world-problem/>
- [9] Seidel, A., Teicher, U., Ihlenfeldt, S., Sauer, K., Morczinek, F., Dix, M., Niebergall, R., Durschang, B., & Linke, S. (2023). Towards Lunar In-Situ Resource Utilization Based Subtractive Manufacturing. *Applied Sciences*, 14(1), 18. <https://doi.org/10.3390/app14010018>
- [10] Trigwell, S. et al. (2013). Electrostatic beneficiation of lunar regolith: Applications in in situ resource utilization. *Journal of Aerospace Engineering*, 26(1), 30–36.
- [11] Turapov, B., & Kalácka, G. (2024). Book of Abstracts from the 10th International Scientific Conference on Advances in Mechanical Engineering (ISCAME 2024) (Vol. 8). Trans Tech Publications Ltd. <https://doi.org/10.4028/b-gZHse4>
- [12] Valerie Wiesner. (2024). Dust-Proofing the Future: Materials Challenges for Lunar Exploration.
- [13] Windisch, L., Linke, S., Jütte, M., Baasch, J., Kwade, A., Stoll, E., & Schilde, C. (2022). Geotechnical and Shear Behavior of Novel Lunar Regolith Simulants TUBS-M, TUBS-T, and TUBS-I. *Materials*, 15(23). <https://doi.org/10.3390/ma15238561>
- [14] Xi, B., Jiang, M., & Cui, L. (2021). 3D DEM analysis of soil excavation test on lunar regolith simulant. *Granular Matter*, 23(1), 1. <https://doi.org/10.1007/s10035-020-01070-6>
- [15] Zanon, P., Dunn, M., & Brooks, G. (2023). Current Lunar dust mitigation techniques and future directions. *Acta Astronautica*, 213, 627–644. <https://doi.org/10.1016/j.actaastro.2023.09.031>.

Energetic analysis and mathematical modelling of a solar-pot

Márton RÁTKAI¹, Gábor GÉCZI², Richárd KICSINY³, László SZÉKELY³

¹*Doctoral School of Mechanical Engineering,*

Hungarian University of Agriculture and Life sciences, MATE, Gödöllő

²*Department of Environmental Analysis and Technologies, Institute of Environmental Sciences, MATE Gödöllő*

³*Department of Mathematics and Modelling, Institute of Mathematics and Basic Science, MATE Gödöllő*

Abstract

The studied solar-pot is a recent invention, which is made for environmentally friendly cooking or heating (by utilizing solar energy) of foods and liquids. Its structure is similar to a double pipe heat exchanger, it has an outer mantle and an inner cooking tank. The goals of the paper are presenting a recent physically-based mathematical model describing the solar pot and carrying out computer experiments with it, assembling an experimental system of the pot connected with a solar collector and performing measurements on it. Based on the results, the solar pot can successfully be used for cooking or sterilizing foods or liquids during the studied time period, in Hungary. In particular, based on measured data, the temperature level needed for heat treatment (75 °C) can be maintained in the cooking tank for several hours (~5 h, on the average) in a typical day in May.

Keywords

solar-pot, solar cooking, measurements, mathematical modelling, simulation results

1. Introduction

The thermal energy provided by the sun is used to treat food in different ways. Examples include drying (Kalita et al., 2024), baking and cooking (Mehling 2023). Solar food preparation devices operated with solar energy are known, in which solar energy directly heats a surface or air along it in a closed box, and the heat is transferred from there to the closed vessel placed in the box (Saxena et al., 2020). With this solution, the preparation of food by cooking cannot be solved in many cases (Bigelow et al., 2024). However, there are solar cookers able to produce the temperature required for cooking, which is 73.9 °C according to USDA (2025). Typical types are the reflective panel (Gupta et al.,

2021), the parabolic (Saini et al., 2023) and the evacuated tube solar cooker (Hosseinzadeh et al. 2020). These are the so-called direct-type food processing devices. Indirect types use a solar collector to produce the thermal energy needed for food processing.

In Zhou et al. (2023), a solar cooker with solar collector and heat storage is investigated in China. The main goal of the research was to investigate the effect of the quartzite heat storage medium on the system. For this, a mathematical model describing the performance of the system was prepared. Based on the results, the version with quartzite heat storage increases the performance of the system, and the investment cost also decreases. The solar share was 71% which clearly means a significant reduction in the carbon dioxide emission with regard to the cooking activity. In the investigations of the present paper on a mantle-pot equipment that we call solar pot, working with only solar heat, the solar share is even higher, 100%. Nevertheless, the completion of the pot with some auxiliary heating may come into consideration in the future, as it is mentioned in the Conclusions. (It would decrease the solar share but increase the operating period of the pot.)

In Hosseinzadeh et al. (2021), a research is conducted on an indirect type solar food processing device with nanofluid working medium. One of the main elements of the system is the parabolic solar collector, at the focal point of which the working medium is heated by flowing through it. The other important element is the cooking unit, which consists of a copper pot and the copper pipe that surrounds it (wrapped around it). The heated working medium flows in this pipe, thus transferring the heat to the cooking space. A separate tank was also installed between the cooking unit and the collector. Due to the parabolic collector, the spiral heat exchanger and the additional tank, the structure of the system is more complex and thus its implementation is obviously more expensive than the system of the solar pot of this paper, which uses a more conventional evacuated tube collector and the solar pot similar to a simple, jacketed heat exchanger.

In Getnet et al. (2023), it was investigated how the performance of the system changes when the collector is supplemented with reflectors in an indirect solar food processing system equipped with a flat plate collector. They found that without a reflector the highest temperature of the outlet working medium is 71 °C, and the highest energy efficiency is 63%. It can be stated that the system is not suitable for cooking as the minimum safe temperature for cooking is 73.9 °C according to USDA (2025). On the other hand, thanks to the addition of reflectors, these values were respectively 103.65 °C and 79%. It should be mentioned that the additions made in order to increase the performance of the equipment significantly increased the complexity of the system. The system examined in this paper has a simpler design and does not contain phase change material.

The main elements of the system examined in this paper are the solar collector and the so-called solar pot. In the literature, there are mathematical

models for collectors and solar heating systems (Buzás and Farkas 2000, Castellanos et al. 2020), however, as it is a recent invention, no model has yet been worked out for the solar pot. In terms of design, the solar pot is similar to a tube-in-tube heat exchanger or a solar storage tank. Models for those are already available in the literature. There are two main types of models. One is the black-box type and the other one is the physically-based model. The physically-based model relies on the physical background of the modelled system or process, which is therefore often difficult to set up in the case of a complex system (Kalogirou et al., 1999). Black-box modelling does not take into account the physical background, it represents a more result-oriented approach, the creation of the model is typically simpler (Brus and Zambrano 2010, Zheng et al. 2023).

The Hottel-Whillier-Bliss physically-based mathematical model worked out for flat plate collectors (Hottel and Woertz 1942) can be used to describe the temperature distribution of the working medium along the length of the collector as a function of place and time. The model was also extended to evacuated-tube collectors (Rátkai et al. 2024a). In Buzás et al. (1998), a physically-based mathematical model was developed that can be used to describe the temporal behaviour of a flat plate collector. Estimation of the temperature of the outlet working medium is made possible by a differential equation formulated on the basis of the energy balance of the collector. In Víg (2007), a black-box type neural network model was made, which can be used to model the thermal behaviour of a flat plate collector. Knowing the intensity of solar radiation, the ambient temperature and the temperature of the working medium entering the collector, with a constant mass flow, the temperature of the outlet heat transfer medium can be predicted with the model. In Kicsiny (2014), a black-box model based on multiple linear regression was developed for solar collectors. As a result, the appropriate temperature of the outlet working medium can be calculated. The identified and validated model was compared to the physically-based model of Buzás et al. (1998). The results showed that the model in Kicsiny (2014) was able to predict the temperature of the outlet working medium more accurately. The importance of the model, in addition to the appropriate accuracy (average accuracy better than 5%), is due to its simplicity. It requires little calculation and can be used for any type of collector (e.g., evacuated tube collector).

There are several mixed storage models in the literature. In Buzás and Farkas (2000), a physically-based mathematical model was developed. An ordinary differential equation based on the energy balance of the tank allows the temperature of the tank to be calculated. The model does not take into account the heat capacity of the solar storage material. In Hiris (2022), a physically-based mathematical model for a mixed storage was worked out, based on the heat balance of the storage, which can be used to calculate the temperature of the storage. A similar model can be found in Badescu (2008). In Kicsiny (2018), a black-box model based on multiple linear regression was developed for mixed

solar storages, which can be used to determine the geometric average temperature of the storage.

When modelling tube-in-tube heat exchangers, energy balance is often assumed between the working media of the two sides, neglecting the environmental heat exchange (Bradley 2010, Zohuri 2017). In Géczi et al. (2019), various mathematical models for tube-in-tube heat exchangers similar to the solar pot examined in this paper were developed. The physically-based model takes into account the heat exchange with the environment, too. A black-box type mathematical model was also developed in Géczi et al. (2019) based on multiple linear regression, which also takes environmental heat exchange into account. The models were validated using measurements on a heat exchanger. Based on the results, the physically-based model not neglecting the heat exchange with the environment can estimate the temperature of the outlet working medium more accurately than the other model version assuming energy balance between the two sides of a heat exchanger. The black-box model proved to be more accurate than both models, in case of considerable environmental heat exchange.

The content of the present paper, with recent results (Rátkai et al. 2024c) and new measured data, is as follows:

1. A recent physically-based mathematical model is presented to describe the examined, recently invented solar pot. Computer simulations are made with the model, based on which conclusions are drawn regarding the practical applicability of the solar pot.
2. An experimental system of the hydraulically connected solar pot and a solar collector is physically assembled. The different variables of the system (different temperature values) are measured. Based on measured data, conclusions are drawn regarding the practical applicability of the solar pot.
3. New measurements made in a longer period between 16 May and 03 June 2024 underlie the applicability of the solar pot (see Figure 16.)

The structure of the paper is the following: Section 2 contains the description of the modelled and measured system. Section 3 presents the physically-based model of the solar pot along with the simulation results. In Section 4, the measurements made on the experimental system and the measured data are shown. Section 5 serves with conclusions and future research proposals.

2. System description

The solar pot (shown in Figure 1) is a recent invention, which gained a utility model protection in 2021 from the Hungarian Intellectual Property Office under patent number 5489 (Géczi and Kicsiny 2021). Currently, the pot is in prototype

status, that is, a single specimen of it has been produced, from stainless steel (AISI 304) with a thickness of 2 mm, so far, for research purposes. However, it is already published by means of the mentioned patent, so it could be produced by a proper manufacturer commercially, in compliance with the related legal regulations.

The device is made for environmentally friendly cooking or heating of foods and liquids. Its structure is similar to a double pipe heat exchanger. It has an outer mantle and an inner cooking tank. Cooking or heating is done as follows. The mantle heats the cooking tank by circulating working medium (water or else) along the cooking tank's outer surface. The mantle forms a closed hydraulic circuit with a solar collector. The working medium in the mantle and the interior of the cooking tank are hydraulically separated from each other, which implies heating and cooking can be executed hygienically. The pot can also be used for reheating foods or heating liquids not only in connection with food preparation. Using the device, heating and cooking can be made with the utilization of renewable solar energy. The solar pot has the advantage that it can be connected to an existing solar heating system (Rátkai et al., 2024b). It is an indirect-type food processing equipment, which can be used with any collector using liquid as working fluid. If there is insufficient solar energy, one can heat the pot with a stove or a cooking plate as well.



Figure 1. Photos of the solar-pot (Rátkai et al. 2024c).

In the experimental system of this paper, the solar pot is connected to an evacuated tube solar collector. Figure 2 presents the sketch of the pot containing the main geometric sizes and measuring points (for three temperatures) on it.

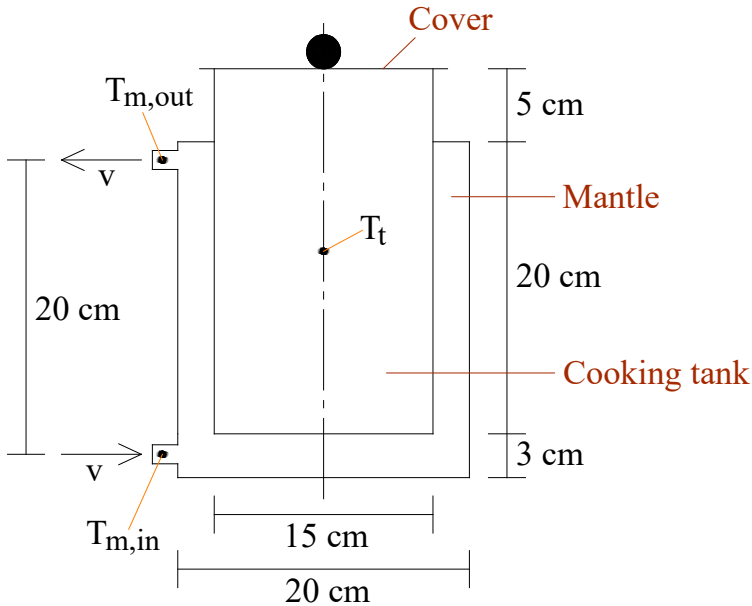


Figure 2. Sizes and measuring points of the solar-pot (Rátkai et al. 2024c).

The experimental solar heating system with the solar pot and the time-dependent variables along with the parameters of the system are shown in Figure 3.

In Figure 3, t denotes the time dependence of the variables. These variables are the following:

- $T_{c,e}$: temperature of the solar collectors's environment (outdoors), °C,
- $T_{c,in}$: solar collector inlet (water) temperature, °C,
- $T_{c,out}$: solar collector outlet (water) temperature, °C,
- T_t : temperature in the cooking tank, °C,
- $T_{p,e}$: temperature of the solar pot's environment (indoors), °C,
- $T_{m,in}$: mantle inlet (water) temperature, °C,
- $T_{m,out}$: mantle outlet (water) temperature, °C.

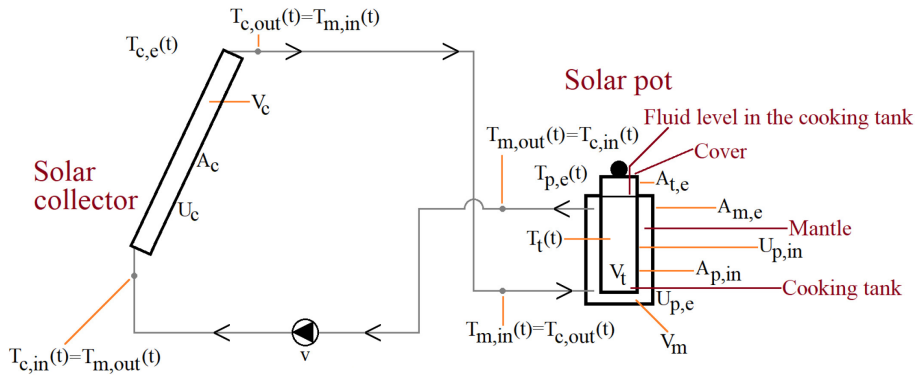


Figure 3. The solar pot and the experimental system (Rátkai et al. 2024c).

As the fluid in the mantle is considered mixed, the (homogeneous) temperature inside the mantle is (consequently) considered the same as the mantle outlet temperature. (Basically, this temperature also corresponds to the, geometrically, mean fluid temperature in the mantle.) As the pipes connecting the solar pot and the collector are insulated and their volume is neglected, we consider the solar collector outlet temperature and the mantle inlet temperature equal ($T_{c,out} = T_{m,in}$). The same holds for the solar collector inlet temperature and the mantle outlet temperature ($T_{c,in} = T_{m,out}$).

The constant parameters of the system are the following:

- A_c : surface area of the collector (one side), m^2 ,
- $A_{m,e}$: surface area of the mantle to the environment, m^2 ,
- $A_{t,e}$: surface area of the cooking tank to the environment, m^2 ,
- $A_{p,in}$: surface area between the mantle and the cooking tank, m^2 ,
- U_c : overall heat loss coefficient of the solar collector, $\frac{W}{m^2K}$,
- $U_{p,e}$: overall heat loss coefficient of the solar pot, $\frac{W}{m^2K}$,
- $U_{p,in}$: overall heat transfer coefficient between the mantle and the cooking tank, $\frac{W}{m^2K}$,
- v : volumetric flow rate of the pump, $\frac{m^3}{s}$,
- V_c : volume of the collector, m^3 ,
- V_m : volume of the mantle, m^3 ,
- V_t : volume of the cooking tank, m^3 .
-

During the tests, the cooking tank is filled with water up to the top of the mantle

and covered by a stainless steel plate. The stainless steel cover can be removed during the cooking process to check the state of the handled food or drink. Accordingly, there is atmospheric pressure inside the cooking tank. We also circulate water between the solar pot and the solar collector as the working fluid (Rátkai et al., 2024c).

3. Mathematical modelling

The model of the solar pot is a physically-based mathematical model based on the energy balance of the pot. It consists of two submodels (due to the jacketed structure of the pot), one for the mantle temperature and the other for the cooking tank temperature, constituting a system of differential equations. Both equations are non-homogeneous linear differential equations with constant coefficients. The model uses temperature differences only, which allows the use of either Celsius or Kelvin values.

3.1. Mathematical Model

Equations (1, 2) represent the model of the solar pot. Equation (1) is for the mantle, while Equation (2) is for the cooking tank temperature:

$$\frac{dT_{m,out}}{dt} = \frac{v}{V_m} (T_{m,in} - T_{m,out}) + \frac{A_{m,e}U_{p,e}}{\rho c V_m} (T_{p,e} - T_{m,out}) + \frac{A_{p,in}U_{p,in}}{\rho c V_m} (T_t - T_{m,out}), \quad (1)$$

$$\frac{dT_t}{dt} = \frac{A_{p,in}U_{p,in}}{\rho c V_t} (T_{m,out} - T_t) + \frac{A_{t,e}U_{p,e}}{\rho c V_t} (T_{p,e} - T_t),$$

where the density of water is ρ and the specific heat capacity is c .

3.2. Simulation Results

Equations (1, 2) were fed into the Matlab/Simulink programming environment. The computer realization of the model can be seen in Figure 4.

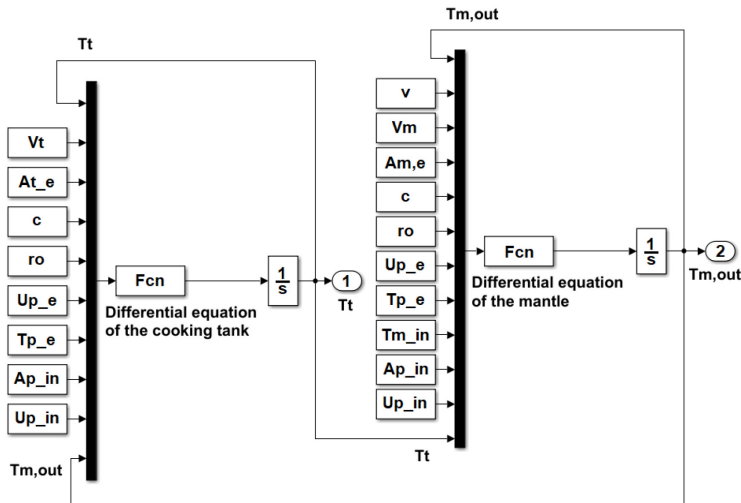


Figure 4. Computer realization of the mathematical model (Rátkai et al. 2024c).

To run the model, the values of the solar pot's parameters need to be provided. $A_{m,e} = 0.19 \text{ m}^2$, $A_{t,e} = 0.041 \text{ m}^2$, $A_{p,in} = 0.112 \text{ m}^2$, $V_m = 3.691 \text{ l} (= 3.691 \cdot 10^{-3} \text{ m}^3)$, and $V_t = 4.418 \text{ l} (= 4.418 \cdot 10^{-3} \text{ m}^3)$ are geometric parameters of the physically manufactured solar pot (see Figure 1 in Section 2). The density (ρ) and specific heat capacity (c) of water are also needed. These values are $1000 \frac{\text{kg}}{\text{m}^3}$ and $4200 \frac{\text{J}}{\text{kgK}}$, respectively.

The determinations of $U_{p,e} = 20.4 \frac{\text{W}}{\text{m}^2\text{K}}$ (overall heat loss coefficient) and $U_{p,in} = 351 \frac{\text{W}}{\text{m}^2\text{K}}$ (overall heat transfer coefficient) are made by calculations based on recommendations from the literature.

$U_{p,e}$ is the overall heat loss coefficient between the mantle and the solar pot's environment. It is determined by considering the following:

1. Convective heat transfer between the inside of the mantle and the inner surface of the mantle's wall. (This wall is adjacent to the environment.) Taking into account the liquid in the mantle (water) and the material of the mantle's wall (stainless steel), and assuming forced convective heat transfer along the inner surface of the mantle's wall, the heat transfer coefficient is $850 \frac{\text{W}}{\text{m}^2\text{K}}$, which is an average value according to Cao (2010).
2. Thermal conduction inside the mantle's wall. Taking into account the material of the mantle's wall, which is stainless steel (with a thickness of 0.002 m), the thermal conductivity coefficient is $15 \frac{\text{W}}{\text{mK}}$, which is an average value according to Cao (2010).

3. Convective heat transfer between the outer surface of the mantle's wall and the solar pot's environment. Taking into account the material of the mantle's wall (stainless steel) and the air surrounding the pot from outside, and assuming free convective heat transfer along the surface of the wall, the heat transfer coefficient is $21 \frac{W}{m^2K}$, which is an average value according to Cao (2010).

The above details were fed into the Engineering Toolbox (2025) online program, which made the necessary calculations for the overall heat loss coefficient. The result is $U_{p,e} = 20.4 \frac{W}{m^2K}$.

In the value of $A_{t,e}$ (which is the responsible surface regarding the heat loss of the cooking tank to the environment), the surface area of both the cover and that part of the tank's wall which is above the mantle are included. Furthermore, $U_{p,e}$ is applied to this surface when determining the heat loss of the cooking tank to the environment. Of course, this approach contains certain simplifications (which is clearly advantageous when one would like to apply the model in the practice) since it does not take into account that there is some air between the tank's fluid and the cover. Nevertheless, it must underestimate the pot's real heat performance a bit since the air has some (advantageous) thermal insulating effect. It also means that we do not provide even a slight advantage for the solar pot when presenting its potential applicability. In addition, we carried out simulations (not detailed here) where we tried to model the special effect of the air under the cover. In fact, the difference was so slight (within 1% regarding the modelled temperature values) that we think they are not worth dealing with in the present model.

$U_{p,in}$ is the overall heat transfer coefficient between the mantle and the cooking tank. It is determined by considering the following:

1. Convective heat transfer between the inside of the mantle and the outer surface of the cooking tank's wall. Taking into account the liquid in the mantle (water) and the material of the cooking tank wall (stainless steel), and assuming forced convective heat transfer along the surface of the wall, the heat transfer coefficient is $850 \frac{W}{m^2K}$, which is an average value according to Cao (2010).
2. Thermal conduction inside the mantle's wall. (For more details, see Note 2 above.)
3. Convective heat transfer between the inner surface of the cooking tank's wall and the inside of the cooking tank. Taking into account the material of the wall (stainless steel) and the liquid in the cooking tank (water), and assuming free convective heat transfer along the surface of the wall, the heat transfer coefficient is $650 \frac{W}{m^2K}$, which is an average value according to Cao (2010).

The above details were fed into the Engineering Toolbox (2025) online program, which made the necessary calculations for the overall heat transfer coefficient. The result is $U_{p,in} = 351 \frac{W}{m^2K}$.

$T_{p,e}(t)$ is assumed to be constant as the solar pot is located in an air-conditioned mobile container, so $T_{p,e} := T_{p,e}(t) := 25^\circ\text{C}$, in accordance with the temperature set inside the container. The initial values of the model are also set to this value, so $T_{m,out}(0) := 25^\circ\text{C}$ and $T_t(0) := 25^\circ\text{C}$. (Accordingly, our model can be applied for a solar pot inside a building, which is a rather general situation, since the outside effects, like the effect of sky, solar irradiance, wind speed etc. are not considered.) For the sake of simplicity, $T_{m,in}(t) (= T_{c,out}(t))$ is set constant in the simulations, 80°C . Choosing this temperature value, it was taken into consideration that it can easily be reached and maintained for a longer time on a typical day in May in Hungary (see e.g., Figure 9 in Section 4.2), and that this inlet temperature is probably high enough for the cooking tank to reach the minimum temperature for sterilizing foods—based on our preliminary assumption. This minimum temperature is 73.9°C , but in this work 75°C is aimed due to safety purposes. The simulations were carried out with two different volumetric flow rate (v) values, which can be realized in the experimental system as well. The results of the simulations are presented in Figures 5 and 6. More specifically, Figure 5 presents the modelled $T_{m,out}$ and T_t temperatures in case of $v = 100 \frac{1}{h} (= 2.78 \cdot 10^{-5} \frac{m^3}{s})$, while Figure 6 presents them in case of $v = 200 \frac{1}{h} (= 5.56 \cdot 10^{-5} \frac{m^3}{s})$. The running time of the simulations was 1 h in both cases.

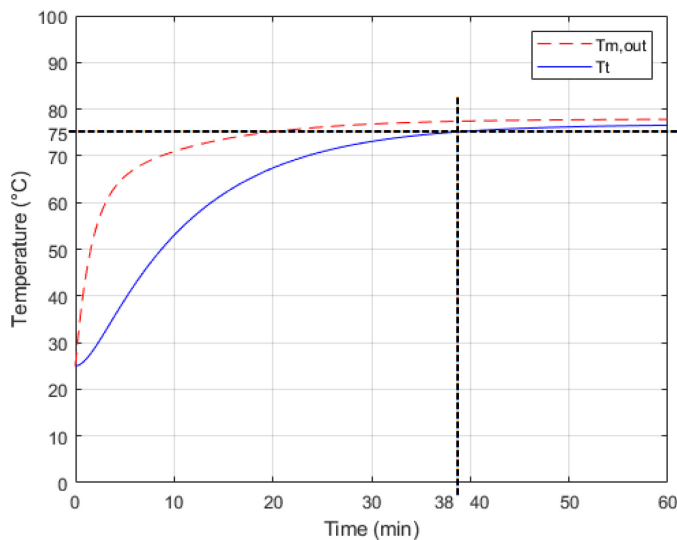


Figure 5. Result of the simulation in case of $v = 100 \frac{1}{h}$ (Rátkai et al. 2024c).

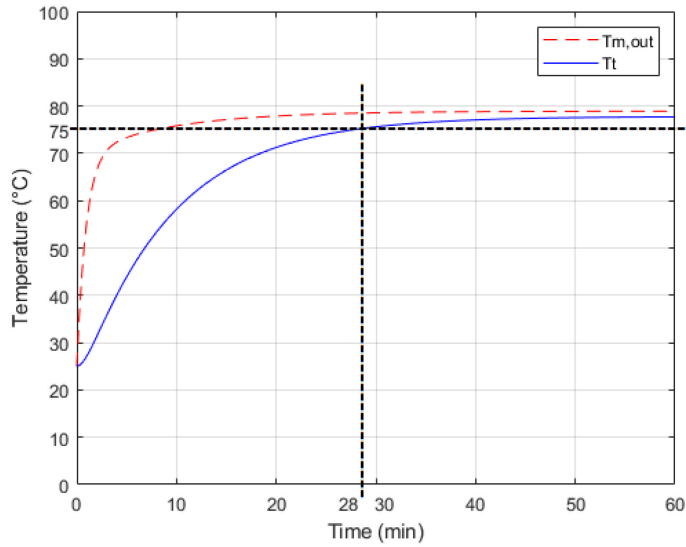


Figure 6. Result of the simulation in case of $v = 200 \frac{1}{h}$ (Rátkai et al. 2024c).

In Figures 5 and 6, it can be seen that the cooking tank temperature reaches 75 °C, which is normally enough for the sterilization of foods. It can also be stated that this temperature is reached in less time with higher flow rate. With $100 \frac{1}{h}$, it took 38 min (see Figure 5), while with $200 \frac{1}{h}$, it required 28 min (see Figure 6). In addition, the maximum (final) tank temperature was 76.5 °C in case of $100 \frac{1}{h}$ and 77.7 °C with $200 \frac{1}{h}$.

4. Experimentation

4.1. Experimental System

During the measurements, the values of $T_{c,e}$, $T_{m,in}$ ($= T_{c,out}$), $T_{m,out}$ ($= T_{c,in}$), $T_{p,e}$, T_t and v are measured. The temperatures are measured with K-type thermocouples (with an average uncertainty of 1 °C), the pump flow rate is measured with a Kobold Unirota URM-33 33H G5 (Nyíregyháza, Hungary) 0 type flow meter (with an average uncertainty of $6 \frac{1}{h}$). As additional information, the (global) solar irradiance on the collector's plane is also measured (in $\frac{W}{m^2}$). The type of the solar irradiance sensor is Theodor Friedrichs 6003.3000 BG (Elmshorn, Germany) (with an average uncertainty of $30 \frac{W}{m^2}$). The collector, with $2.2m^2$, is oriented to the south, its tilt angle is 40°.

The pipes connecting the solar pot and the collector are insulated and their volume is neglected. As a result, we consider the mantle inlet water temperature and the solar collector outlet water temperature equal ($T_{m,in} = T_{c,out}$). The same goes for the mantle outlet water temperature and the solar collector inlet water temperature ($T_{m,out} = T_{c,in}$). The structure of the experimental system, installed at the campus of the Hungarian University of Agriculture and Life Sciences (Gödöllő, Hungary), is shown in Figure 3, the physically manufactured solar pot is presented in Figure 1 and the connected evacuated tube solar collector can be seen in Figure 7.



Figure 7. Photo of the solar collector (Székely et al. 2021).

4.2. Experimental Results

During the measurements, the same flow rates were used as in the simulations. The temperature of the solar pot's environment ($T_{p,e}$) was also constant 25°C as the temperature of the mobile container where the solar pot is located was set to this value with an air-conditioner. Figures 8, 9, 10, 11, 12, 13, 14 and 15 present the graphs of all measurement results. Figures 9 and 11 show the measurement results of two days (26 May 2024 and 28 May 2024) when the flow rate was set

to 100 l/h. In Figure 13 and Figure 15, the measured data of two days (29 May 2024 and 30 May 2024) are presented when the flow rate was set to 200 l/h. On the left side of the figures (a), the graphs of $T_{m,in}$ ($= T_{c,out}$) and $T_{c,e}$ can be seen, on the right (b), there are the graphs of $T_{m,out}$ and T_t . As additional information, Figures 8, 10, 12 and 14 show the solar irradiance on the four measured days.

Figures 9, 11, 13 and 15 demonstrate that the cooking tank temperature reached the safe cooking temperature of 75 °C during the measurements in the early afternoon, between 12:00 and 13:00. The temperature of the cooking tank was higher than this value until late afternoon, between 17:20 and 18:00. The only exception was on 30 May when the tank temperature decreased below 75 °C at 16:18 due to the cloudier weather than usual. According to the measurements, it can be stated that the volumetric flow rate has no considerable influence on the heating. Both examined flow rate values made the safe cooking possible for a satisfactory time interval within each measured day. The measured values of $T_{m,out}$ and T_t are almost equal, which is in accordance with the final modelled temperature values in the simulations (see Figures 5 and 6). Additionally, Figure 16 shows measured $T_{m,out}$ and T_t values in a longer period between 16 May and 03 June 2024.

In summary, the measured results reinforce the simulated ones, which underlie that the solar pot is really able to cook (sterilize) safely (liquid) foods and drinks.

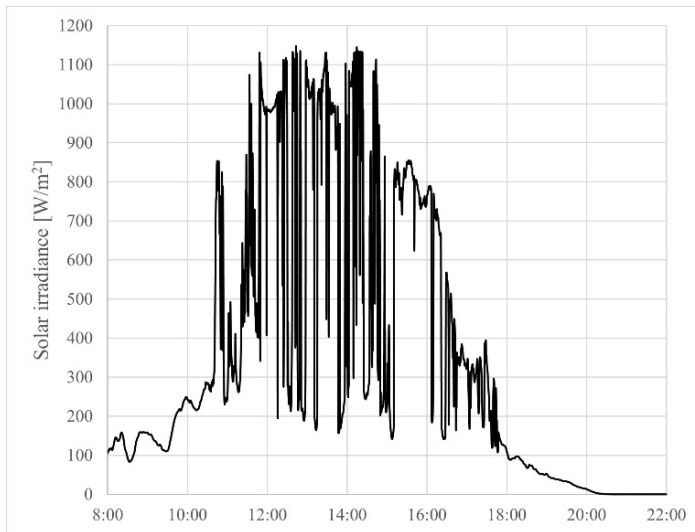
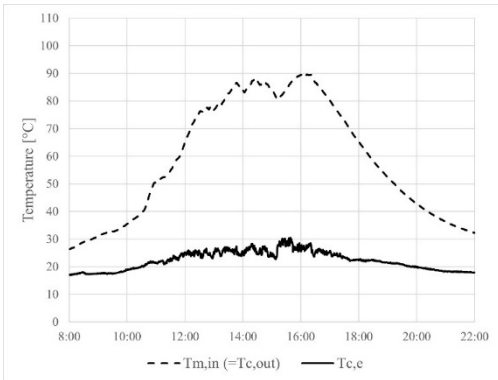
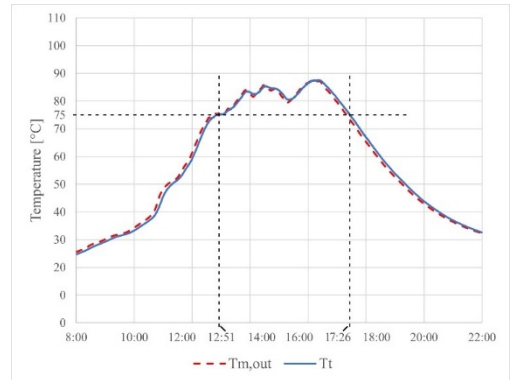


Figure 8. Measured values of the solar irradiance on 26 May 2024, between 8:00 and 22:00 (Rátkai et al. 2024c).



(a)



(b)

Figure 9. Measured values of $T_{c,e}$, $T_{m,in}$ ($= T_{c,out}$) on the left (a) and $T_{m,out}$, T_t on the right (b) on 26 May 2024, between 8:00 and 22:00, when $v = 100 \frac{m}{h}$ (Rátkai et al. 2024c).

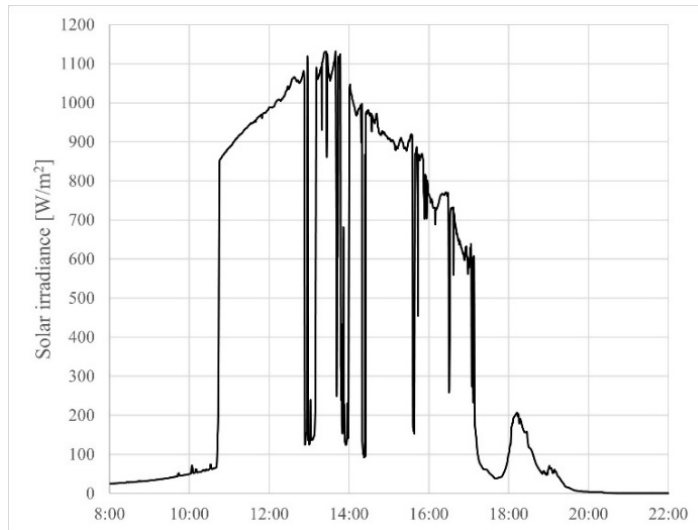


Figure 10. Measured values of the solar irradiance on 28 May 2024, between 8:00 and 22:00 (Rátkai et al. 2024c).

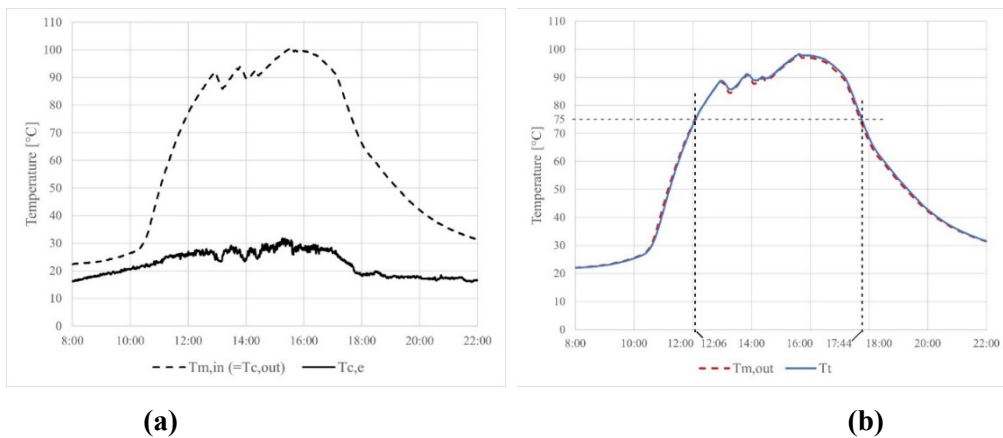


Figure 11. Measured values of $T_{c,e}$, $T_{m,in}$ ($= T_{c,out}$) on the left (a) and $T_{m,out}$, T_t on the right (b) on 28 May 2024, between 8:00 and 22:00, when $v = 100 \frac{m}{h}$ (Rátkai et al. 2024c).

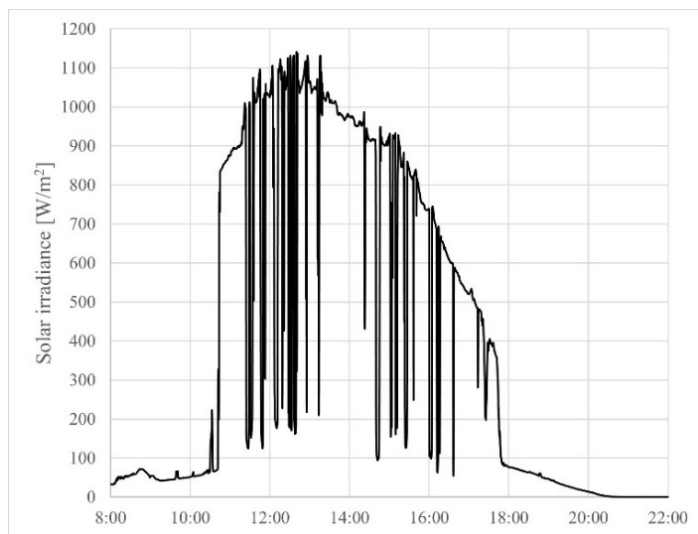


Figure 12. Measured values of the solar irradiance on 29 May 2024, between 8:00 and 22:00 (Rátkai et al. 2024c).

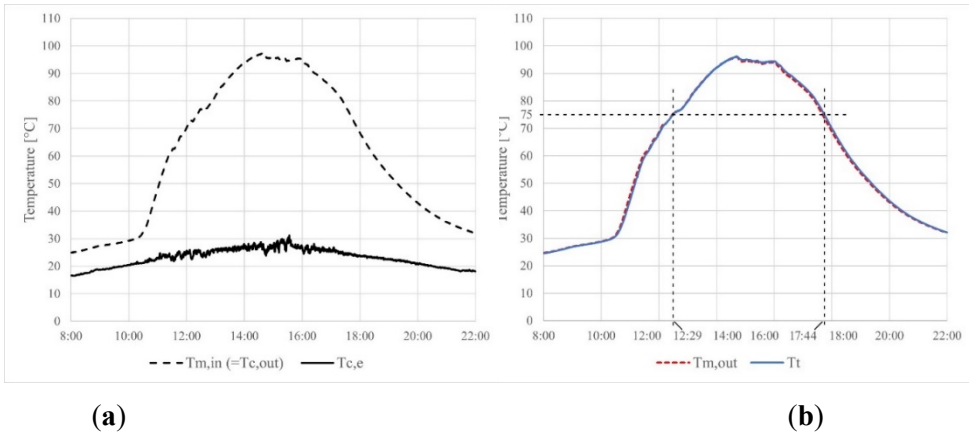


Figure 13. Measured values of $T_{c,e}$, $T_{m,in} (= T_{c,out})$ on the left (a) and $T_{m,out}$, T_t on the right (b) on 29 May 2024, between 8:00 and 22:00, when $v = 200 \frac{m}{h}$ (Rátkai et al. 2024c).

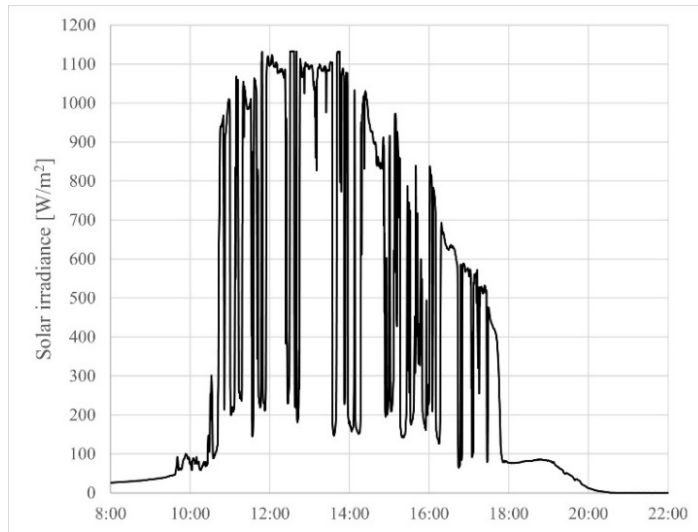


Figure 14. Measured values of the solar irradiance on 30 May 2024, between 8:00 and 22:00 (Rátkai et al. 2024c).

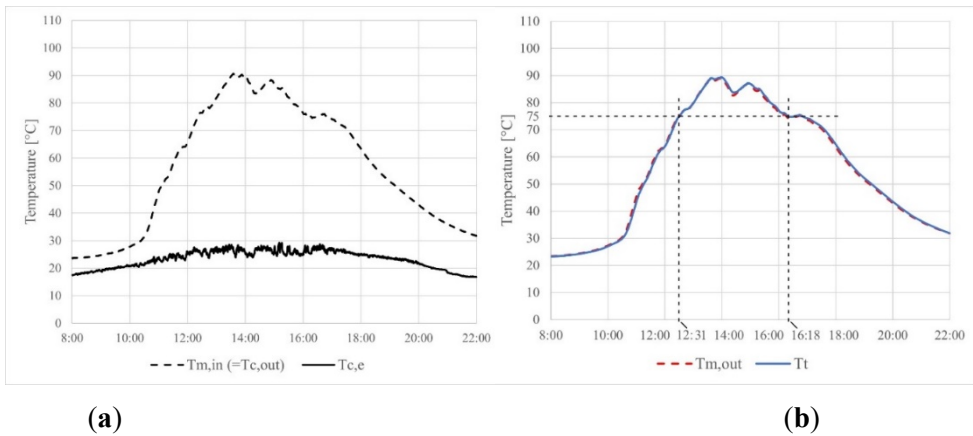


Figure 15. Measured values of $T_{c,e}$, $T_{m,in}$ ($= T_{c,out}$) on the left (a) and $T_{m,out}$, T_t on the right (b) on 30 May 2024, between 8:00 and 22:00, when $v = 200 \frac{h}{h}$ (Rátkai et al. 2024c).

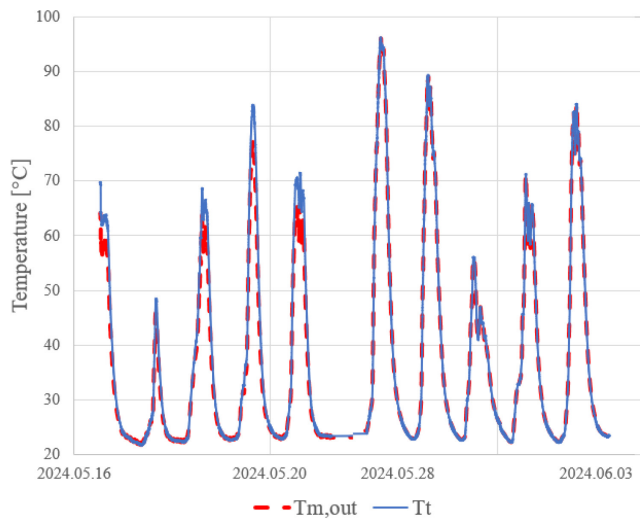


Figure 16. Measured $T_{m,out}$ and T_t values between 16 May and 03 June 2024

5. Conclusions

In the paper, a recent physically-based mathematical model was presented and an experimental system was assembled for a recently invented solar pot. The solar pot, as an environmentally friendly technical tool, utilizes renewable solar heat, provided by a solar collector as the heat source, for cooking or heating foods, drinks or other liquids. Based on both the simulated and the measured

results, the solar pot, containing an inner cooking tank (where the cooking or heating task is realized) and an outer mantle (connected directly to the solar collector), can be used successfully to cook or sterilize different dishes and liquids. In particular, based on measured data, the temperature level needed for heat treatment (75 °C) can be maintained in the cooking tank for several hours (~5 h, on the average) in a typical day in May in Hungary.

Future research plans include the investigation of how long does it take for the solar pot-collector system to cook different dishes (like pasta, meat etc.) in different seasons and weather conditions. The possibility and relevance of different types of auxiliary (not solar) heating solutions (in addition to the solar collector) may also be examined, in order to extend the operating period of the solar pot. With respect to the presented mathematical model, the establishment of a maximally precise version of it (considering sky effects, the effect of air under the cover, the temperature dependence of certain parameters, like the mass density and the specific heat capacity of water, etc.) may come into question in the future.

Acknowledgements

This research was funded by the project ‘The feasibility of the circular economy during national defense activities’ of 2021 Thematic Excellence Programme of the National Research, Development and Innovation Office under grant no.: TKP2021-NVA-22, led by the Centre for Circular Economy Analysis.

References

- [1] Badescu, V. Optimal control of flow in solar collector systems with fully mixed water storage tanks. *Energy Convers. Manag.* 2008, 49, 169–184. <https://doi.org/10.1016/j.enconman.2007.06.022>.
- [2] Bigelow, A.W.; Tabatchnick, J.; Hughes, C. Testing Solar Cookers for Cooking Efficiency. *Sol. Energy Adv.* 2024, 4, 100053. <https://doi.org/10.1016/j.seja.2024.100053>.
- [3] Bradley, J. Counterflow, crossflow and cocurrent flow heat transfer in heat exchangers: Analytical solution based on transfer units. *Heat Mass Transf.* 2010, 46, 381–394. <https://doi.org/10.1007/s00231-010-0579-5>.
- [4] Brus, L.; Zambrano, D. Black-box identification of solar collector dynamics with variant time delay. *Control. Eng. Pr.* 2010, 18, 1133–1146. <https://doi.org/10.1016/j.conengprac.2010.06.006>.
- [5] Buzás, J.; Farkas, I. Solar domestic hot water system simulation using blockoriented software. In *The 3rd ISES-europe Solar World Congress; CD-ROM Proceedings*; København, Denmark, 2000; pp. 1–9.
- [6] Buzás, J.; Farkas, I.; Biró, A.; Németh, R. Modelling and simulation aspects of a solar hot water system. *Math. Comput. Simul.* 1998, 48, 33–46. [https://doi.org/10.1016/S0378-4754\(98\)00153-0](https://doi.org/10.1016/S0378-4754(98)00153-0).
- [7] Cao, E. *Heat Transfer in Process Engineering*, 1st ed.; McGraw-Hill Education: New York, NY, USA, 2010; ISBN: 9780071624084.
- [8] Castellanos, L.S.M.; Noguera, A.L.G.; Velásquez, E.I.G.; Caballero, G.E.C.; Lora, E.E.S.; Cobas, V.R.M. Mathematical modeling of a system composed of parabolic trough solar collectors integrated with a hydraulic energy storage system. *Energy* 2020, 208, 118255. <https://doi.org/10.1016/j.energy.2020.118255>.
- [9] Engineering Toolbox. Available online: https://www.engineeringtoolbox.com/overall-heat-transfer-coefficient-d_434.html (accessed on 15 February 2025).
- [10] Géczi, G.; Kicsiny, R.; Hungarian University of Agriculture and Life Sciences. Apparatus for Preparing Food with Solar Energy and/or for Heating Liquid, Utility Model Protection, Hungarian Intellectual Property Office. Patent 5489, 27 October 2021. (In Hungarian).
- [11] Géczi, G.; Kicsiny, R.; Korzenszky, P. Modified effectiveness and linear regression based models for heat exchangers under heat gain/loss to the environment. *Heat Mass Transf.* 2019, 55, 1167–1179. <https://doi.org/10.1007/s00231-018-2495-z>.
- [12] Getnet, M.Y.; Gunjo, D.G.; Sinha, D.K. Experimental investigation of thermal storage integrated indirect solar cooker with and without reflectors. *Results Eng.* 2023, 18, 101022. <https://doi.org/10.1016/j.rineng.2023.101022>.
- [13] Gupta, P.K.; Misal, A.; Agrawal, S. Development of low cost reflective panel solar cooker. *Mater. Today Proc.* 2021, 45, 3010–3013. <https://doi.org/10.1016/j.matpr.2020.12.004>.

- [14] Hiris, D.P.; Pop, O.G.; Balan, M.C. Analytical modeling and validation of the thermal behavior of seasonal storage tanks for solar district heating. *Energy Rep.* 2022, 8, 741–755. <https://doi.org/10.1016/j.egy.2022.07.113>.
- [15] Hosseinzadeh, M.; Faezian, A.; Mirzababae, S.M. Parametric analysis and optimization of a portable evacuated tube solar cooker. *Energy* 2020, 194, 116816. <https://doi.org/10.1016/j.energy.2019.116816>.
- [16] Hosseinzadeh, M.; Sadeghirad, R.; Zamani, H.; Kianifar, A.; Mirzababae, S.M. The performance improvement of an indirect solar cooker using multi-walled carbon nanotube-oil nanofluid: An experimental study with thermodynamic analysis. *Renew. Energy* 2021, 165, 14–24. <https://doi.org/10.1016/j.renene.2020.10.078>.
- [17] Hottel, H.C.; Woertz, B.B. The performance of flat plate solar heat collectors. *Trans. ASME* 1942, 64, 91-104.
- [18] Kalita, N.; Muthukumar, P.; Dalal, A. Performance investigation of a hybrid solar dryer with electric and biogas backup air heaters for chilli drying. *Therm. Sci. and Eng. Prog.* 2024, 52, 102646. <https://doi.org/10.1016/j.tsep.2024.102646>.
- [19] Kalogirou, S.A.; Panteliou, S.; Dentsoras, A. Modeling of Solar Domestic Water Heating Systems Using Artificial Neural Networks. *Sol. Energy* 1999, 65, 335–342. [https://doi.org/10.1016/S0038-092X\(99\)00013-4](https://doi.org/10.1016/S0038-092X(99)00013-4).
- [20] Kicsiny, R. Black-box model for solar storage tanks based on multiple linear regression. *Renew. Energy* 2018, 125, 857–865. <https://doi.org/10.1016/j.renene.2018.02.037>.
- [21] Kicsiny, R. Multiple linear regression based model for solar collectors. *Sol. Energy* 2014, 110, 496–506. <https://doi.org/10.1016/j.solener.2014.10.003>.
- [22] Mehling, H. Use of phase change materials for food applications—State of the art in 2022. *Appl. Sci.* 2023, 13, 3354. <https://doi.org/10.3390/app13053354>.
- [23] Rátkai, M.; Géczi, G.; Kicsiny, R.; Székely, L. New Physically-Based Mathematical Model and Experiments for a Recently Invented Solar Pot. *Appl. Sci.* 2024, 14, 6643. <https://doi.org/10.3390/app14156643> (c)
- [24] Rátkai, M.; Géczi, G.; Székely, L. Investigation of the Hottel–Whillier–Bliss Model Applied for an Evacuated Tube Solar Collector. *Eng* 2024, 5, 3427-3438. <https://doi.org/10.3390/eng5040178> (a)
- [25] Rátkai, M.; Kicsiny, R.; Székely, L. Modelling of a recently invented solar pot. *An. Tech. Szeg.* 2024, 18:2, 38-48. <https://doi.org/10.14232/analecta.2024.2.38-48> (b)
- [26] Saini, P.; Pandey, S.; Goswami, S.; Dhar, A.; Mohamed, M.E.; Powar, S. Experimental and numerical investigation of a hybrid solar thermal-electric powered cooking oven. *Energy* 2023, 280, 128188. <https://doi.org/10.1016/j.energy.2023.128188>.
- [27] Saxena, A.; Cuce, E.; Tiwari, G.N.; Kumar, A. Design and thermal performance investigation of a box cooker with flexible solar collector tubes:

- An experimental research. *Energy* 2020, 206, 118144. <https://doi.org/10.1016/j.energy.2020.118144>.
- [28] Székely, L.; Kicsiny, R.; Hermanucz, P.; Géczi, G. Explicit analytical solution of a differential equation model for solar heating systems. *Sol. Energy* 2021, 222, 219–229. <https://doi.org/10.1016/j.solener.2021.05.007>.
- [29] USDA (Food Safety and Inspection Service, U.S. Department of Agriculture). Safe Minimum Internal Temperature Chart. Available online: <https://www.fsis.usda.gov/food-safety/safe-food-handling-and-preparation/food-safety-basics/safe-temperature-chart> (accessed on 15 February 2025).
- [30] Víg, P.G. Modelling of Solar Collector Systems with Neural Network. Ph.D. Thesis, Szent István University, Gödöllő, Hungary, 2007. (In Hungarian).
- [31] Zheng, J.; Febrer, R.; Castro, J.; Kizildag, D.; Rigola, J. A new high-performance flat plate solar collector. Numerical modelling and experimental validation. *Appl. Energy* 2023, 355, 122221. <https://doi.org/10.1016/j.apenergy.2023.122221>.
- [32] Zhou, C.; Wang, Y.; Li, J.; Ma, X.; Li, Q.; Yang, M.; Zhao, X.; Zhu, Y. Simulation and economic analysis of an innovative indoor solar cooking system with energy storage. *Sol. Energy* 2023, 263, 111816. <https://doi.org/10.1016/j.solener.2023.111816>.
- [33] Zohuri, B. Compact Heat Exchangers, Selection, Application, Design and Evaluation; Springer International Publishing, Cham, Switzerland, 2017. <https://doi.org/10.1007/978-3-319-29835-1>.

Tribological evaluation of glass fiber reinforced epoxy (GFRP) composites using pin-on-disc abrasion tests

Tamás György SÁRKÁNY¹, Gábor KALÁCSKA², Róbert KERESZTES²

¹ Doctoral School of Mechanical Engineering, MATE Gödöllő

² Department of Materials Science and Engineering Processes, Institute of Technology, Hungarian University of Agriculture and Life Sciences, MATE Gödöllő

Abstract

This study investigates the tribological behavior of glass fiber reinforced epoxy (GFRP) composites under abrasive wear conditions using a pin-on-disc experimental setup. GFRP composites are widely used in automotive, aerospace, and structural applications due to their high strength-to-weight ratio and corrosion resistance; however, their wear performance in abrasive environments remains a critical concern. The research focuses on evaluating abrasive wear resistance by incorporating controlled abrasive particulate media (e.g., silica sand) between the composite pin and rotating steel disc. Key parameters, including applied load, sliding velocity, abrasive particle size, and filler concentration, were systematically varied to analyze their influence on wear rate and friction coefficient. Wear mechanisms were characterized using confocal microscopy to identify surface degradation modes such as fiber fragmentation, matrix cracking, and particle embedment. This study presents a measurement method that the authors developed to subsequently determine the wear properties of composite material pairings based on an experimental design.

Keywords

epoxy, glass fiber composite, adhesive wear, abrasive wear, pin-on-disc wear

1. Introduction

Glass fiber reinforced epoxy composites are widely used in various industries due to their desirable mechanical properties, corrosion resistance, and cost-effectiveness. Understanding the tribological behavior of these composites is crucial for their successful application in dynamic and wear-prone environments. This study aims to investigate the wear resistance of glass fiber reinforced epoxy composites under abrasive wear conditions using a pin-on-disc experimental setup. The tribological behavior of glass fiber reinforced epoxy composites is influenced by various factors, such as normal load, sliding velocity, and the presence of abrasive particulates (Sarkar et al., 2017). Previous studies have

reported the effects of these parameters on the friction and wear characteristics of these composites. (Sarkar et al., 2017) (Suresha et al., 2006) (Berg et al., 1973) The current study seeks to build upon these findings and provide a comprehensive understanding of the wear resistance of glass fiber reinforced epoxy composites under abrasive conditions. In this work, a pin-on-disc experimental setup was employed to evaluate the tribological performance of glass fiber reinforced epoxy composites. In our article, we present the procedure we developed, which, we hope, can be used to test the wear resistance of composite components under mixed wear conditions. The university has a long tradition of wear testing. Among other things, our researchers have tested the wear properties of closed-cell aluminum foams made by direct foaming and gas injection and their matrix materials using a pin-on-disc testing device. (Gábora, 2020) Researchers developed AlSi12 aluminum syntactic foams reinforced with iron (GM) and ceramic (GC, SLG) hollow spheres via low-pressure infiltration. Pin-on-disc tests against steel under dry/lubricated conditions showed friction and wear depended on reinforcement type. GC ceramic spheres in lubricated tests provided optimal performance ($\mu \approx 0.08\text{--}0.12$), leveraging oil retention for enhanced wear resistance. (Májlinger, 2016)

During the development of the procedure, a key consideration was to simultaneously induce adhesive wear and abrasive wear during testing. To achieve this, the pin-on-disc method was augmented with the addition of abrasive particles. Another critical aspect was ensuring the procedure remained relatively rapid and enabled the comparison of multiple composite types under identical parameters. Microscopy measurements were conducted to quantify the extent of wear and characterize the surface morphology. Preliminary testing was performed to validate the functionality of the methodology and demonstrate its efficacy. The materials employed in the preliminary tests are detailed below.

2. Materials and methods

The matrix material

In our research, we use an epoxy resin matrix. Structural epoxy resins are widely employed in various industrial applications due to their exceptional mechanical properties, chemical resistance, and dimensional stability. A review of the published literature reveals that many researchers have investigated the wear properties of epoxy resins, but these studies always attempt to achieve better properties by adding some type of material. Jakab and colleagues incorporated reinforced materials (polymer and mineral fillers) into epoxy resin matrices and examined the improvement in the overall performance of the composites, which could enable the industrial application of these materials in environments subjected to intense wear. (Jakab, 2021)

It is difficult to find a clear consensus in the literature regarding the wear properties of certain polymer matrix materials. Wear resistance is a complex concept, as it encompasses various factors such as abrasion, friction, and surface degradation during use (Radmanovac et al., 2017). The wear properties of structural epoxy resins are influenced by numerous factors, including the chemical composition of the resin, the presence and distribution of fillers or reinforcements, the curing process, and the environmental conditions to which the material is exposed. (Pham, H., 2005) Therefore, it is not meaningful to study the standalone wear properties of epoxy resins, as the reinforcing phase of the composite structure significantly influences the final properties.

In our research, we used **MGS LR 635** laminating epoxy resin as the matrix and **MGS LH 635** hardener for manufacturing the test specimens. This is a type of resin widely used in Hungary and applied across numerous fields. The choice of this resin was based on its common usage, ensuring that the results can be utilized in many industrial contexts. The resin-to-hardener ratio was 100:33.

Table 1. Main mechanical properties of the epoxy matrix

| Material | Cured density | Tensile modulus | Tensile strength | Yield strain | Bending modulus | Bend strength |
|----------|----------------------|------------------|------------------|------------------|-----------------|----------------|
| | | DIN EN ISO 527-2 | DIN EN ISO 527-2 | DIN EN ISO 527-2 | DIN EN ISO 178 | DIN EN ISO 178 |
| | [g/cm ³] | [GPa] | [MPa] | % | [GPa] | [MPa] |
| LH635 | 1.15 – 1.20 | ~ 3.6 | ~ 85 | ~ 6 | ~ 3.8 | ~ 140 |

The fiber reinforcement material

The wear behavior of glass fiber-reinforced epoxy composites has been compared to that of carbon/aramid hybrid-reinforced epoxy composites. The results showed that the substitution of the glass fiber weave with the carbon/aramid weave led to a 35% reduction in the coefficient of friction on average. Additionally, the carbon/aramid hybrid-reinforced epoxy composites demonstrated superior wear performance under milder sliding conditions, with the wear rate being an average factor of 22 lower than that of the glass fiber-reinforced epoxy composites (Larsen et al., 2006). This suggests that the choice of fiber reinforcement can significantly impact the tribological properties of polymer-based materials, and alternative reinforcement options such as carbon/aramid hybrids may be more suitable for applications requiring low friction and high wear resistance. However, glass fiber-reinforced epoxy

composites have demonstrated excellent abrasion resistance in pin-on-disc experiments, making them a viable choice for applications where high wear resistance is a priority. (Jawad, 2019) On effect of the wearing the adhesive bond is continuing to decrease, which strength of composite structure leads to reduction. That is why, the protection against wear plays very important role in assurance of durability of composite materials and long lifetime (Suresha et al., 2006)

For the test specimens, we used a plain weave fabric with a density of 220 g/m². Another key consideration in selecting the fiber reinforcement was to choose a material that is widely used in industrial applications. The fabric type, designated as **UTE 220 P**, is a fiber reinforcement material with a surface treatment compatible with E-type epoxy resin.

Table 2. Main mechanical properties of the glass fiber (Ku, 2011)

| Material | Cured density | Tensile strength | Yield strain | Bending modulus |
|-----------------|---------------------------|-------------------------|---------------------|------------------------|
| | [g/cm³] | [MPa] | % | [GPa] |
| UTE 220 P | 2.5 | ~ 2000 | ~ 0.5 | ~ 70 |

Manufacturing the specimen

The fabrication of the glass fiber reinforced epoxy composite materials involved a hand lay-up technique followed by compression molding. This process resulted in a woven E-glass fiber reinforced epoxy composite with a fiber content of 45 wt%. The fiberglass reinforcement was laminated in 6 layers, thus producing test specimens with a thickness of 1.5 mm.

The wear process was interrupted twice. To ensure precise microscope positioning, alignment interfaces were fabricated on the specimen to enable accurate repositioning. The specimen surfaces were not pretreated prior to measurements. The geometric shaping of the composite plate was achieved via CNC milling. The figure below illustrates the composite plate fabrication process on the left and the technical drawing of the specimen on the right.

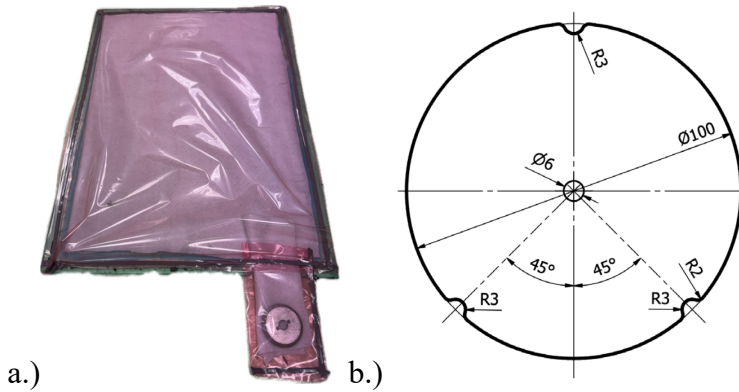


Figure 1. a.) the composite plate fabrication process b.) The technical drawing of the specimen

Pin-on disc procedure

The working principle of the pin-on-disc wear measurement is relatively simple. A specimen, typically in the form of a pin, is placed in contact with a rotating disc, which is made of the material to be tested. The pin is pressed against the disc with a specific normal force, and the disc is rotated at a constant angular velocity, causing the pin to slide against the disc surface. During the test, the mass loss of the pin or the depth of wear on the disc is measured to determine the wear rate of the material. (Sarkar et al., 2017) The figure below illustrates the schematic of the measurement setup. The wear pin comprises a hardened bearing ball, which was adhered to the pin shaft to establish a thermally neutral bond (i.e., without heat input). The bearing ball exhibits a hardness of 38 HRC. This bearing ball was pressed onto the specimen surface during testing.

The pin-on-disc setup allows for the controlled evaluation of various parameters that influence the wear behavior of materials, such as the normal load, sliding speed, sliding distance, and the properties of the materials involved. The specific wear rate, which is the volume of material lost per unit of sliding distance and normal force, is often used as the primary measure of the wear performance of the tested materials. The results of the tribological evaluation reveal that the friction and wear behavior of the glass fiber reinforced epoxy composite are influenced by the duration of sliding, normal load, and sliding velocity. (Sarkar et al., 2017) Increased normal load was found to lead to higher wear, while the coefficient of friction decreased. Conversely, higher sliding velocities resulted in increased wear, while the coefficient of friction initially peaked at 5.01 m/s before decreasing. (Singh et al., 2021)

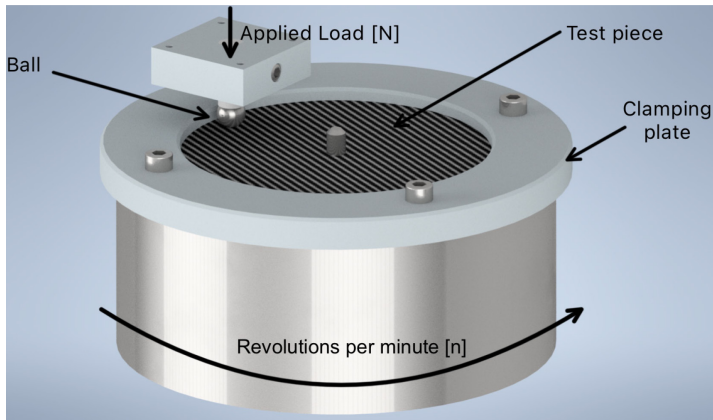


Figure 2. Schematic diagram of the pin-on-disc procedure

The wear rate is calculated using the equation: $W = \Delta m / (\rho * L * F_n)$, where W is the specific wear rate, Δm is the mass loss of the specimen, ρ is the density of the specimen, L is the sliding distance, and F_n is the normal load applied. This equation allows researchers to quantify the material's resistance to wear under the specified test conditions. The specific wear rate, W , represents the volume of material removed per unit of sliding distance and normal force, providing a standardized metric to compare the wear performance of different materials. By measuring the mass loss, Δm , of the specimen and incorporating the density, ρ , sliding distance, L , and normal load, F_n , this formula enables a comprehensive evaluation of the wear characteristics. This information is crucial for understanding the tribological behavior of materials and selecting appropriate ones for applications involving sliding or abrasive wear. (Jawad, 2019). The pin-on-disc wear test is a versatile technique that can be used to study the wear behavior of a wide range of materials, including metals, ceramics, polymers, and their composites. As an example, a study on the sliding wear of blended cobalt-based alloys found that the pin-on-disc experiment revealed a more complex relationship between the alloy composition and the wear rate (Ahmed et al., 2020).

During the preliminary testing, the wear testing machine completed three 50-meter intervals, totaling 150 meters of sliding distance. Interruptions were necessitated by intermediate microscopy measurements to assess wear progression. A constant applied load of 7 N was maintained throughout the test. The ball abraded the specimen along a wear track with a radius of 33.5 mm at a circumferential speed of 0.05 m/s. Abrasive quartz sand, with an average particle size of 100 μm , was utilized during the wear process. To ensure continuous retention of the sand within the contact zone, deflector blades were employed. Data acquisition was performed using the HBM Catman system. HBM catman is a professional data acquisition and analysis software primarily used for

engineering measurements, such as mechanical load testing, vibration analysis, and strain measurement. The software is capable of recording signals in real time (e.g., pressure, force, acceleration, temperature) from sensors (e.g., strain gauges, load cells, accelerometers), followed by analysis, visualization, and documentation of the acquired data. The speed, pin displacement and normal forces were recorded during the measurement. The measurements were made at 22 °C and 60% humidity. The figure 3. shows the device in operation.



Figure 3. The abrasive pin-on-disc method during measurement

Results and dicussion

The measurement results

Phase 3 of the Measurement: The increase in the wear mark is clearly visible. The first picture shows the 50-meter run, the second the 100-meter run, and the third the 150-meter run. It is clear that during wear the fibers always stand in a different direction compared to the wear. First the fibers lie at 0° and 90°, then after a 45° turn at 45-45°.

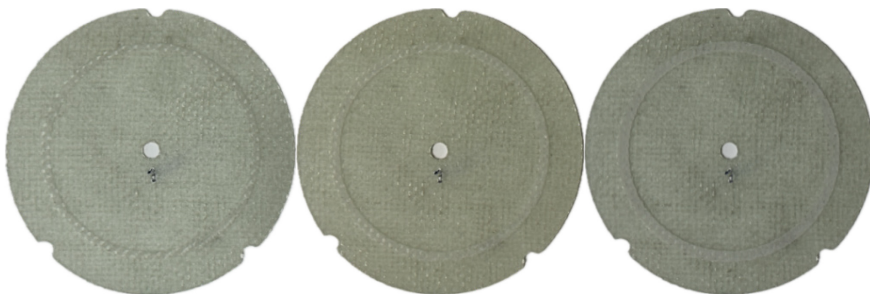


Figure 4. The pin-on-disc method during measurement

The friction coefficient (μ) typically exhibits two distinct phases during tribological interactions:

1. **Initial (Run-In) Phase:** During this stage, the contact points between the surfaces have not yet fully adapted. As a result, the value of μ may fluctuate and remain relatively high due to the macroscopic roughness of the surfaces.
2. **Steady State:** After partial surface conformity and the embedding of wear debris, μ stabilizes into an equilibrium state. This phase is most relevant for predicting long-term behavior under continuous sliding conditions.

For example, in glass fiber-reinforced epoxy (GFRP) composites, the friction coefficient generally ranges between 0.2 and 0.4 against a steel counterpart, depending on fiber orientation and the adhesive properties of the matrix. A parallel orientation of the fibers relative to the sliding direction can reduce μ , as the aligned fibers help mitigate macro-scale damage by distributing stresses more effectively. (Hansen et al., 2020) These experiences can be clearly observed in the following diagram. At first the coefficient of friction is high, then it decreases and stagnates. Finally, as the ball goes deeper and deeper, it comes into contact with the specimen over an increasingly larger surface area and the coefficient of friction increases.



Figure 5. The friction coefficient

The following figure shows the amount of wear in millimeters. The figure clearly shows that this process shows a linear curve, which is also interesting

because we are pressing a ball into the test specimen. It would seem logical that the more the test specimen wears, the larger the surface area of the ball's surface is in contact with the test specimen and the slower it wears. But this is not what can be observed in this experiment. We saw that the ball also lost a lot of its material. About 0.09 mm was also worn off the ball. Thus, we came to the conclusion. That the abrasive effect of the grains was much higher than that of the ball. I believe the ball also wore a lot. The total wear of the test specimen is 0.21 mm.

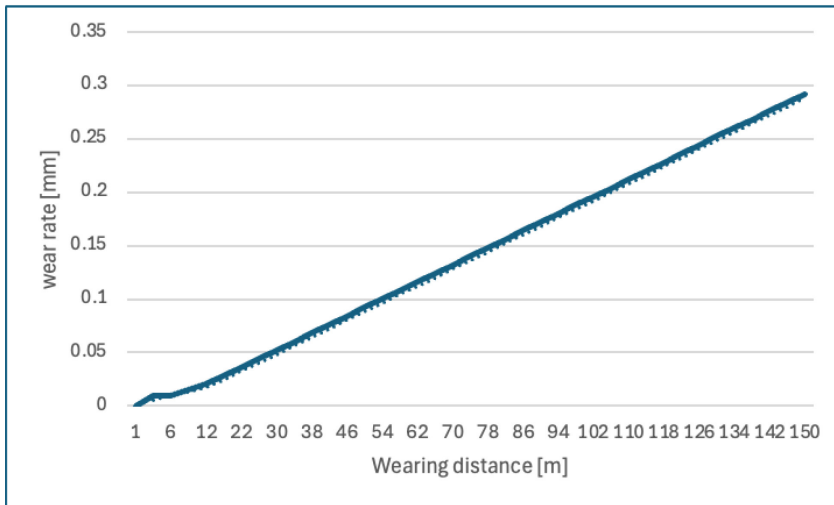


Figure 6. Wear distance and wear rate on a diagram

Rabinovicz's abrasion wear model, a seminal contribution to the field of tribology, has long been recognized as a fundamental framework for understanding the complex mechanisms underlying the wear of materials subjected to abrasive conditions. The Rabinovicz model, first introduced in the 1960s, provides a systematic approach to predicting the wear behavior of materials under abrasive conditions (Altaie et al., 2017). At the core of the model is the recognition that wear is a complex interplay between the material properties, the nature of the abrasive medium, and the operating conditions. Rabinovicz posited that the wear rate of a material is directly proportional to the applied load and inversely proportional to the hardness of the material, a relationship that has been widely validated through extensive empirical studies. (Amrishraj & Senthilvelan, 2018) The experimental results confirm a clear correlation between wear depth and the Rabinowicz abrasive wear model. The material loss of the GFRP composite specimen (0.21 mm) and the steel ball (0.09 mm) over a 150 m sliding distance exhibited a linear trend, consistent with the fundamental equation of the Rabinowicz model: $W=H/k \cdot L$, where “ k ” is the

wear coefficient (dependent on material and abrasive particle properties), " $L=L_n$ " is the applied load (7 N), and " H " is the hardness of the wearing material. According to this model, material loss is proportional to the load and the hardness of the abrasive particles (quartz sand, ~1100 HV), while inversely proportional to the hardness of the specimen (~200–300 HV). The hard quartz sand particles effectively cut into the softer composite surface, resulting in the observed linear wear curve. This behavior is a typical example of two-body abrasion, where particles act as fixed abrasives.

The Olympus OLS5000 3D Laser Microscope in Wear Testing

The Olympus OLS5000 3D laser confocal microscope serves as a key instrument in wear testing, aiding in the understanding of wear mechanisms and the quantitative analysis of surface degradation. This is particularly crucial in industrial applications where components are exposed to particle abrasion, friction, or repetitive mechanical loading. As a measurement tool, the Olympus OLS5000 enables detailed, non-destructive observation of wear processes and the precise documentation of surface changes at the nanometer scale. Its laser confocal technology focuses light reflected from the surface, allowing for "optical sectioning" and the generation of a 3D topographic image of the sample's surface. This method is ideal for measuring micro-scratches, craters, or changes in surface roughness resulting from wear. For instance, following pin-on-disc or tribometer experiments, the microscope allows for accurate quantification of wear track depth, the distribution of surface irregularities, and the extent of particle embedding or matrix delamination.

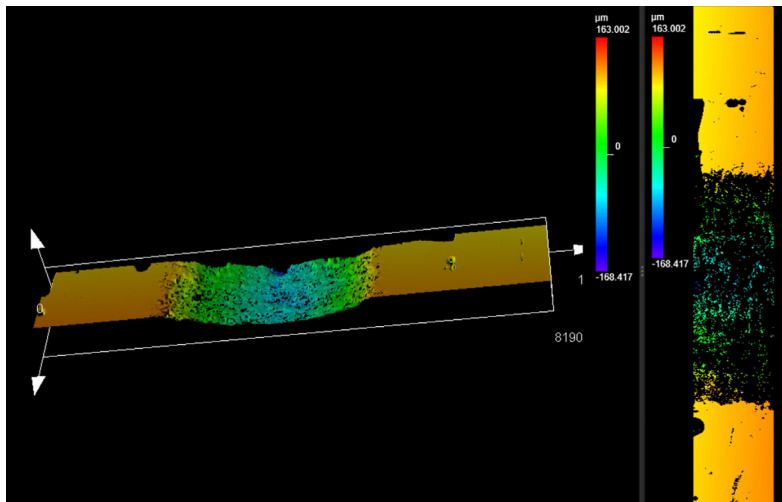


Figure 7. The Olympus OLS5000 3D Laser Microscope in Wear Testing

Future plans for wear test: In future work, we plan to implement a three-factor experimental design to further investigate the same material. The study will systematically evaluate the effects of applied load, sliding distance, and sliding speed on wear behavior under controlled abrasive conditions. The experimental matrix will include:

- **Applied load:** 7 N, 14 N, and 21 N,
- **Sliding distance:** 50 m, 100 m, and 150 m,
- **Sliding speed:** 0.05 m/s, 0.1 m/s, and 0.15 m/s.

The experimental design will follow the pin-on-disc methodology outlined in our previous study, ensuring consistency in test parameters such as counterface material (hardened steel disc), abrasive particulate type (e.g., silica sand), and environmental conditions (temperature, humidity). By employing a full factorial design ($3 \times 3 \times 3$), we aim to generate a comprehensive dataset to quantify the individual and interactive effects of these variables on wear rate, friction coefficient, and surface degradation mechanisms. Statistical tools, such as ANOVA (Analysis of Variance), will be applied to identify the dominant factors influencing tribological performance. Subsequently, abrasive-free wear tests will be conducted to isolate and analyze pure adhesive wear mechanisms on the specimens. These tests will eliminate abrasive particulates to investigate how surface interactions (e.g., micro-welding, plastic deformation, or material transfer) contribute to wear in the absence of third-body abrasion. Comparative analysis of abrasive vs. non-abrasive wear modes will provide deeper insights into the material's intrinsic wear resistance and interfacial behavior. Post-test characterization using the Olympus OLS5000 3D laser confocal microscope will enable high-resolution quantification of wear track morphology, surface roughness evolution, and subsurface damage. This dual-phase approach (abrasive and adhesive wear studies) will facilitate the development of predictive wear models and inform material optimization strategies for applications requiring tailored resistance to specific wear mechanisms. This systematic investigation will advance the understanding of multifactorial wear dynamics in fiber-reinforced composites, bridging the gap between laboratory-scale testing and real-world operational conditions. The results are expected to guide the selection of optimal operational parameters and material formulations for industries such as automotive, aerospace, and heavy machinery, where component longevity under complex wear scenarios is critical.

4. Conclusion

- The method is highly suitable for wear analysis of composite materials. The wear track generated during testing is well-defined and measurable, yet the process does not induce significant frictional heating that could thermally degrade the composite matrix (e.g., epoxy softening or fiber-matrix interface weakening). This ensures the preservation of the sample's intrinsic mechanical properties during testing, enabling accurate post-test characterization.
- The methodology provides a robust framework for future experimental designs. Its repeatability, scalability, and compatibility with standardized protocols (e.g., ASTM G99 for pin-on-disc testing) make it ideal for systematic studies investigating additional variables such as environmental conditions (humidity, temperature), alternative abrasive media, or multi-axis loading scenarios.
- Microscopic measurements (e.g., 3D laser confocal microscopy, SEM) enable precise quantification of: Geometric changes: Depth/width of wear tracks, volume loss via 3D topographical mapping. Surface roughness evolution: Parameters such as S_a (arithmetical mean height) or S_z (maximum height) calculated from profilometry data. Material loss: Cross-sectional analysis or mass loss measurements validated by gravimetric methods. These data are critical for correlating wear mechanisms (e.g., abrasive ploughing, adhesive transfer) with operational parameters, supporting predictive wear modeling and material optimization.

However, the experiment revealed that the wear of the specimen (0.21 mm) was nearly twice that of the steel ball (0.09 mm). This contradicts traditional two-body abrasion models, where counterface (steel ball) wear is negligible. Instead, the phenomenon suggests a dominant third-body abrasion mechanism, where the abrasive action of the quartz sand particles significantly exceeds the direct wear caused by the ball.

Furthermore, the friction coefficient (μ) exhibited a more complex behavior. As shown in Figure 5 of the article, μ varied across three distinct phases:

1. **Initial phase (0–50 m):** High μ (~ 0.23) due to surface roughness and initial embedding of abrasive particles.
2. **Stabilization phase (50–100 m):** Declining μ (~ 0.1) as surfaces partially conformed and abrasive particles distributed more evenly.
3. **Late phase (100–150 m):** Renewed μ increase (~ 0.15), despite the reduced specific load caused by expanding contact area.

This periodic fluctuation in μ cannot be explained by the simplified framework

of the Rabinowicz model. Instead, it reflects the dynamic role of third-body quartz sand particles, which intermittently cut into surfaces, rolled, or detached from the contact zone. To fully understand these interactions, further experiments are required to analyze particle dynamics, including their size, concentration, and real-time movement during abrasion.

References

- [1] Ahmed, R., Lovelock, H. L. de V., & Davies, S. (2020). Sliding wear of blended cobalt based alloys. In *Wear* (p. 203533). Elsevier BV. <https://doi.org/10.1016/j.wear.2020.203533>
- [2] Altaie, A., Bubb, N. L., Franklin, P., Dowling, A. H., Fleming, G. J. P., & Wood, D. J. (2017). An approach to understanding tribological behaviour of dental composites through volumetric wear loss and wear mechanism determination; beyond material ranking. In *Journal of Dentistry* (Vol. 59, p. 41). Elsevier BV. <https://doi.org/10.1016/j.jdent.2017.02.004>
- [3] Amrishraj, D., & Senthilvelan, T. (2018). Dry Sliding wear behavior of ABS Composites reinforced with nano Zirconia and PTFE. In *Materials Today Proceedings* (Vol. 5, Issue 2, p. 7068). Elsevier BV. <https://doi.org/10.1016/j.matpr.2017.11.371>
- [4] Berg, C. A., Batra, S., & Tirosh, J. (1973). Wear and friction of two different types of graphite fibre-reinforced composite materials. In *Fibre Science and Technology* (Vol. 6, Issue 3, p. 159). Elsevier BV. [https://doi.org/10.1016/0015-0568\(73\)90018-3](https://doi.org/10.1016/0015-0568(73)90018-3)
- [5] Gábora, A., Kalácska, G., Keresztes, R. Z., Beke, S., & Géresi, Z. G. (2020). Pin on disc vizsgálatok zártcellás alumíniumhabokon.
- [6] Hansen, J., Björling, M., & Larsson, R. (2020). Lubricant film formation in rough surface non-conformal conjunctions subjected to GPa pressures and high slide-to-roll ratios. *Scientific Reports*, 10(1), 22250.
- [7] Jakab, B., Panaitescu, I., & Gamsjäger, N. (2021). The action of fillers in the enhancement of the tribological performance of epoxy composite coatings. *Polymer Testing*, 100, 107243.
- [8] Jawad, D. K. (2019). Sliding Wear Test and Also SEM Study on Epoxy Reinforced Glass Fibre Composite Along with the Fillers of Black Granite Powder, White Granite Powder as Well as Stone Powd. In *International Journal of Engineering Research and (Issue 12)*. International Research Publication House. <https://doi.org/10.17577/ijertv8is120180>

- [9] Ku, H., Wang, H., Pattarachaiyakoop, N., & Trada, M. (2011). A review on the tensile properties of natural fiber reinforced polymer composites. *Composites Part B: Engineering*, 42(4), 856-873..
- [10] DOI: <https://doi.org/10.1016/j.compositesb.2011.01.010>
- [11] Larsen, T. Ø., Andersen, T. L., Thorning, B., Horsewell, A., & Vigild, M. E. (2006). Comparison of friction and wear for an epoxy resin reinforced by a glass or a carbon/aramid hybrid weave. In *Wear* (Vol. 262, p. 1013). Elsevier BV. <https://doi.org/10.1016/j.wear.2006.10.004>
- [12] Májlinger, K., Bozóki, B., Kalácska, G., Keresztes, R., & Zsidai, L. (2016). Tribological properties of hybrid aluminum matrix syntactic foams. *Tribology International*, 99, 211-223.
- [13] Pham, H., & Marks, M. J. (2005). Epoxy Resins. In *Ullmann's Encyclopedia of Industrial Chemistry*. https://doi.org/10.1002/14356007.a09_547.pub2.
- [14] Radmanovac, N., Ćirković, N., & Šarac, T. (2017). The importance of the resistance to wear in the choice of fabrics for protective garments. In *Advanced technologies* (Vol. 6, Issue 1, p. 81). <https://doi.org/10.5937/savteh1701081r>
- [15] Sarkar, P., Modak, N., & Sahoo, P. (2017). Effect of Normal Load and Velocity on Continuous Sliding Friction and Wear Behavior of Woven Glass Fiber Reinforced Epoxy Composite. In *Materials Today Proceedings* (Vol. 4, Issue 2, p. 3082). Elsevier BV. <https://doi.org/10.1016/j.matpr.2017.02.191>
- [16] Singh, T., Goswami, C., Kumar, S. R., & Singh, S. (2021). Tribological properties of fiber reinforced phenolic composites under sliding condition. In *Materials Today Proceedings* (Vol. 47, p. 6231). Elsevier BV. <https://doi.org/10.1016/j.matpr.2021.05.190>
- [17] Suresha, B., Chandramohan, G., Renukappa, N. M., & Siddaramaiah. (2006). Mechanical and tribological properties of glass–epoxy composites with and without graphite particulate filler. In *Journal of Applied Polymer Science* (Vol. 103, Issue 4, p. 2472). Wiley. <https://doi.org/10.1002/app.25413>

Development of laboratory static fracture tests for milling tools

László ZSIDAI¹, Benjámín MARKOVICS¹, Tamás PATAKI¹,
Zoltán SZAKÁL¹, István SZABÓ¹, Norbert SCHREMPF¹,
Róbert KERESZTES¹

¹ *Institute of Technology, Hungarian University of Agriculture and Life Sciences, MATE, Gödöllő*

Abstract

This study uses a unique laboratory experimental system to explore the breakage of milling tools. The breakdown of milling tools, in addition to wear, is most often is the break. With this, in addition to the tool cost, the cost of the destroyed raw material can also be high. Predictive tool failure prediction is required to avoid tool errors. Our work is related to the development of a comprehensive predictive system, as part of which we present the development of the laboratory static tool fracture testing system and its extension in the direction of FEM simulations. The results showed that the simulation programs can be used appropriately to develop a predictive tool breakage prediction system. The test system can be economically designed and used as a system element within complex tests. At the same time, fracture tests can be well linked to FEM simulation as well.

Keywords

predictive; milling; breakage of tool; laboratory test; FEM

1. Introduction

The parameters of the milling greatly influence the product and the cost. The use of the right parameters is essential for economical machining. However, excessive reduction of the machine main time can be an extremely large additional load on the tool. Finding the ideal settings and the optimum parameters is therefore essential, as in addition to the broken tool, the cost of the damaged product is also high, and machining that is too slow increases the cost of production in the same way. Manufacturers therefore need to know what parameters they can work with.

In our work, we present a static fracture test laboratory test method developed as part of a comprehensive predictive tool failure prediction system. Static fracture testing alone, of course, is not enough to form a comprehensive view of a

particular tool. At the same time, as an element of a complex system, it provides basic initial information for later basic data.

By presenting the static fracture test method we used and prepared, our primary goal is to present a simplified and economical test system. It can be used for industrial purposes in addition to educational research tasks. We also consider it important to validate the test system with the FEM procedure, which computer simulation will play a significant role in the future development of the system.

Tool breaks during milling

The service life of rotary cutting tools is affected by a number of factors. It is very important to choose a well-chosen tool material according to the material to be machined, as well as the geometry, design and setting of the appropriate technological parameters.

There are basically two needs for machining. The finished product can be produced in the right quality and economically. Ideally, the workpiece is actually produced in the desired quality, with adequate productivity and cost factors. However, this is true in the rarest of cases. Technological parameters may deviate from the values specified by the programmer, unexpected errors may occur during machining. Control systems are used to eliminate these problems. Increasing the efficiency of cutting machining can be solved by maximizing the utilization of the cutting tool. CNC cutting machines are effective tools for increasing utilization. However, maximizing tool utilization beyond a limit reduces efficiency due to tool damage. Ideally, the best use of a tool lasts until it breaks down if it is replaced before the critical time (the moment of failure). If it is replaced earlier, the tool has not been used and compared to this theoretical ideal condition, the tool is specifically more expensive and there is more waste.

Tool life is limited by wear on the cutting edge. The area of wear is well mapped, the different forms of wear can be well analyzed. Basic tool wear: abrasive wear, diffusion wear, oxidation wear, fatigue wear, adhesion wear, surface wear, crater wear, back wear, plastic deformation, edge helmet formation, heat cracking, chipping, edge breakage. (Fig. 1)

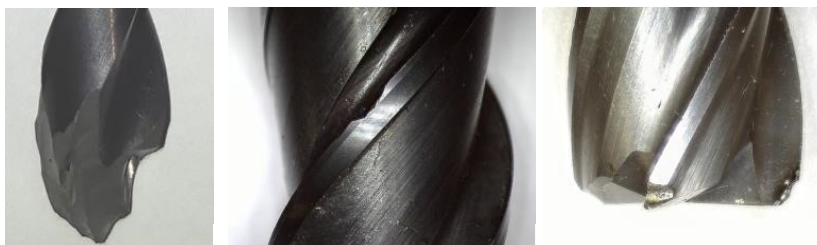


Figure 1. Typical milling tool fractures: full cross section, edge breakout, corner breakout (source: MATE UNIVERSITY-Lab of Material Science)

The break is due to tool overload. Many factors work together on the tool during machining. As a result, harmful vibrations can occur in many cases, which can cause damage to the cutting edge of the tool. The presence of vibrations in the cutting process is undesirable. The breakouts and chippings of the cutting edges mostly suggest some harmful vibrations. They also have a detrimental effect on the quality of the finished workpiece. Ultimately, they can also cause premature tool breakage. The phenomenon of harmful vibration has a high noise effect, so it can be detected by the operator. However, harmful vibrations can develop even when they are less audible. Therefore, it is important to monitor the cutting system online and to monitor the vibrations. This allows the system to be operated optimally and to intervene before harmful vibrations occur.

Two different types of measurements are used, including direct measurements (direct indicator of tool wear, e.g., wear width) and indirect measurements (indirect indicator of tool wear, e.g., vibration, cutting force, etc.). From indirect measurements we infer directly to monitor the condition of the tool, while from indirect measurements we infer inferentially using a model-based evaluation method (J. Wang et al, 2013).

Tool manufacturers strive to reduce harmful vibrations during cutting (source: Sandvik Coromant). This can be achieved by designing the edge geometry, applying coatings, or designing the tool body to dampen the resulting vibrations. In milling (Figure 1 left side), generally the tool performs the main movement (rotary movement), and the workpiece performs the secondary movement (movements in X, Y and Z direction). (Fig. 2)

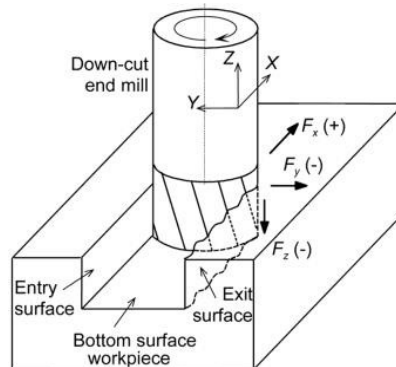


Figure 2. Force components of milling (Luo et al 2007)

The literature on milling tool tests mainly includes tests during dynamic cutting, a brief summary of which can be seen below.

Cutting force and breakage measuring methods in milling

There are two commonly used methods to measure cutting forces in milling. The most common method is to attach the measuring device directly to the workpiece. Another method is when the measuring unit is connected to the milling tool or the spindle near to the tool.

Albrecht et al (2004) measured the cutting forces in milling using capacitive sensors. They installed a capacitance type displacement sensor on the main spindle of a three-axis CNC vertical machining centre.

Altintas and Park (2004) measured the cutting forces in three dimensions with combined sensors in their milling experiment. The spindle of a vertical machining centre was retrofitted with three pairs of piezo-electric sensors. Two pairs of shear sensors (Kistler 9145) were used to measure lateral forces in the feed (x-axis) and normal (y-axis), and a pair of compression sensors (Kistler 9135) were used to measure the axial (z-axis) forces in milling. The signals from each sensor were added and passed through an anti-aliasing filter. The signals were then amplified by the charge amplifiers.

Kaya et al (2011) used a rotating force dynamometer (Kistler 9123C1111 type) for the dynamic and quasistatic measurement of the three force components (F_x , F_y , F_z) as well as of the drive moment M_z on a rotating tool. The output from the cutting dynamometer is transferred with a non-contact Radio Frequency protocol to charge amplifier (Kistler Corporation, Model 5223B). The rotating cutting force type dynamometer (RCD) has advantages over fixed dynamometers, such as the cutting forces can be measured on the rotating tool independently of the size of workpiece and measurement can be performed on any spatial position (four or five axis milling).

Phokobye et al (2019) used multicomponent dynamometer (Kistler 9255C type) for measuring the cutting forces during milling. In their research a solid rectangular work piece of MS 200 TS was clamped to the dynamometer using two holes and the dynamometer was clamped directly to the machine table. Milling operations were thereafter performed for dry cutting using different cutting parameters of cutting speed, feed rate and depth of cut.

Postel et al (2019) used the Cutting force measuring with spindle mounted vibration sensors. The spindle of a 5 axis CNC machining centre is instrumented with 5 accelerometers mounted on the non-rotating housing. The objective was to estimate the cutting forces and vibrations at the tool tip from the accelerometers attached to the housing during machining.

The following literatures examines tool breakage using different analytical and on-line methods.

Y. Altintas et al (1988) describe a simple and efficient algorithm for processing the milling force signal to detect cutter breakage. Using sampling synchronized with cutter teeth the basic variation per tooth is removed by calculating average forces per tooth. The first difference of these forces detects both breakage and some sudden changes in cutting conditions (cornering, milling over a slot). The second difference distinguishes between the two. The

algorithm is illustrated by computational simulations as well as by measurements in milling tests.

Yao et al (2009) introduce a new diagnosis technique for tool breakage in face milling using a support vector machine (SVM). The features of spindle displacement signals are first fed into the kernel-based SVM decision function. After the SVM learning procedure, the SVM can respond in real-time to automatically diagnose tool fracture under varying cutting conditions. Experimental results show that this new approach can detect tool breakage in a wide range of face-milling operations.

C.Y. Wang et al (2015) investigated two types of PVD-coated carbide tools (TiAlN and TiSiN) to determine the mechanism of cutting tool wear and breakage and the effects of tool angle, tool diameter, tool extended length, cutting force and cutting-induced vibration on the tools. The modes of breakage of the coated carbide tools used for the high-speed milling of hardened steel were coating peeling, chipping and tip breakage.

Xue Hongjian et al (1997) created a new concept of shape characteristic detection of tool breakage in milling operations is proposed. The detection of tool breakage is conducted according to the shape characteristics of discrete dyadic wavelet decomposition of cutting force. By means of the proposed method, the influence caused by the variation of cutting parameters and transients is eliminated. The proposed method is conducted in two steps. Cutting force signals are decomposed by discrete dyadic wavelet, with the shape characteristic vectors and after the shape characteristic vectors are fast classified by the ART2 neural networks. The accuracy and effectiveness of the proposed method are verified by numerous experiments.

Y.S. Tarn (1990) is presented a study of the cutting force pulsation due to tool breakage. Monitoring algorithms extracting the cutting force signal changes caused by tool breakage and further processing the extracted cutting force signal to recognize tool breakage are proposed. Theoretical studies and experimental results performed in milling operations have proven the feasibility of the algorithms proposed. In another work (Y.S. Tarn 1991) from the same author, we can read the following. The quasi-mean resultant force has been proven to be very useful for sensing tool breakage in milling. It has been also shown that the quasi-mean resultant force is proportional to the quasi-mean resultant displacement of spindle. Therefore, a system for on-line detection of tool breakage in milling has been developed in this paper by using the difference of the quasi-mean resultant displacement of spindle.

It can be seen from the review of the professional literature that a number of articles deal with the investigation of the breakage of milling tools and the resulting cutting forces. These are mostly dynamic in-cutting tests that aim to predict, among other things, tool breakage through the determination of the resulting cutting forces using analytical calculations and the use of on-line sensors. We have little information about the fracture itself and the formation of cracks that precede it.

The aim of our work is to develop a complex test system where, through the elemental stresses, we induce failures and their pre-failure conditions, the effects of which can be detected by later cutting tests. Our present work seeks to present one segment of this extensive research, through the laboratory fracture test method.

2. Theoretical description of the tests and procedur

First, let's take a schematic look at our planned complex tool failure testing system. (Fig. 3)

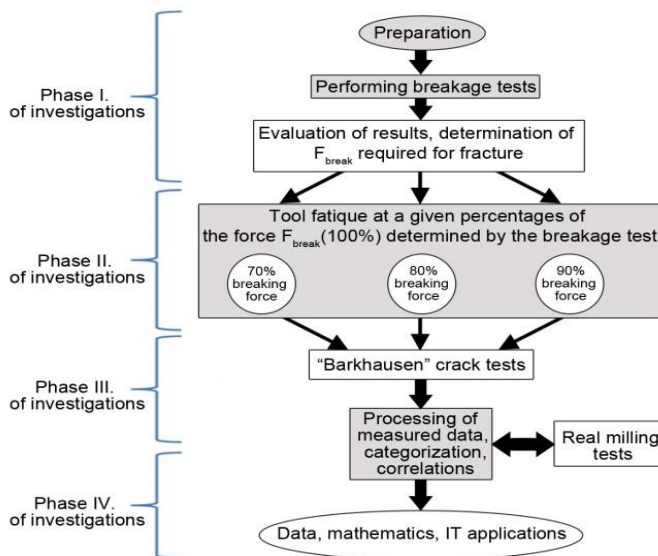


Figure 3. The logical sequence of complex experiment

A brief description of the main steps shown in the figure is as follows:

- Section I: After the preparations, we first determine the $F_{breaking}$ force required to break the tool with static (stationary) fracture tests.
- Section II: Load the tool with a 70-80-90% reduction of the previous $F_{breaking}$ force during rotation on a properly prepared milling (drilling) machine.
- Section III: Next, the tool so fatigued is subjected to Barkhausen tests. The reduction of the breaking force depends to a large extent on the degree of crack formation, if this requires an allocation closer to the breaking force, 95-90-85-80% can also be used. It is important to use uniformly decreasing load allocations.

- Section IV: The processing of the obtained results and their incorporation into the IT database is the final phase of this logical line. In the future, the results of the real cutting tests will be included here.

The results obtained in this way, together with the results of the data taken from industrial production and the preliminary cutting laboratory tests, provide the basis for the future continuation of the research.

Our studies now presented belong to section I. These will form the basis for subsequent fatigue tests, which will be carried out with the help of a “Barkhausen” magnet crack tester.

Development of breakage testing equipment

In the following, let’s review the fracture testing equipment specifically developed for the project. The design of the device was based on the following aspects.

- We need to solve the task using existing equipment.
- The tool clamp must correspond to the actual machine cutting conditions.
- The tool can be rotated outside the fixed position in the clamp.
- We must clearly obtain data on the nature of the fracture (sudden, e.g., exploding or fragmenting, edge cracking) and the degree of breaking force required by drawing a computer diagram continuously during the measurement.

The following schematic diagram shows the arrangement and main parts of the measuring equipment. (Fig. 4)

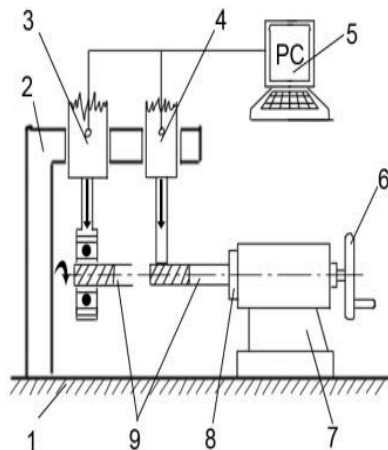


Figure 4. Outline of the breakage test apparatus: 1-stabile base plate, 2- frame (tensile stress tester), 3- pressure head for rotating tool, 4- pressure head for stationary tool, 5- computer measurement software, 6- hand clamp and rotator, 7- clamping milling spindle, 8- morse taper tool holder, 9-milling tools (specimens)

The tool (9) and the pressure heads (3, 4) are located in the rigid frame system (1, 2). The pressure head touches the cutting end of the tool by simulating the depth of grip (2-3-4-5mm). At the tool end, the contact of the pressure head acts in a circular manner on the tool. The easiest way to achieve this is with a bearing ring (3). The design of the tool holder and the tool holder must correspond to real industrial conditions (7, 8). The computer recording the measurement data (5) continuously records the compressive force in a diagram.

In the following, we review the parts of the equipment marked in the sketch.

Stable basic frame measuring unit

A material testing tensile machine forms the framework for the measurement. The tensile machine is located in our material testing laboratory, type Zwick-Roel Z100, with a maximum tensile/compressive force of 100kN.

Tool holder fixing unit, tool holder inserts

The stable gripping of the tool and the provision of the rotation function are ensured by an original milling (vertical) spindle head (type: ME1000 milling machine) with morse (MT)-3 conical connection. A special tool holder has been designed for the vertical head so that the tool can be loaded at the appropriate length and clamped to the desired extent. Figure 5 shows the complete clamping structure and morse cone tool clamp. By turning the wheel mounted on its threaded spindle, the desired position can be set to apply the load.

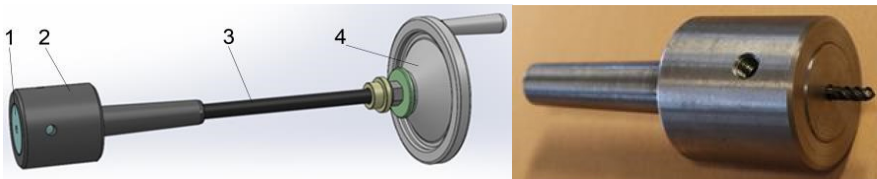


Figure 5. Assembly drawing of the clamping device and the morse conical tool holder, 1- tool holder insert with „Weldon” sleeve, 2- tool holder shank with morse cone, 3- retraction shaft, 4rotating hand wheel

The tool holder shank (2) must ensure a precise fit to the morse-conical spindle sleeve of the milling head and must also be secured axially. It includes a handwheel (4) for fixing and rotating the spindle at one end and a matching hole at the other end to hold the "Weldon" sleeve (1) (three such inserts are required for Ø6, Ø8 and Ø10 tools). The tools are fastened with two M6 screws, the insert is fixed with two M10 screws rotated 90° apart. It is connected to the vertical head with an MK-3 conical clamp. Part 3 is an M12 threaded shank. The test can be performed in two angular positions. This determines whether there is a significant difference depending on the different angular position of the tool.

The tool holder inserts are made of C45R material for adequate strength, however, the brittle material has been avoided to prevent the shank from breaking in the insert. The inserts have a double-sided design, so that if one side expands due to the compressive load, it can be used on the other side (Fig. 6).



Figure 6. The tool holder insert with the fixing holes is made for a tool diameter of 6 mm

Pressure inserts

Two types of pressure inserts used for breakage tests have been developed and are shown in the figure.



Figure 7. Push rod with cylindrical solid and bearing roller end

The simple push rod (figure 7. on the left) creates a tool break in the upright position. This examines the material properties of the tool shank, in addition to the fractures that occur during cutting in such a position, e.g., CNC fast movement. This press was used to test the breaking forces acting eccentrically on each cutting edge.

The press-fit insert with a bearing end (figure on the right) is used for fracture tests during rotation, here a bearing ring (which fits the diameter of the tool under test loads the tool shank during rotation areas of application. (Fig. 8)

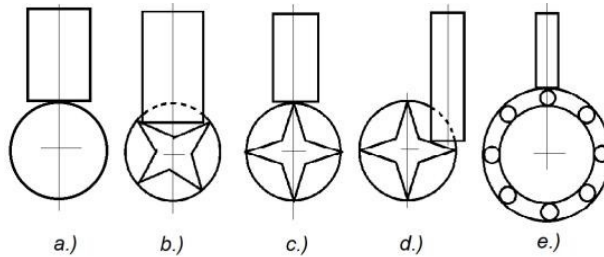


Figure 8. Planned test categories for tool breakage, Solid tool shank break, b.) Tool cutting part loaded on two edges, c.) Tool cutting part loaded on one edge, d.) Tool cutting edge loaded, e.) Tool loaded during rotation

Assembling the device group

The following figure shows the assembled breakage tester. The tensile test machine is used in a pressing function using the appropriate probe fork insert. Below the load beam is the tool holder with the vertical milling head.



Figure 9. Planned Measurement assembly and load zone

The vertical head is mounted on the test bench with two hex head screws. By placing the holes on the test bench, positioning has also been solved.

Procedure of measurement

- Fracture tests were performed on milling tools, which is also represented by the nature of the load. Fracture tests examine the maximum load capacity of different tools against static breaking force. The tools involved in the tests are selected on the basis of the following characteristics:
- tool material

- tool diameter
- number of cutting edges
- according to technology (milling, drilling)

The principle of measurement is as follows, a solid circular steel exerts a radial force on the clamped tool. The value of the breaking force at which the tool breaks is recorded with the help of a computer measuring program. During the measurement, we follow the steps marked in the following flowchart, together with the given remarks (Figure 10.).

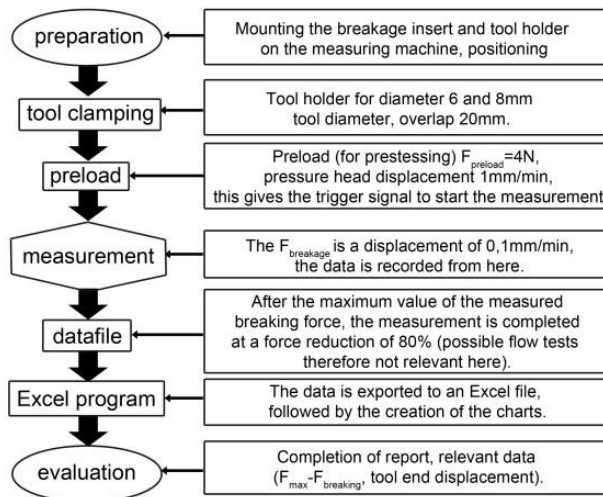


Figure 10. Main steps of the breakage test procedure

3. Equipment validation

The equipment was tested and validated in two parts. First, break the “typical” milling tools and then record the measured data. After that, the 3D modelling of the former milling tool, and then checking this with finite element simulation, is how close the calculated breaking force approaches the result of the real fracture test measured on the equipment.

Breakage test with the developed equipment

In the following, let’s review the real breakage test, milling tool, the test procedure, and the results.

Specimen milling tool of breakage test

The validation fracture test was performed on a Fraisa P5230 Ø6 milling tool (P5230.300 HM MG10 gt) with the following main features (source: Fraisa):

- Fine-grained, carbide homogeneous structure (without internal cooling hole)
- Raw material with a hardness of 1600HV
- Rm tensile strength: 850-1100 MPa
- 6mm tool diameter (shank and working part)
- 3 cutting edges
-

Test procedure, measurement result

The process of the validation test is completely in line with the previous flowchart. The tester increased the load until the tool broke, while measuring the deformation and standard force. The measurement results are shown in the following figure.

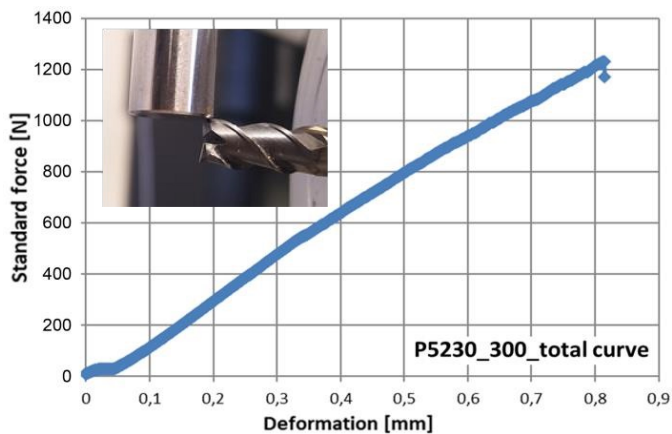


Figure 11. The relationship between deformation and force

The figure 11 shows the complete measurement diagram, in the 0-0.35mm displacement range at the initial stage of the measurement (0-500 measurement data after preloading) and then in the 0.35-0.82mm displacement range at full load (500-1200 measurement data) shows the evolution of the curve up to the fracture. It can be seen that the relationship between the force and the deformation is approximately linear, the fracture occurs at 1234 N, with the magnitude of the deformation is 0.815 mm.

The following figure shows the original condition of the tool and the fracture surface (brittle fracture) after the test. (Fig. 12)



Figure 12. Photos of the tool used for validation measurement (Frais P5230 Ø6) before (left) and after (right) the breakage test

Repetition of breakage test by FEM analysis

Using the possibilities of computer simulations, we create the “opposite pole” of the validation tests for the finite element test, the comparison of which with the real fracture test shows its applicability.

3D CAD model of the tool

For the simulations, a 6-diameter P 5230.300 HM MG10gt milling tool used in real fracture tests was modelled. The modelling was performed with parametric engineering CAD software. The following figure shows the appearance of the 3D model (Fig. 13).

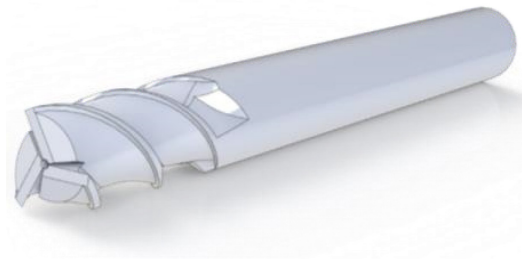


Figure 13. Apparent 3D CAD image of the tool model (based on Fraisa P5320 Ø6)

For the volumetric body model, we also considered the tool edge characteristics, chamfers, and angles.

FEM simulation breakage tests

The aim is to determine whether the simulation programs give adequate results for radial loads. Furthermore, to create a method to determine the critical value that the tool can still handle and to compare this value with the result of the actual test. Given the results obtained, a conclusion must be drawn and the suitability of the method determined.

The simulation was performed with Ansys® Academic Research Mechanical, Release 17.2 with the Static Structural module. The following aspects were kept in mind during the simulation:

- The clamping is made on the shank with a fixed grip, as the grip takes all six degrees of freedom, so this grip is correct.
- Clamping will take place in two lengths.
- The load is applied to the cutting edge for a length of 6 mm.
- The load is applied to one or two corresponding surfaces.
- The voltage drop caused by sharp edges does not matter during the simulation.

The carbide has a hardness of approximately 90 HRA (Pintér 2018) with a yield strength of approximately 1000 MPa. Therefore, the force at which such a load is applied to the tool is recorded. (Fenyvessy 2015)

In determining the value sought, if the voltage exceeds the yield point due to the force, it will be lower in the next simulation, if it does not exceed, and vice versa.

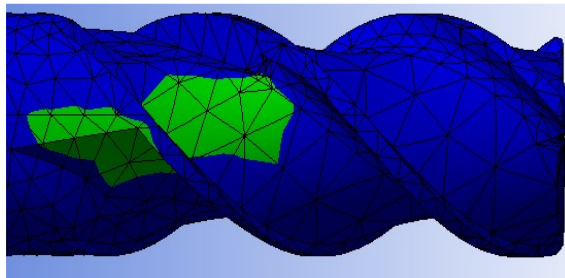
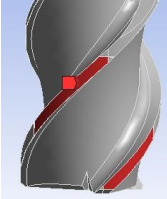
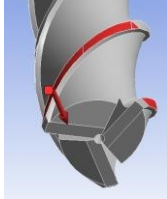
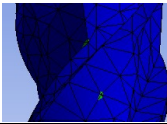
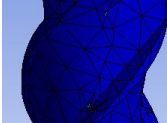
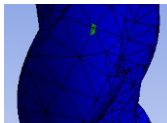


Figure 14. The simulated fracture

Figure 14 shows how the stress in the green area reached the yield point and thus a fracture would occur. Both the simulation and the examined broken tool showed a brittle fracture. In the following, we look at the results obtained from the simulations in tabular form (Table 1).

Table 1. Simulation results of Fraisa P5320 Ø6 fracture at different clamping lengths

| Tool type | 1 tool edge vertically | 2 tool edges |
|-----------------------|---|---|
| Load |  |  |
| 30 mm clamping length |  |  |
| Required strength | 1100 N | 1100 N |
| 40 mm clamping length |  |  |
| Required strength | 1050 N | 1050 N |

The images in the table illustrate the achievement of the yield strength. This appeared at the top third of the cutting part of the tools, so those parts were enlarged in the pictures. The complete tools and the stresses that arise in them are shown below.

It can be seen from these simulations that it gives nearly the same result regardless of rotation and clamping. The presented structure can be applied on a theoretical basis to find the force at which the plastic deformation occurs. For reliability, compare the real and simulated fracture test values in the following.

4. Discussion, comparison of real and simulated breakage test

Clamping and loading are similar to a real fracture test. On the short surface “A” the force is applied, while on the surface “B” the tool is gripped, tying all six degrees of freedom. (Figure 15.)

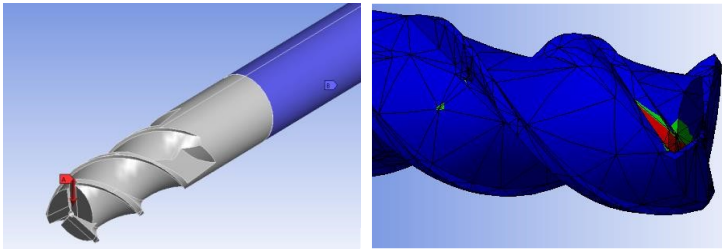


Figure 15. Structure of comparative simulation and plastic deformation

Excluding the high stress due to the sharp corners of the cutting edges, 800 N is required to reach 1000 MPa according to the simulation. Under a force of 1200 N, the deformation develops as shown in the following figure, in millimeters.

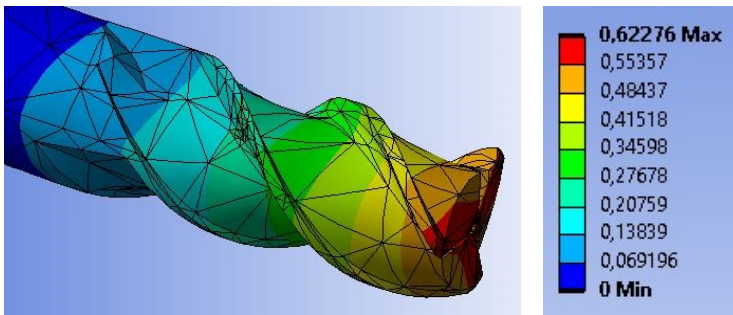


Figure 16. Comparative simulation and deformation

The following figure shows a sectional view of the stress distribution, and since the yield strength on the inner parts is already significantly lower, a brittle fracture is conceivable, values are in MPa.

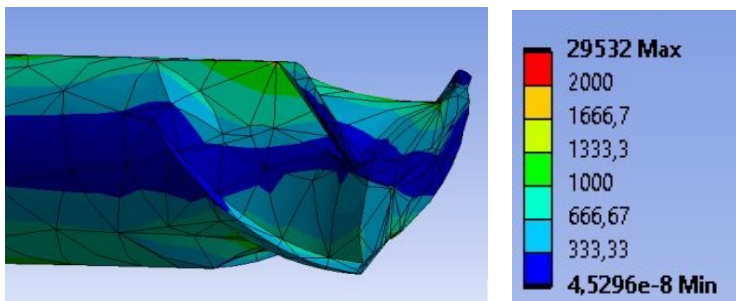


Figure 17. Comparative simulation and distribution of strength

5. Conclusion

The results showed that the simulation programs can be properly used to develop a predictive tool breakage prediction system. The extent of the deviations is commensurate with the current capabilities of the simulation programs.

The FEM method showed less value in the deformation, but this can also be explained by the fact that other elements of the device performing the test are also deformed (vertical head, clamping elements), therefore it shows a higher value than shown in the simulation.

Determining the load values is not an easy task for this type of brittle fracture, however, it was visible how the whole cross-section slowly underwent plastic deformation.

Because the predictive method deviates in the direction of safety and shows the onset of plastic deformation at 2/3 of the true fracture value, it provides an acceptable result.

Overall, it can be stated that the simulation can provide a support corresponding to the breaking point of the tools. It cannot be determined with full certainty at present, but it can provide a safe limit that is of great help in determining the cutting parameters. The interaction of the laboratory test method and the finite element simulations performed in parallel show a favourable opportunity for our further investigations.

The long-term goal of the studies is to determine sub-data for a larger, more complex task, to develop predictive tool failure prediction systems.

Acknowledgement

Our work was supported by the 2018-1.3.1-VKE-2018-00041 “*Intelligens, prediktív szerszámfelügyeleti eljárások kidolgozására és rendszer kialakítására, valamint a fejlesztés fenntartására alkalmas kutatási együttműködés létrehozása*” project and we would like to express our special thanks.

References

- [1] Albrecht, S. S. Park, Y. Altintas, G. Pritschow: High frequency bandwidth cutting force measurement in milling using capacitance displacement sensors, *International Journal of Machine Tools and Manufacture*, vol. 45., 2004
- [2] Kaya, C. Oysu, H. M. Ertunc: Force-torque based on-line tool wear estimation system for CNC milling of Inconel 718 using neural networks, *Advances in Engineering Software*, vol. 42., 2011
- [3] Y. Wang, Y.X. Xie, Z. Qin, H.S. Lin, Y.H. Yuan, Q.M. Wang: Wear and breakage of TiAlN- and TiSiN-coated carbide tools during high-speed milling of hardened steel, *Wear*, Volumes 336–337, 15 August 2015, Pages 29-42
- [4] Dr. Pintér József: Forgácsoló megmunkálás (Forgácsolás és szerszámai) Szerszám anyagok (élműanyagok, szerszám bevonatok), NGB_AJ012_1, 2018
- [5] F. Dömötör: Összetett szerkezetű járműanyagok (hibridek, kompozitok) határfelületei megmunkálási folyamatainak korszerű technológiai diagnosztikája, Doctoral dissertation, 2013
- [6] J. H. Kim, H. K. Chang, D. C. Han, D. Y. Jang, S. I. Oh: Cutting Force Estimation by Measuring Spindle Displacement in Milling Process, *CIRP Annals*, vol. 54., 2005
- [7] J. Luo, H. Ding, A. J. Shih: Induction-heated tool machining of elastomers—part 2: chip morphology, cutting forces, and machined surfaces, *Machining Science and Technology, An International Journal*, vol. 9., 2007
- [8] J. Wang, P. Wang, and R. X. Gao: Tool life prediction for sustainable manufacturing, 2013
- [9] M. Postel, D. Aslan, K. Wegener, Y. Altintas: Monitoring of vibrations and cutting forces with spindle mounted vibration sensors, *CIRP Annals - Manufacturing Technology*, vol. 68., 2019
- [10] S. N. Phokobye, I. A. Daniyan, I. Tlhabadira, L. Masu, L. R. Van Staden: Model Design and Optimization of Carbide Milling Cutter for Milling Operation of M200 Tool Steel, *Procedia CIRP*, vol. 84., 2019
- [11] T. Fenyvessy, R. Fuchs, M. C. Gütler és A. Plósz: Műszaki Táblázatok, Budapest: TCS Media Kft., 2015.
- [12] V. Zablotskyi, O. Dahnyuk, S. Prystupa, A. Tkachuk: Formation of Physical and Mechanical Properties of Surface Layer of Machine Parts, *Mechanics, Materials Science & Engineering*, 2017
- [13] Xue Hongjian, Yang Kechong, Yang Rong: The shape characteristic detection of tool breakage in milling operations, *International Journal of Machine Tools and Manufacture*, Volume 37, Issue 11, November 1997, Pages 1651-1660
- [14] Y. Altintas, I. Yellowley, J. Tlusty: The Detection of Tool Breakage in Milling Operations, *J. Eng. Ind.* Aug 1988, 110(3): 271-277

- [15] Y. Altintas, S. S. Park: Dynamic Compensation of Spindle-Integrated Force Sensors, CIRP Annals, vol. 53., 2004
- [16] Y.S.Tarn: On-line detection of tool breakage in milling, Mechanical Systems and Signal Processing, Volume 5, Issue 5, September 1991, Pages 389-401
- [17] Y.S.Tarn: Study of milling cutting force pulsation applied to the detection of tool breakage, International Journal of Machine Tools and Manufacture, Volume 30, Issue 4, 1990, Pages 651-660
- [18] Yao-Wen Hsueh, Chan-YunYang: Tool breakage diagnosis in face milling by support vector machine, Journal of Materials Processing Technology, Volume 209, Issue 1, 1 January 2009, Pages 145-152
- [19] <https://www.fraisa.com/en/assets/media/pdf/kataloge/en/FRAISA-end-millingtools-2014.pdf>. [Access date:16 04 2020]
- [20] <https://www.kistler.com/en/> [Access date:16 04 2020]
- <https://www.sandvik.coromant.com/> [Access date:16 05 2021]

Analyzing the mechanical properties of bio photopolymer-composite test specimens

Adrián BOGNÁR¹, Krisztián KUN², László ZSIDAI³

¹*Doctoral School of Mechanical Engineering, MATE, Gödöllő*

²*Department of Innovative Vehicles and Materials, NJE, Kecskemét*

³*Department of Materials Science and Engineering Processes, Institute of Technology, MATE, Gödöllő*

Abstract:

In this study, an organically modified montmorillonite (OMMT), was added to the Stereolithography (SLA) resin. The test specimens were made using a custom stereolithographic 3D printer and the mechanical properties of the printed specimens were investigated. The effect of the filler on printing accuracy was also measured and evaluated. The results showed that the addition of OMMT at 5% (w/w) decreased the flexural modulus and the maximal flexural stress by 37%.

Keywords:

DLP, SLA, composite, montmorillonite, resin, photopolymerization

Introduction

Rapid prototyping, particularly SLA 3D printing, has undergone significant advancements due to developments in material science. Traditional 355 nm SLA printers are expensive due to specialized laser equipment and the photoinitiators used, while 405 nm desktop Digital Light Processing (DLP) systems offer a more affordable alternative but often exhibit inadequate mechanical properties. To address this issue, researchers are exploring nanocomposites as reinforcing materials. This study examines the effect of organic montmorillonite nanoparticles on the mechanical properties of test specimens produced from DLP resin. The results highlight how the incorporation of OMMT nanoparticles influences the mechanical characteristics of printed products (Weng, 2016), (Palucci Rosa, 2021).

Experimental

The temperature of the resin and the printer chamber is one of the most significant factors during the experiment, as it affects viscosity by decreasing it, allowing the material to flow more easily within the resin vat and improve printability. The effect of temperature is particularly important not only during the printing of pure photopolymer resin but also in the mixing process and the printing of photopolymer composite materials. The appropriate temperature range for dispersion depends on the reinforcing material. In such cases, it is advisable to use a material with a similar or identical density because a heavier material will quickly sink into a lower-viscosity liquid, leading to an inhomogeneous material distribution during printing. This promotes the formation of stress concentration points, uneven load distribution, and ultimately the fracture of the final product. In terms of its effect on the chemical structure, higher temperatures increase the mobility of free radicals and polymers, which enhances the photopolymerization processes and leads to a higher conversion of cross-links (Bagheri, 2019).

Photopolymer resin

Photopolymers are resins that change their structural and chemical properties through photochemical reactions when the exposed light leads to crosslinking. They consist of a mixture of highly crosslinkable monomers, oligomers, and light-sensitive photoinitiators. The illumination is usually done with ultraviolet (UV) light, although it can extend into the visible spectrum. As a result, their structural properties can be altered under UV light exposure. Oligomers are molecules made up of a limited number of monomer units, enabling the formation of branched chain molecules. Thanks to the branching, the crosslinking grows in all directions in space. The material used in the experiments is skin-colored Voxeltek Pro resin, for which the manufacturer did not provide a Technical Datasheet.

As a result, we referred to the processing parameters of a similar resin with comparable properties, as recommended by the printer manufacturer (Bagheri, 2019), (Voxeltek, online).

Organic filler material

Organically modified montmorillonite (OMMT) is utilized as a reinforcing agent due to its unique ability to enhance the mechanical and thermal properties of materials. When incorporated into resins, OMMT can improve strength, stiffness, and heat resistance. This is primarily attributed to its layered structure, which allows for more even dispersion within the polymer matrix, potentially leading to better interactions between the resin and the reinforcement. Nanomer I.30P (Table 1.), a high-purity montmorillonite treated with Octadecyl-

Ammonium ($C_{18}H_{37}NH_3^+$). This organic compound used to modify the surface of montmorillonite clays like Nanomer I.30P. By attaching Octadecyl-Ammonium groups, the polarity of the materials surface is reduced, making it more compatible with apolar polymers. This can improve dispersion and may provide stronger mechanical reinforcement in the polymer matrix (Nanomer I.30P, online source), (Tarablsi, 2012), (Bata, 2024).

Table 1. General data of Nanomer I.30P (Nanomer I.30P, online source)

| | |
|--|-------------------------------|
| Surface Modifier | Octadecyl-Ammonium |
| Appearance | Off white free flowing powder |
| Surface Modifier Concentration | 28-32 wt% |
| Bulky Density | 250-300 kg/m ³ |
| Particle Size (Mean) | 15-20 μm |
| Specific Gravity | 1.9 g/cm ³ |
| X-ray diffraction (d₀₀₁) | 18-22 Å |

The surface treatment improves compatibility with the resin, allowing it to function as an effective additive for enhancing physical performance and flame resistance. However, the interaction between the resin and Nanomer I.30P has not been previously studied, and the effects of heating have not been considered. Now it is expected that the resin will incorporate well with the treated nanoparticles to potentially improve its properties. Nanomer I.30P is typically used in concentrations ranging from 4-6 wt% for mechanical improvements, and 1-4 wt% for flame retardancy (Nanomer I.30P, online source).

Custom 3D printer setup

The printing was performed on a Phrozen Sonic Mighty 8K DLP printer (Fig. 1.). This type of printer does not have a built-in heating unit to control the chamber temperature, so this was achieved using a custom heating system described in a previous study. This heating device must be capable of maintaining a stable resin temperature of 40°C. Heating the photopolymer resin is necessary to reduce its viscosity, ensuring better flow properties and more uniform layer formation during printing. This helps improve the overall print quality and may enhance the dispersion of any added reinforcing materials. The selected resin temperature values were determined based on previously reviewed studies, which highlight the benefits of heating (Frank, 2022), (Dall'Argine, 2020), (Steyrer, 2018).

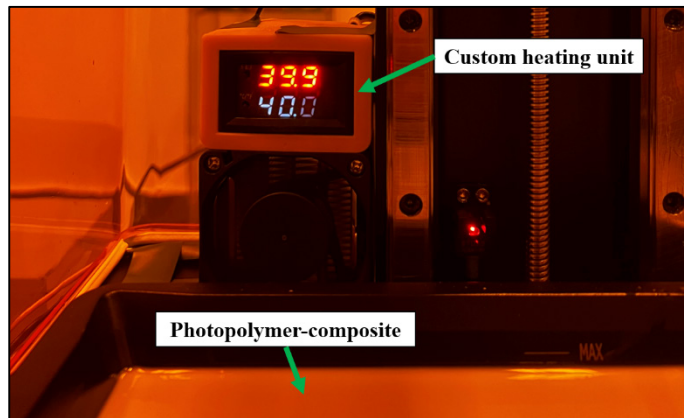


Figure 1. The custom heating unit inside the chamber and set to 40°C

Preparation of photopolymer-composite material

Magnetic stirring (Fig. 2.) is a low-cost mixing method, where a small magnet is used for mixing the particles, achieved through high-speed rotational movement. While it is simple and cost-effective, the mixing efficiency is not very high with this method. Despite this limitation, magnetic stirring is still suitable for mixing materials with larger particle sizes, similar to manual mixing. However, for optimal dispersion, especially of nanomaterials, an ultrasonic homogenizer can be used to improve material preparation. Mixing over a wider temperature range can also help enhance dispersion.

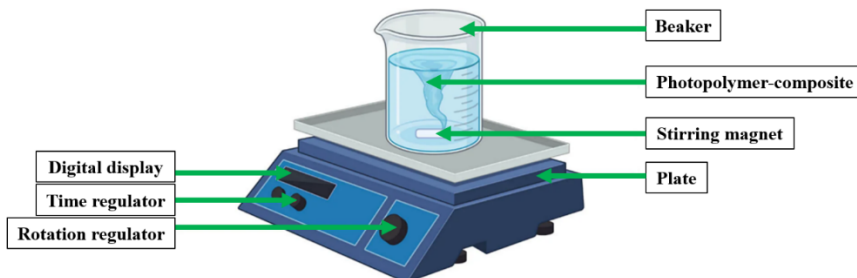


Figure 2. Parts of the magnetic stirring machine (Magnetic Stirrer, online source)

The filler material required for printing was measured using a Kern ABT 120-5DM laboratory scale. Two types of resin were prepared for the experiment: a pure resin and a resin containing 5% wt% OMMT. The OMMT was mixed into the resin to investigate its effects on the material's properties. A 5% wt%

concentration was chosen based on the Nanomer I.30P datasheet and previous studies, as well as its potential to enhance the resin's performance without negatively impacting its overall characteristics. Before mixing, the resin was heated up to 40°C using an industrial polymer drying oven. The pre-heating of the resin before mixing was prompted by the OMMT's tendency to form lumps. When the resin was at room temperature, the results were unsatisfying, as the resin aggregated into larger lumps at the bottom of the photopolymer vat during preliminary test (Fig. 3.) (Nanomer I.30P, online source).

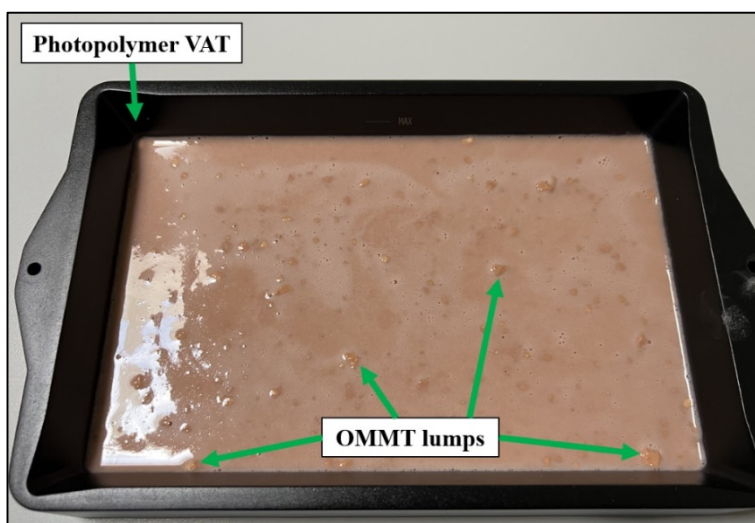


Figure 3. Inconsistent dispersion of the reinforcement material in the photopolymer resin

3D printing process

A total of 18 bending test specimens were printed: 9 pieces from the pure resin with 0 wt% OMMT, and 9 pieces from the resin containing 5% wt% OMMT (Fig. 4.). The dimensions of the test specimens were 53×10×3 mm, following the MSZ EN ISO 178 standard for plastic three-point bending test specimens. No other factors were modified in the slicer or during the printing process, all manufacturing settings were left at the recommended value mentioned in the 2.1 section.

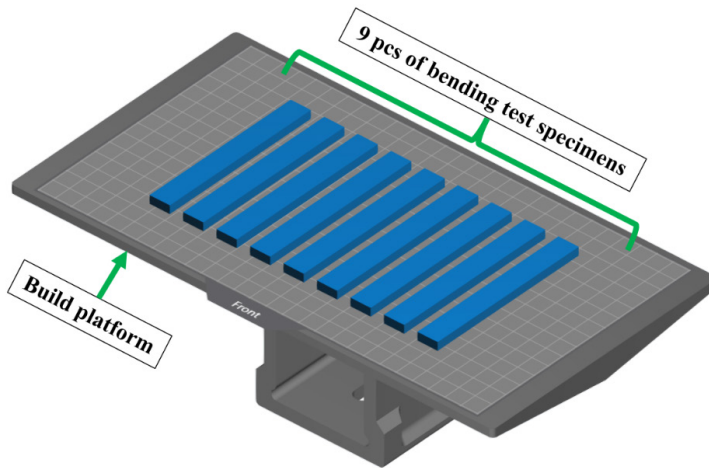


Figure 4. Specimen layout on the build platform (ChituBox Slicer Software, online source)

Table 2. contains printing parameters based on the Phrozen Sonic Mighty 8K official printing profiles that were applied identically in both experiments. In the present experiment, the specimens were not post-cured, only cleaned with isopropyl alcohol. With these printing settings, the printing of a set of 9 specimens took 25 minutes.

Table 2. Resin printing parameters (Prozen Resin Profile, online source)

| | | |
|------------------------------|--------------------------------|--------------|
| Basic info | Layer height | 0.05 |
| | Retract speed (mm/min) | 150 |
| Bottom Layers | Layer count | 6 |
| | Exposure time (s) | 35 |
| | Lifting distance (mm) | 8 |
| | Lifting speed (mm/min) | 60 |
| Transition layers | Layer Count | 6 |
| | Exposure time (s) | 2.3 |
| Normal layers | Lifting distance (mm) | 8 |
| | Lifting speed (mm/min) | 60 |
| Waiting mode during printing | Mode | Resting time |
| | Rest time after retract | 2 |

Three-point bending flexural test

During the three-point bending test, the printed prismatic specimens were subjected to a simply supported loading configuration with a central concentrated force. The specimens were supported at two points from below, while the load was applied at a single point from above. The reaction force was recorded at the specimens midpoint as a function of deflection. Based on the applied force and the corresponding deflection, the flexural deformation behavior of the specimens was analyzed. For data evaluation, the determination of the flexural modulus and the flexural strength was required. The bending tests were performed using an Instron 3366 universal testing machine (Fig. 5).

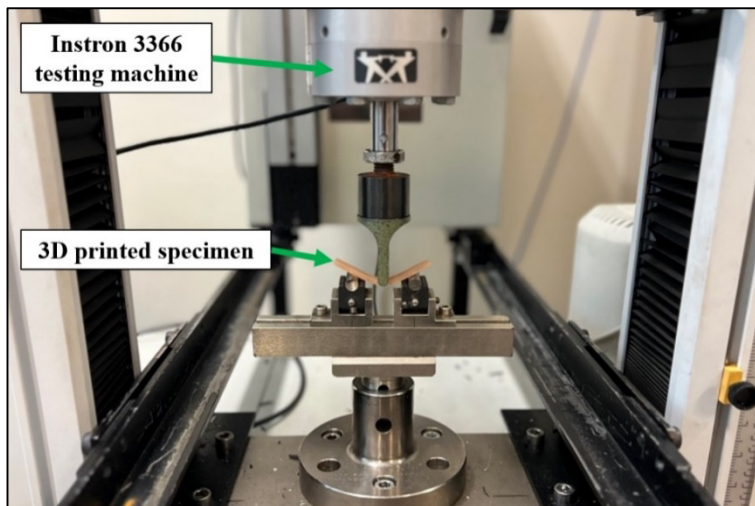


Figure 5. Three-point bending flexural test

Each specimen was placed on the support rollers with the surface that was not in contact with the build platform facing downward. The support span was set to 48 mm using a caliper, considering the specimens thickness (16x3 mm) and following the MSZ EN ISO 178 standard. The bending test was conducted either until specimen fracture or until a predefined deflection limit was reached. In this study, the maximum deflection was set to 11 mm. This value was determined based on three preliminary tests. Table 3. contains the most important settings for bending, configured in the Bluehill 2 software.

Table 3. Three-point bending settings of the measurement software

| | |
|--------------------------------------|-----------------------------|
| Standard | MSZ EN ISO 178 |
| Force measurement range | 10 kN |
| Displacement measurement type | Crosshead displacement |
| Sampling rate | 100 ms |
| Crosshead speed | 20 mm/min |
| Fixture type | Three-point bending fixture |
| Support span | 48 mm |
| Preload | 1 N |
| Preload speed | 10 mm/min |
| Maximum deflection value | 11 mm |

Results and conclusion

The results of the three-point bending tests are recorded in Table 4.

Table 4. Three-point bending test results

| Pure specimen | Flexural modulus (MPa) | Maximum load (N) | Maximum flexural stress (MPa) | OMMT reinforced specimen | Flexural modulus (MPa) | Maximum load (N) | Maximum flexural stress (MPa) |
|-----------------------|------------------------|------------------|-------------------------------|--------------------------|------------------------|------------------|-------------------------------|
| #1 | 4406 | 183.35 | 146.68 | #1 | 2548 | 115.44 | 92.36 |
| #2 | 4199 | 179.19 | 143.35 | #2 | 2551 | 118.86 | 95.09 |
| #3 | 3929 | 154.54 | 123.63 | #3 | 2693 | 115.88 | 92.70 |
| #4 | 4389 | 183.82 | 147.06 | #4 | 2688 | 114.14 | 91.31 |
| #5 | 3987 | 168.66 | 134.93 | #5 | 2732 | 115.63 | 92.50 |
| #6 | 4039 | 170.82 | 136.66 | #6 | 2902 | 105.28 | 84.23 |
| #7 | 3808 | 162.70 | 130.16 | #7 | 2644 | 116.05 | 92.84 |
| #8 | 3815 | 162.26 | 129.81 | #8 | 1508 | 77.96 | 62.37 |
| #9 | 3958 | 169.54 | 135.64 | #9 | 2765 | 115.63 | 92.51 |
| Average values | 4058,89 | 170,54 | 136,44 | Average values | 2559 | 110,54 | 87,60 |

In tensile testing, an increase in reinforcement content generally leads to improved mechanical properties up to a certain concentration. However, in flexural testing, this trend does not necessarily hold, particularly if the reinforcement does not integrate effectively with the polymer matrix. In the present study, the decrease in flexural properties can be attributed to the insufficient interaction between the surface-treated OMMT and the resin (Fig. 6.).

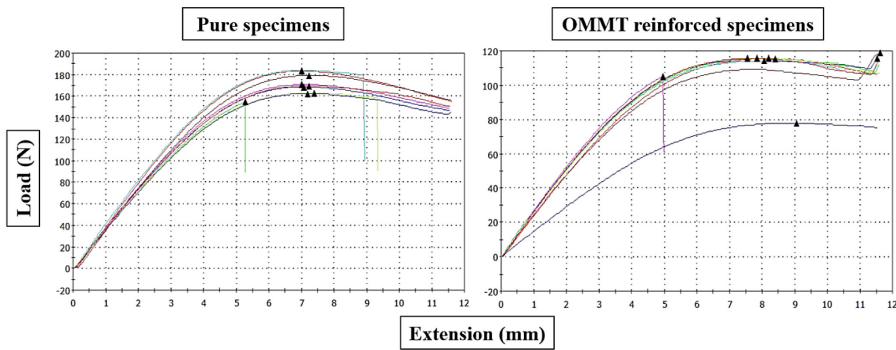


Figure 6. Pure specimens (left) and OMMT reinforced specimens (right) load-extension graphs

The underlying reason for this is the difference in polarity: OMMT, modified with octadecyl ammonium, exhibits improved compatibility with certain polymer systems. However, in this case, the specific photopolymer resin did not establish a sufficiently strong interaction with the OMMT particles after mixing. The likely explanation is that the resin predominantly exhibits non-polar characteristics, while the surface treatment of OMMT aims to enhance dispersion rather than to ensure strong chemical bonding with non-polar resins. Consequently, the reinforcement did not integrate effectively, limiting its ability to enhance the flexural performance. Additionally, further investigation into the photopolymer resin itself is necessary to better understand its matrix characteristics, particularly in terms of polarity and compatibility with OMMT.

This would allow for selecting or modifying the resin to achieve improved dispersion and interaction with the reinforcement. Moreover, the mixing process plays a crucial role in the final dispersion of OMMT within the resin. Inadequate mixing can lead to agglomeration, preventing the reinforcement from being evenly distributed, which negatively affects mechanical performance. Therefore, optimizing the mixing parameters, including mixing time, speed, and method, is essential to improve homogeneity. Temperature control is another critical factor, as the viscosity of the resin changes with temperature, influencing the dispersion of OMMT. Maintaining an appropriate temperature during mixing and printing could enhance the distribution of the reinforcement, preventing sedimentation or

uneven dispersion. Future studies should focus on these aspects to develop a more effective approach for incorporating OMMT into photopolymer resins.

REFERENCES

- [1] Weng, Z., Zhou, Y., Lin, W., Senthil, T., & Wu, L. (2016). Structure-property relationship of nano enhanced stereolithography resin for desktop SLA 3D printer. *Composites Part A: Applied Science and Manufacturing*, 88, 234-242.
- [2] Palucci Rosa, R., & Rosace, G. (2021). Nanomaterials for 3D printing of polymers via stereolithography: Concept, technologies, and applications. *Macromolecular Materials and Engineering*, 306(10), 2100345.
- [3] Bagheri, A., & Jin, J. (2019). Photopolymerization in 3D printing. *ACS Applied Polymer Materials*, 1(4), 593-611.
- [4] Voxeltek Pro Resin (last viewed on: 28.02.2025):
- [5] Online source: <https://hu.voxeltek.com/>
- [6] Nanomer I.30P Technical Datasheet (last viewed on: 28.02.2025):
- [7] Online source: <http://east8west.com/data/Nanocor-product-I.30P.pdf>
- [8] Tarablsi, B., Delaite, C., Brendle, J., & Croutxe-Barghorn, C. (2012). Maghemite intercalated montmorillonite as new nanofillers for photopolymers. *Nanomaterials*, 2(4), 413-427.
- [9] Bata, A., Gerse, P., Slezák, E., & Ronkay, F. (2024). Time- and temperature-dependent mechanical and rheological behaviours of injection moulded biodegradable organoclay nanocomposites. *Advanced Industrial and Engineering Polymer Research*, 7(4), 482-496.
- [10] Frank, C., Hager, K., Csizmadia, R., Kury, M., & Gorsche, C. (2022). Hot Lithography-High precision 3D printing of flame-retardant photopolymers for the electronics industry.
- [11] Dall'Argine, C., Hochwallner, A., Klikovits, N., Liska, R., Stampf, J., & Sangermano, M. (2020). Hot-Lithography SLA-3D Printing of Epoxy Resin. *Macromolecular Materials and Engineering*, 305(10), 2000325.
- [12] Steyrer, B., Buseti, B., Harakály, G., Liska, R., & Stampfl, J. (2018). Hot Lithography vs. room temperature DLP 3D-printing of a dimethacrylate. *Additive Manufacturing*, 21, 209-214.
- [13] Magnetic Stirrer- Principle, Parts, Types, Uses, Examples (last viewed on: 28.02.2025):
- [14] Online source: <https://microbenotes.com/magnetic-stirrer-principle-parts-types-uses-examples/>
- [15] ChituBox SLA/DLP/LCD 3D Slicer Software (last viewed on: 28.02.2025):
- [16] Online source: <https://www.chitubox.com/en/index>
- [17] Prozen Resin Profile (last viewed on: 28.02.2025):
- [18] Online source: <https://phrozen3d.com/pages/resin-profile>

Cradle-to-Cradle LCA for circular bio-based plastics: a systemic framework for closed-loop material use

Rihem JEBALI¹, Nejmaddine LAYEB¹, László ZSIDAI²

¹*Doctoral School of Mechanical Engineering, MATE, Gödöllő*

²*Department of Machine Construction, Institute of Technology, MATE, Gödöllő*

Abstract:

The growing environmental strain of conventional plastics has prompted the search for sustainable alternatives, and bio-based plastics have emerged as promising substitutes. In this article, an integrative Cradle-to-Cradle (C2C) Life Cycle Assessment (LCA) framework is introduced as a design for circular bio-based plastics. Building upon conventional linear LCA, which often fails to account for regenerative use phases, the proposed approach focuses on biological and technical nutrient cycles to achieve a closed material flow loop. The paper discusses design principles, systemic considerations, and application challenges of circular LCA, considering product design, infrastructure, and policy directions in general. By incorporating C2C thinking into LCA and design processes, this framework aims to transform bioplastics from single-use products to regenerative assets in a circular economy. Key findings from existing literature, industry practice, and material science inform the feasibility and usefulness of the model in guiding future sustainable material systems.

Keywords:

Bioplastics, Life cycle assessment, Recycling, Circular economy

Introduction

Environmental concerns over plastic waste and dwindling fossil fuel supplies have led to growing interest in green alternatives to traditional petroleum-based plastics. [1] In this context, bioplastics produced from renewable biomass, and in many cases biodegradable, have emerged as the solution of choice. In recent years, the scientific community has been studying the potential environmental benefits of bioplastics through life cycle assessment (LCA) approaches that assess the impacts of manufacturing, use, and end-of-life phases. [2] [3]

Sustainability has become the core requirement in engineering and design.[4] It requires rethinking the design, manufacture and disposal of products, infrastructures and industrial systems. In doing so, green engineering has

developed as a discipline that seeks to minimize environmental damage while maximizing social and economic gains. It advocates for the development of systems that conserve energy, minimize waste, and utilize renewable materials.

But while many traditional approaches to sustainability are designed to reduce the negative impacts of human activity, this mindset can fall short of the necessary radical transformation in a limited and fragile system.

The Cradle to Cradle (C2C) philosophy is built on a dream in which everything we make doesn't end up in the bin but is used to create something new. William McDonough and Michael Braungart first coined the term, which turns the traditional linear idea of 'take, make and throw away' on its head. Instead, it calls for a biological and technical metabolism system in which waste is a resource.[5] In C2C thinking, materials are seen as nutrients in a closed cycle, either safely returned to nature or reused in industrial cycles. This approach encourages the design of materials and products that promote regeneration, reduce waste, and create value in each use.[6] For example, composting industrial products, where everything has a second (or third, or fourth) productive life.

The introduction of this approach to plastics looks promising. Plastics are both a blessing and a curse in today's world. They are strong, light, and versatile, but it is notoriously difficult to dispose of them in an environmentally friendly way. An economic system known as the "circular economy" seeks to eliminate waste and promote product reuse. In this system, plastics are no longer disposable waste, but valuable goods that must go through several life cycles. [7] Circular approaches to plastics aim to redesign products, make them more recyclable, and create systems where they can be reused. Governments and companies, ranging from car parts to packaging, are rethinking how plastics can be part of the cycle of materials, rather than being incinerated. [8]

Bioplastics

Bioplastics produced from renewable biomass sources such as corn starch, sugar cane, or cellulose have a lower carbon content than petrochemical plastics and are changing the face of green growth. The important thing is not where the plastic comes from, but where it goes.

Bioplastics, as classified in **Figure 1**, can be composted, recycled, or reused in high-value applications if they are manufactured according to C2C design principles. Depending on their technical design, they can be integrated into biological or technical cycles. The goal is to produce biodegradable or recyclable materials that can be both recycled and regenerated. [9]

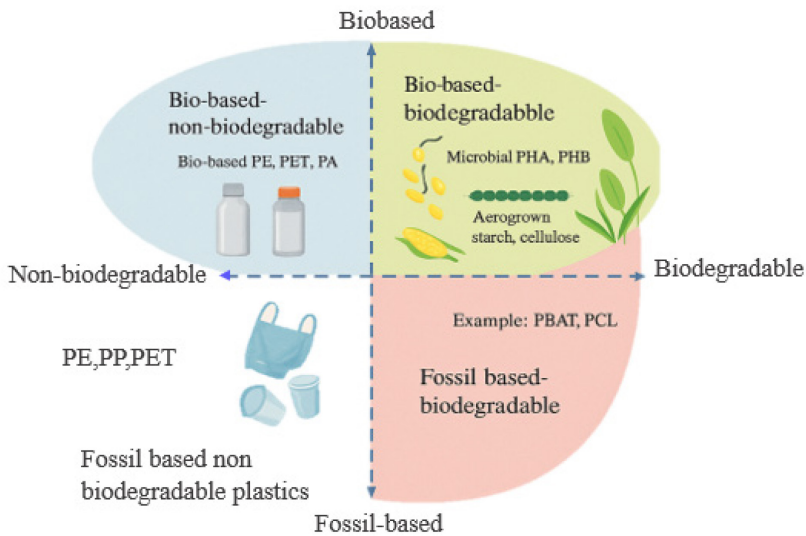


Figure 1: Main three categories of bioplastics. Adapted from (Muneer et al. 2021)

Life Cycle Assessment

Traditional LCA vs. Cradle-to-Cradle LCA

Life Cycle Assessment (LCA) has been around for centuries as a method of measuring the environmental impact of products from raw material extraction to until scrapping. The traditional LCA models, however, tend towards being linear in their approach and having no mechanism for accounting for circular system complexities. An example is a traditional LCA, which will measure the impact of plastic bottles until they are dumped and not account for reuse and recycling. [10]

This is where 'cradle-to-cradle' LCA comes into the picture, which is an even more circular and integrated form of LCA that looks at material in a continuous loop.

Cradle to Cradle LCA considers multiple life cycles of a material rather than a single 'end of life' since material flows are dynamic and continuous in a real-world system.

This approach evaluates how materials transform across the stages of production, use, and regeneration, emphasizing the importance of designing products from the outset with recyclability, compostability and reintegration into either biological or technical cycles in mind. [11]

Systemic LCA for Circular Materials

A systemic LCA redirects focus from individual product evaluations to interrelated systems. It is about combining all types of information:

environmental impacts, economic compromises, social consequences, and technical interdependencies. It's not the footprint of the product, it's the handprint, or it's the net positive contribution to the circular system. It's that bigger picture that makes systemic LCA such a powerful tool for companies seeking to be in alignment with circular economy goals. [12]

Challenges in Implementing Circular LCAs

The shift from conventional LCA towards systemic LCA, cradle-to-cradle, is not problem-free. In the first place, data availability is a concern. Circular systems are rich in complexity and need cross-sector, real-time data. Then, there is the issue of modelling closed-loop cases: how to forecast the environmental footprint of a material that will be reused three times within the same situation?

Another is the standardization, like relative to traditional LCAs, which are formulated from more refined guidelines (e.g., ISO 14040/44), circular LCAs have no standardized protocols yet. This makes calibration and comparison difficult. Finally, there must be experts on board who are acquainted with the science and systems approach of circular appraisal. Without expertise on these grounds, even well-designed tools don't work. [13]

Closed Loop Material Systems in Circular Bio-Based Plastics

Closed Loop System

A closed-loop system is a sustainable model designed to keep materials continuously circulating within a production cycle, minimizing waste and the need for new resources. [14] In this system, products are designed from the start for reuse, recycling, or safe reintegration into the environment. Rather than following the traditional linear path of "take, make, dispose," a closed-loop approach ensures that materials retain their value through multiple lifecycles. This concept is especially vital in addressing environmental challenges, as it promotes efficiency, reduces pollution, and supports the transition to a circular economy. [15]. When applied to bio-based plastics, closed-loop systems aim to recover and reuse the same material in the same or similar applications, ensuring zero waste and maximum value retention. Unlike open or cascading loops, where materials eventually lose functionality, closed loops are designed to be perpetual. Think of it like pressing the "reset" button every time a product reaches the end of its use. [16]

This concept is foundational to circular economy principle. It minimizes the need for virgin material extraction, drastically reduces emissions, and creates more stable, local supply chains. For bio-based plastics, which are already more sustainable than petroleum-based plastics, closed loops push the sustainability bar even higher.

Designing Bio-Based Plastics for Closed Loop Recycling

The design phase is where the closed loop potential is created or destroyed. For a bio-based plastic product to be maintained within a closed loop, it will have to be designed for durability, traceability, and ease of disassembly. This is where Cradle-to-Cradle design principles shine. [17]

For instance, bio-based PET (polyethylene terephthalate) bottles can be designed to retain the same chemical properties as conventional PET so that they are recyclable in existing recycling systems. But that is not all: additives must be non-toxic, coloring must be recyclable, and labels must be removable. Each design decision matters [18],[19]. Emerging technologies also allow molecular marking very tiny invisible markers embedded in plastics to identify the polymer type, use history, and optimal recycling path. These tags make sorting easier by automatic systems to maintain materials in the appropriate loop. It is a marriage of biology, chemistry, and information science turning "waste" into a quality resource for its next life.

Closed loops don't just happen in the design lab, but they need real-world systems to support them. This means:

- **Collection networks** that efficiently retrieve used plastics.
- **Recycling facilities** that can handle bio-based materials without contamination.
- **Reverse logistics** platforms that bring materials back from the consumer to the producer.

Economic and Environmental Value of Closed Loops

It is the effectiveness of closed loops that makes them so powerful. Each kilogram of recycled plastic saves energy, raw materials, and emissions. The environmental benefits are obvious, but the economic ones are just as compelling. [20]

- **Reduced costs of production:** Companies can cut costs on virgin materials by recycling what they already possess
- **Resilient supply chains:** Closed loops reduce reliance on volatile raw material markets.
- **Compliance with regulation:** Many governments now offer incentives, or impose penalties based on circularity scores

Summary

This study puts the revolutionary potential of integrating Cradle-to-Cradle values with Life Cycle Assessment of bio-based plastics on the front burner. Unlike

conventional LCA schemes whose target is waste dumping, C2C systematic thinking considers incessant material flow, aligning with the vision of a circular economy. By producing bio-plastics that are intended to be recyclable, compostable, and traceable, one can close the loop and dramatically reduce both environmental and economic loss. However, realizing this potential is not merely about product technology but also infrastructure, data systems, and systems of regulation that support closed-loop logistics. As bioplastics develop as essential materials for sustainable development, system-level LCA models will be essential tools to make sure that they contribute positively and holistically towards environmental, economic, and social objectives.

Conclusion

This paper introduces a forward-looking strategy that links Cradle-to-Cradle (C2C) principles to Life Cycle Assessment (LCA) in circular bio-based plastics. Traditional LCA approaches cannot handle the circular material flows and regeneration cycles of circular economies. This work, on the other hand, introduces a systems-based LCA approach where several cycles of reuse, recycling, and reintegration are taken into account, providing a positive lift to sustainability measurements. It covers the classification and possibilities of bioplastics, explains traditional vs. C2C LCAs, and explores the central role that design plays in bringing closed-loop systems into operation. Challenges of data availability, standardization, and system modeling are also mentioned. The methodology points out that bio-based plastics, when incorporated into system C2C loops, have the capacity to shift from being environmentally burdensome to positive regenerative resources. Ultimately, the paper confirms the transition toward "doing more good" rather than "doing less harm" in sustainable material systems.

References

- [1] Atiwesh, G, Mikhael, A, Parrish, CC, Banoub, J & Le, T-AT 2021, "Environmental impact of bioplastic use: A review," *Heliyon*, 7(9):e07918, DOI: 10.1016/j.heliyon.2021.e07918
- [2] Senila, L., Kovacs, E., Resz, M.-A., Senila, M., Becze, A., & Roman, C. (2024). Life Cycle Assessment (LCA) of Bioplastics Production from Lignocellulosic Waste (Study Case: PLA and PHB). *Polymers*, 16(23), 3330. <https://doi.org/10.3390/polym16233330>
- [3] Edo, GI, Mafe, AN, Ali, ABM, Akpoghelie, PO, Yousif, E, Isoje, EF, Igbuku, UA, Zainulabdeen, K, Owheruo, JO, Essaghah, AEA, Umar, H, Ahmed, DS & Alamiery, AA 2025, "Life cycle and environmental impact assessment of biopolymer-based packaging vs. conventional plastics in the food industry,"

Materials Today Communications, 46112806,
<https://doi.org/10.1016/j.mtcomm.2025.112806>

[4] Anastas, PT & Zimmerman, JB 2003, “Peer Reviewed: Design through the 12 Principles of Green Engineering,” *Environmental Science & Technology*, 37(5):94A-101A, <https://doi.org/10.1021/es032373g>

[5] Braungart, M, McDonough, W & Bollinger, A 2006, “Cradle-to-cradle design: creating healthy emissions – a strategy for eco-effective product and system design,” *Journal of Cleaner Production*, 15(13–14):1337–1348, <https://doi.org/10.1016/j.jclepro.2006.08.003>.

[6] McDonough, W & Braungart, M 2002, “Cradle to cradle: remaking the way we make things,” *Choice Reviews Online*, 40(02):40–0914, <https://doi.org/10.5860/choice.40-0914> .

[7] Geissdoerfer, M, Savaget, P, Bocken, NMP & Hultink, EJ 2016, “The Circular Economy – A new sustainability paradigm?,” *Journal of Cleaner Production*, 143757–768, <https://doi.org/10.1016/j.jclepro.2016.12.048>

[8] Kinn, M.C. An Innovative Approach to Closing the Loop in a Circular Plastic Economy by Upcycling Single-Use Post-consumer Thin Film Plastic Packaging Waste into Durable Plastic Products. *Mater Circ Econ* 6, 59 (2024). <https://doi.org/10.1007/s42824-024-00152-7>

[9] Rasheed, T, Vattathurvalappil, SH, Shaikat, MM, Theravalappil, R, Ali, U, Ummer, AC, Saleem, MTB, Jaseer, EA & Imran, M 2024, “Recent updates on biodegradability and recyclability of bioplastics - Towards a new era in sustainability,” *Sustainable Materials and Technologies*, 41e01051, <https://doi.org/10.1016/j.susmat.2024.e01051>

[10] Da Silva, LF, Resnitzkyd, MHC, Del Rosario Santibanez Gonzalez, E, De Melo Conti, D & Da Costa, PR 2022, “Management of plastic waste and a Circular Economy at the end of the Supply Chain: A Systematic literature review,” *Energies*, 15(3):976, <https://doi.org/10.3390/en15030976>

[11] Tamoor, M, Samak, NA, Yang, M & Xing, J 2022, “The Cradle-to-Cradle Life Cycle Assessment of Polyethylene terephthalate: Environmental Perspective,” *Molecules*, 27(5):1599, <https://doi.org/10.3390/molecules27051599>

[12] De Araujo, JB, Dieterle, M, Schell, L, Herrmann, T, Haug, M & Viere, T 2024, “How do LCA studies support CE? A systematic case study review,” *Circular Economy*, 2(3):, <https://doi.org/10.55845/rww19003>

[13] Samani, P 2023, “Synergies and gaps between circularity assessment and Life Cycle Assessment (LCA),” *The Science of the Total Environment*, 903166611, <https://doi.org/10.1016/j.scitotenv.2023.166611>

[14] Kara, S, Hauschild, M, Sutherland, J & McAloone, T 2022, “Closed-loop systems to circular economy: A pathway to environmental sustainability?,” *CIRP Annals*, 71(2):505–528, <https://doi.org/10.1016/j.cirp.2022.05.008>

[15] Zhou, S & Smulders, S 2021, “Closing the loop in a circular economy: Saving resources or suffocating innovations?,” *European Economic Review*, 139103857, <https://doi.org/10.1016/j.euroecorev.2021.103857>.

[16] Arijeniwa, VF, Akinsemolu, AA, Chukwugozie, DC, Onawo, UG, Ocholor, CE, Nwauzoma, UM, Kawino, DA & Onyeaka, H 2024, "Closing the loop: A framework for tackling single-use plastic waste in the food and beverage industry through circular economy- a review," *Journal of Environmental Management*, 359120816, <https://doi.org/10.1016/j.jenvman.2024.120816>

[17] Ribul, M, Lanot, A, Pisapia, CT, Purnell, P, McQueen-Mason, SJ & Baurley, S 2021, "Mechanical, chemical, biological: Moving towards closed-loop bio-based recycling in a circular economy of sustainable textiles," *Journal of Cleaner Production*, 326129325, <https://doi.org/10.1016/j.jclepro.2021.129325>

[18] Muneer, NF, Nadeem, H, Arif, A & Zaheer, W 2021, "Bioplastics from Biopolymers: An Eco-Friendly and Sustainable Solution of Plastic Pollution," *Polymer Science Series C*, 63(1):47–63, <https://doi.org/10.1134/s1811238221010057>

[19] Thakur, S, Chaudhary, J, Sharma, B, Verma, A, Tamulevicius, S & Thakur, VK 2018, "Sustainability of bioplastics: Opportunities and challenges," *Current Opinion in Green and Sustainable Chemistry*, 1368–75, <https://doi.org/10.1016/j.cogsc.2018.04.013>

[20] Wang, B, Cheng, H & Yang, H 2025, "Coordinate the environmental and economic sustainability in a closed-loop supply chain," *Journal of Environmental Management*, 381125227, <https://doi.org/10.1016/j.jenvman.2025.125227>